NAG3-335

IN-07-

11709 P-94

(NASA-CR-177206) CHANNEL FLOW MODELING OF IMPINGEMENT COOLING OF A ROTATING TURBINE BLADE (Massachusetts Inst. of Tech.) 94 p HC A05/MF A01 CSCL 21E

N86-27285

Unclas

G3/07 43250

CHANNEL FLOW MODELING OF IMPINGEMENT COOLING OF A ROTATING TURBINE BLADE

by

JaHye Jenny Koo

GT&PDL Report No. 181 December 1984

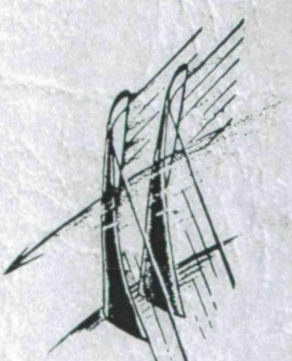

GAS TURBINE & PLASMA DYNAMICS LABORATORY

MASSACHUSETTS INSTITUTE OF TECHNOLOGY

CAMBRIDGE, MASSACHUSETTS

CHANNEL FLOW MODELING OF IMPINGEMENT COOLING OF A ROTATING TURBINE BLADE

by

JaHye Jenny Koo

GT&PDL Report No. 181 December 1984

This research was supported by the NASA Lewis Research Center under Grant No. NAG3-335.

ABSTRACT

Local heat transfer distributions in impingement cooling have been measured by Kreatsoulas [1] and Preiser [2] for a range of conditions which model those in actual turbine blades, including the effects of rotation. These data were reported as local Nusselt numbers, but referred to coolant supply conditions. By means of a channel flow modeling of the flow in the supply and impingement passages, the same data are here presented in terms of local Nusselt number distributions such as are used in design. The results in this form are compared to the nonrotating impingement results of Chupp [3] and to the rotating but non-impingement results of Morris [4]. Rotation reduces the mean Nusselt numbers from these found by Chupp by about 30 percent, and introduces important radial variations which are sensitive to rotation and to leading edge stagger angle.

HEAT TRANSFER COEFFICIENTS
CHANNEL FLOW
TURBINE BLADES
JET IMPINGEMENT
COOLING
ROTATION

NUSSELT NUMBER
COOLANTS
LEADING EDGES
AIRFOILS
CONVECTIVE HEAT TRANSFER
COEFFICIENT OF FRICTION
CORIOLIS EFFECT
BUOYANCY
PRESSURE GRADIENT

ACKNOWLEDGEMENTS

I would like to express my deepest appreciation to my advisor, teacher and friend, Professor Jack L. Kerrebrock. It was his enthusiasm, optimism and endless encouragement, as much as his extensive knowledge and hard work into this project throughout the year, which led to the completion of this work.

Special thanks to Professor Alan H. Epstein, Dr. Robert Norton, and Dr. Hyoun-Woo Shin for their comments and suggestions in the initial stage of the program.

My sincere thanks to Messrs. Bob Haimes, Mike Giles, and Mark Drela for their patience in answering my numerous questions. Their personal warmth and invaluable assistance throughout the program helped me survive my first year at MIT.

TABLE OF CONTENTS

NOMENCLATURE

English Symbols

A	cross-sectional area	(sq. m)
Cp	specific heat under constant	(J/Kg K)
d	impingement jet diameter	(m)
D	leading edge diameter	(m)
d_e	equivalent diameter (A/s)	(m)
f	friction factor	
h	heat transfer coefficient	W/sq.m K)
k	thermal conductivity	(W/m K)
$\overline{M}$	Mach number	
Nu	Nusselt number	
p	pressure	(N/sq.m)
P	jet hole pitch	(m)
r	position vector	
r	radius	(m)
Re	Reynolds number	
s	perimeter	(m)
S	surface area	(sq.m)
S	jet span	(m)
St	Stanton number	
T_s	average surface temperature	(K)
T_f	average fluid temperature	(K)
T_t	total fluid temperature	(K)

T_w	effective wall temperature	(K)
u	velocity vector	
u	velocity component in r direction	(m/sec)
Vj	impingement jet velocity	(m/sec)
z	wall to jet distance	(m)

Greek Symbols

γ	Cp/Cv = specific heat ratio	
γ	stagger angle	(rad)
μ	viscosity	(Nsec/sq.m)
ρ	density	(kg/cu.m)
Ω	angular velocity	(rad/sec)

Subscripts

1	impingement channel
2	supply channel

LIST OF TABLES AND FIGURES

I. INTRODUCTION

One of the most challenging tasks for advancing gas turbine technology is to improve gas turbine efficiency by increased turbine inlet temperature, while maintaining low enough metal temperature levels to achieve acceptable component life. To maintain acceptable temperatures of turbine components, it is necessary to develop effective cooling methods, and the importance of using coolant air in airfoils has been repeatedly emphasized. One of the most effective cooling methods for local internal cooling of turbine blades is jet impingement, which is achieved by blowing cooling air through a series of holes located inside the blades. The effectiveness of this internal cooling technique is measured by the heat transfer coefficient which gives the heat flux per temperature difference between the airfoil and the coolant.

The accurate prediction of the local convection heat transfer coefficient is essential in order to optimize the use of the coolant supply and minimize thermal stresses. Although numerous impingement heat transfer studies have been conducted and reported, most of the available data have been measured in stationary systems, so they do not address the rotational effects in impingement cooling systems. Recently, an extensive set of data on impingement cooling with rotational effects has been obtained by Kreatsoulas [1]. These experiments have revealed large effects due to rotation, on both the mean Nusselt number (averaged on the leading edge surface) and on the detailed heat transfer distribution, which is created by the impinging jets. All of Kreatsoulas' experiments were conducted with a -30 degree stagger angle, typical of the inlet of a high work rotor at the mean radius.

modeled as channel flows, using friction coefficients and heat transfer coefficients which represent averages around the circumference of the passages, and are functions of the radial coordinate along each passage.

Because of the complexity of the flow, it has been possible to describe the effectiveness of impingement cooling only with reference to specific geometries. Thus, Ref. [3] gives correlations in terms of the jet Reynolds number, jet diameter, and the geometric parameters. We describe the effects of rotation relative to this correlation.

Some experiments have been conducted in simple rotating cylindrical passages which show the effects of rotation in such simple geometries and, again, we have compared the data of Kreatsoulas and Preiser with this data, to show the effect of the impingement jets on the heat transfer in the rotating passage. Within the channel flow approximation adopted here, the effects of rotation which are encompassed in the empirical correlations, at least in first approximation, are: 1) the radial pressure gradient in the supply and impingement passages, and its dependence on the heat addition in each passage, which is important in that it controls the flow rates in the impingement orifices, 2) the effect of buoyancy on the heat transfer, and 3) the averaged effect of Coriolis induced cross flow in the passages.

II. EXPERIMENTAL APPARATUS

The experimental apparatus for study of impingement cooling in a rotating system was mainly designed and developed at the MIT Gas Turbine Laboratory and is described in detail by Kreatsoulas [1]. A brief description of the apparatus will be discussed in this section in order to present the modeling of the flow in the impingement region.

The apparatus consists of the rotor, the supporting structure, heat exchangers, instrumentation, calibrating body and blade model, as illustrated in Figure [1]. The blade model, which simulates the leading edge geometry of a real turbine blade, rotates in a vacuum chamber. The vacuum chamber is used to reduce heat transfer by convection from the outer wall to the environment, as well as to eliminate any absorbing medium between radiometer and measurement spot. The infrared radiometer measures the external surface temperature of the foil with a spatial resolution of about 1mm. The local heat transfer coefficients throughout the leading edge region of the blade are then determined from the measured electrical input power and the skin temperature distribution.

Figure [2] shows a geometric description of the flow system of the test model. A thin stainless steel foil (Kanthal A-1), a high resistivity and low thermal coefficient of resistivity material, is electrically heated by dissipation in the skin while being cooled from one side by impinging jets of refrigerant gas (Freon 12). The coolant enters into the supply plenum, flows through the jet holes to the impingement section, and exhausts radially to the exhaust channel. Inside the cooling passage of the model, type E thermocouples and pressure probes are placed to measure

III. FORMULATION OF THE MODEL

Figure [3] illustrates a tube rotating about an axis with a constant angular velocity. Fluid flows in the tube and the motion of this fluid is referred to as a reference coordinate system (r,θ,z). The acceleration vector of a fluid particle, which has a position vector $\vec{r}$ and a velocity vector $\vec{u}$, relative to the rotating coordinate system is

$$\vec{a} = \frac{D\vec{u}}{Dt} + 2\vec{\Omega}x\vec{u} + \vec{\Omega}x(\vec{\Omega}x\vec{r}) \tag{1}$$

$D\vec{u}/Dt$, $2\vec{\Omega}x\vec{u}$, and $\vec{\Omega}x(\vec{\Omega}x\vec{r})$ refer respectively to the total derivative of the velocity vector, Coriolis acceleration, and the centrifugal acceleration.

The Navier-Stokes equation may then be approximated as

$$\rho \quad \frac{D\vec{u}}{Dt} + 2\vec{\Omega}x\vec{u} + \vec{\Omega}x(\vec{\Omega}x\vec{r}) \quad = -\nabla p + \mu\nabla^2\vec{u} \tag{2}$$

where ρ, μ, and p are the density, viscosity, and pressure of the fluid respectively. For a steady flow in the radial direction, Eq. (2) may be simplified as

$$\rho u \frac{\partial u}{\partial r} - \rho\Omega^2 r = -\frac{\partial p}{\partial r} + \mu\nabla^2 u \tag{3}$$

Equation (3), however, does not include the effects of the incoming jets from the supply channel, which we shall assume enter the impingement passage with zero radial momentum. If an elementary radial volume, as shown in Fig. 4, is considered, the momentum balance becomes

$$-\frac{dp}{dr} = \rho u \frac{du}{dr} + u \frac{d}{dr} (\rho u) \tag{4}$$

From continuity,

$$\frac{d}{dr} (\rho uA) = \rho V_j \frac{dA_j}{dr} \tag{5}$$

The energy equation can be derived in a similar manner as the equation of motion by taking a radial element. The heat transfer rate across the surface dS is written in terms of the heat transfer coefficient and the temperature difference as

$$dq = h(T_w - T)dS \tag{14}$$

As a first approximation, the heat transfer rate is estimated by taking the temperature difference between the average temperature of the fluid T and the effective wall temperature T_w, which is assumed to be constant along the passage. T_w is defined as

$$T_w = \frac{A_1 T_s + A_2 T_f}{A_1 + A_2} \tag{15}$$

where

A_1 = impingement channel cross-sectional area

A_2 = supply channel cross-sectional area

T_s = average surface temperature

T_f = average fluid temperature

In the final heat transfer coefficient calculation, T_w is replaced with the measured local wall temperature, and T is replaced with the local fluid temperature. This is to be described in detail in IV.

The average heat transfer coefficient, as a first approximation, is estimated by applying the following analogies. The Reynolds analogy, which assumes complete similarity of momentum and heat transfer, provides the following equation.

$$St = \frac{Nu}{Pr\ Re} = \frac{h}{\rho c_p u} \tag{16}$$

where the total temperatures

$$T_{t_1} = T_1 + \frac{u_1^2}{2c_p}$$

and (22)

$$T_{t_2} = T_2 + \frac{u_2^2}{2c_p}$$

The final six differential equations describing the flow characteristics derived for the regions of interest are presented in non-dimensional form as follows.

Impingement region,

$$\frac{1-M_1^2}{1+\frac{\gamma-1}{2}M_1^2}\frac{r}{u_1}\frac{du_1}{dr} = \frac{\pi d_1 r}{A_1}\left(\frac{T_w}{T_{t_1}} - 1\right)St + \left(\frac{\rho_2 V_j}{\rho_1 u_1}\right)\left[\frac{1+\gamma M_1^2}{1+\frac{\gamma-1}{2}M_1^2} + \frac{T_{t_2}}{T_{t_1}} - 1\right]\frac{r}{A_1}\frac{dA_j}{dr}$$

$$- \frac{M_{T_1}^2}{1+\frac{\gamma-1}{2}M_1^2} + \frac{\gamma M_1^2/2}{1+\frac{\gamma-1}{2}M_1^2} f\frac{s_1}{A_1}r$$

$$- \frac{1+\gamma M_1^2}{1+\frac{\gamma-1}{2}M_1^2}\frac{r}{A_1}\frac{dA_1}{dr} + \frac{k}{\rho_1 u_1 c_p}\frac{r}{T_{t_1}}\frac{d^2T_{t_1}}{dr^2} \qquad (23)$$

$$\frac{r}{T_{t_1}}\frac{dT_{t_1}}{dr} = \frac{\pi d_1 r}{A_1}\left(\frac{T_w}{T_{t_1}} - 1\right)St + \left(\frac{\rho_2 V_j}{\rho_1 u_1}\right)\left[\frac{T_{t_2}}{T_{t_1}} - 1\right]\frac{r}{A_1}\frac{dA_j}{dr}$$

$$+ \frac{(\gamma-1)M_{T_1}^2}{1+\frac{\gamma-1}{2}M_1^2} + \frac{k}{\rho_1 u_1 c_p}\frac{r}{T_{t_1}}\frac{d^2T_{t_1}}{dr^2} \qquad (24)$$

$$M_{T_2}^2 = \frac{\Omega^2 r^2}{\gamma R T_2} = \frac{\Omega^2 r^2}{\gamma R T_{t_2}} \left(1 + \frac{\gamma - 1}{2} \bar{M}_2^2\right) \tag{29d}$$

where $\bar{M}$ = Mach number.

The measured total temperatures and the static pressures at the passage hub of both the impingement and supply channels are prescribed as initial conditions for integration of these equations. The velocities at the passage hub of the regions are prescribed as $u_1 = 0$ and $u_2 = \dot{m}/\rho_2 A_2$ where $\dot{m}$ is the total mass flow rate entering the supply region.

IV. DATA ANALYSIS

The solutions of the differential equations derived in III enable one to obtain the local flow distribution, which further gives the circumferentially averaged flux to the coolant along the radius. In this section, a method of determining the local flow distribution and heat transfer distribution is outlined.

From the measured heat fluxes Kreatsoulas and Preiser calculated, the local heat transfer coefficient h of the leading edge surface using the definition

$$h_c = q/(T - T_c) \tag{30}$$

where T_c is the measured inlet coolant temperature, and q and T are the measured local heat flux and skin temperature, respectively. The value of h_c, calculated using Eq. (30), is based on coolant inlet temperature to the blade, so it includes a number of complex effects, such as heating of the fluid in the supply passage and variations in jet Reynolds number due to differential pressure drops in the supply and impingement passages. A more useful correlation of the local heat transfer distribution may be obtained by basing h on the local fluid temperature T_f in the jets, and by correlating in terms of the local jet Reynolds number. Thus,

$$h_f = q/(T - T_f) \tag{31}$$

For the channel flow analysis, the heat transfer coefficient is averaged around the circumference of the passage along the radius, and Eq. (30) becomes, Chupp, et al. (Eq. 34) which is expressed as a function of geometric parameters and the jet Reynolds number.

$$Nu_{avg} = 0.63\ Re_d^{0.7}\left(\frac{d}{p}\right)^{0.5}\left(\frac{d}{D}\right)^{0.6}\exp\left[-1.27\left(\frac{S}{d}\right)\left(\frac{d}{p}\right)^{0.5}\left(\frac{d}{D}\right)^{1.2}\right] \qquad (34)$$

Nu is an arithmetic average of the Nusselt number for strips located in the leading edge region. Re_d is the jet Reynolds number which is defined as $Re = V_j\rho_2 d/\mu$ where d is the hole diameter. The friction factor is also recalculated as a function of local Reynolds number.

$$f = \frac{0.0791}{Re_d^{0.25}} \qquad (35)$$

An approximate flow distribution is determined from the calculated average Nusselt number and friction factor based on Eqs. (34) and (35), respectively, with the prescribed initial conditions.

The calculated and measured values of the pressure ratio between impingement and supply regions at the inlet are compared. Then an iteration method is applied to satisfy the continuity and zero mass flow at the tip of the supply region.

In the next and final iteration, the Stanton number defined in Eq. (16) is calculated from the average heat transfer, calculated by using Eq. (32). Subsequently, the new local heat transfer averaged in the theta direction, which is based on the temperature difference between the local skin temperature and fluid temperature, is calculated as defined in Eq. (33).

This analysis is applied to all the test data obtained by Kreatsoulas and Preiser. The new calculated heat transfer distribution is then compared with the correlations obtained by other investigators to ensure that the

V. RESULTS AND DISCUSSION

The independent parameters of primary interest in the present study are Reynolds number, rotational speed, heat input, and stagger angle. Tables 2 and 3 summarize the series of parametric studies performed by Kreatsoulas and Preiser which are considered in this analysis. Figures 6A to 34C are the graphical representation of the calculated local flow distribution for all the cases. In Figures 6A to 22C, the velocity, pressure, and temperature of the fluid in both the impingement and supply channels are plotted for each test conducted at -30 degree stagger angle. The results of the local flow distribution calculated for 0 degree stagger angle are similarly illustrated in Figs. 23A to 34C. On the temperature vs radius graphs, the temperatures measured by themocouples at the passage hub and tip are also plotted.

In the impingement passage, the initial condition was applied that T_{t_1} should be equal to the value given by the thermocouple at the base of the impingement passage, and in the region below the first jet, conduction in the radial direction was included in the energy equation. This is why the temperature shows an initial drop before rising due to convective heating.

The outer thermocouple gave fluid temperatures quite different from those computed, and quite inconsistent with the measured heat transfer values. We infer that such measurements are unreliable in the complex, thermally stratified flow found in the impingement passage.

Figures 6D to 22D and 23D to 34D present the Nusselt numbers averaged around the circumference of the passage along the radius for the 30 and 0 degree stagger angle tests. Rotation introduces important radial variations is subject to minimal cross flow and buoyancy effects, it is dominated by the tangential velocity effect and deflects toward the hub. The third jet, under the influence of increasing buoyancy and cross flow, is deflected toward the tip and hence creates a large thermal gradient.

The effect of Reynolds number on heat transfer can be examined by comparing Figs. 13D, 15D, and 17D. In all three cases, the tests were conducted at medium rotational speed and high temperature ratio at 30 degree stagger angle. As the average jet Reynolds number varies from 17000 to 74000, the heat transfer rate increases about three times, the average values ranging from 100 to 280. Similar trends are shown for the low and high speed cases but, at the high rotational speed, the thermal gradients between the jet holes along the passage are more pronounced. For the 0 stagger cases, Figs. 26D and 31D show the increase in heat transfer rate by a factor of 2 as the Reynolds number increases from low to medium. In all the cases, the temperature ratio between the average skin temperature and the coolant temperature seems to have almost no effect on Nusselt number as shown in Figs. 21D and 22D.

The stagger angle effect on impingement-cooled rotating blades is examined by comparing the data obtained by Kreatsoulas and Preiser, which are conducted at 30 and 0 stagger angles, respectively, holding all other nominal conditions the same. Figures 22D and 34D show that the heat transfer rate are lower at zero degrees by approximately 30%, and the high thermal gradient effect due to the dominant tangential velocity effect between the second and third jets is not seen at this angle.

Also indicated in Figs. 6D to 34D are the comparable Nusselt number

VI. CONCLUSION

A channel flow model of flow in the impingement cooling passage of a rotating turbine blade leading edge is used to correct measured heat transfer coefficents to local fluid conditions. The flows in the supply and impingement regions are both modeled as steady state channel flows, using friction and heat transfer coefficents. The local flow properties are obtained by solving the momentum, mass and energy equations with the prescribed initial conditions, and using the local heat transfer rates calculated from the data of Kreatsoulas and Preiser. The local Nusselt number, based on calculated local fluid temperature, is re-evaluated by circumferentially averaging the heat transfer rate. When this result is compared with the Nusselt number, based on the inlet coolant temperature, the maximum difference between them is determined to be about 17 percent. By comparing the calculated Nusselt numbers with the correlations obtained by other investigators, it is concluded that the experimental and modeling formulations are satisfactory. The modeling and the analysis illustrated here, therefore, offer a means for more accurate prediction of impingement cooling heat transfer rates.

REFERENCES

1. Kreatsoulas, J.C., "Experimental Study of Impingement Cooling in Rotating Turbine Blades," Ph.D Thesis, MIT Department of Aeronautics and Astronautics, September 1983.

2. Preiser, Uriel Z., "Stagger Angle Effects on Impingement Cooling of a Rotating Turbine Blade," M.S. Thesis, MIT Department of Aeronautics and Astronautics, May 1984.

3. Chupp, R.E., Helms, H.E., McFadden, P.W. and Brown, T.R., "Evaluation of Internal Heat Transfer Coefficients for Impingement Cooled Turbine Airfoils," Journal of Aircraft, Vol. 6, 1969, pp. 203-208.

4. Morris, W.D. and Ayhan, T., "Observations on the Influence of Rotation on Heat Transfer in the Coolant Channels of Gas Turbine Rotor Blades," Proceedings of the Institute of Mechanical Engineers, Vol. 193, 1979, pp. 303-311.

TABLE 1: TEST SECTION GEOMETRY

Span	S	101.6 mm	4.000 in
Hub radius	Rh	406.4 mm	16.000 in
Tip radius	Rt	508.0 mm	20.000 in
Leading edge diameter	D	12.7 mm	0.500 in
Stagger angle (from axial)	γ	0.523 rad	30.0 deg
Impingement hole diameter	d	2.1 mm	0.081 in
Impingement hole pitch	p	6.1 mm	0.240 in
Wall to jet distance	z	4.1 mm	0.162 in
Impingement insert span	Si	76.2 mm	3.000 in

TABLE 2: -30 degree stagger angle tests

TEST #	ROTATIONAL SPEED	RE #	TW/TC
43	low	low	low
42	low	low	high
39	low	medium	low
44	low	medium	high
40	low	high	low
41	low	high	high
57	medium	low	low
56	medium	low	high
55	medium	medium	low
54	medium	medium	high
59	medium	high	low
58	medium	high	high
63	high	low	low
65	high	medium	low
64	high	medium	high
66	high	high	low
67	high	high	high

TABLE 3: 0 degree stagger angle tests

TEST #	ROTATIONAL SPEED	RE #	TW/TC
113	low	low	high
114	low	medium	high
115	low	medium	high
123	medium	low	high
124	medium	low	high
122	medium	medium	low
119	medium	medium	high
120	medium	medium	high
121	medium	medium	high
128	high	medium	low
126	high	medium	high
127	high	high	high

Fig 1: Experimental Apparatus Schematic Drawing

1. Blade Model
2. Vacuum Chamber
3. Imaging System
4. IR Detector
5. Heat Exchanger
6. Encoder
7. Power Slip Rings
8. Gun Bored Shaft
9. Seal
10. R-12 Inlet
11. R-12 Outlet
12. Var. Speed Drive
13. Instr. Slip Rings
14. Calibration Body

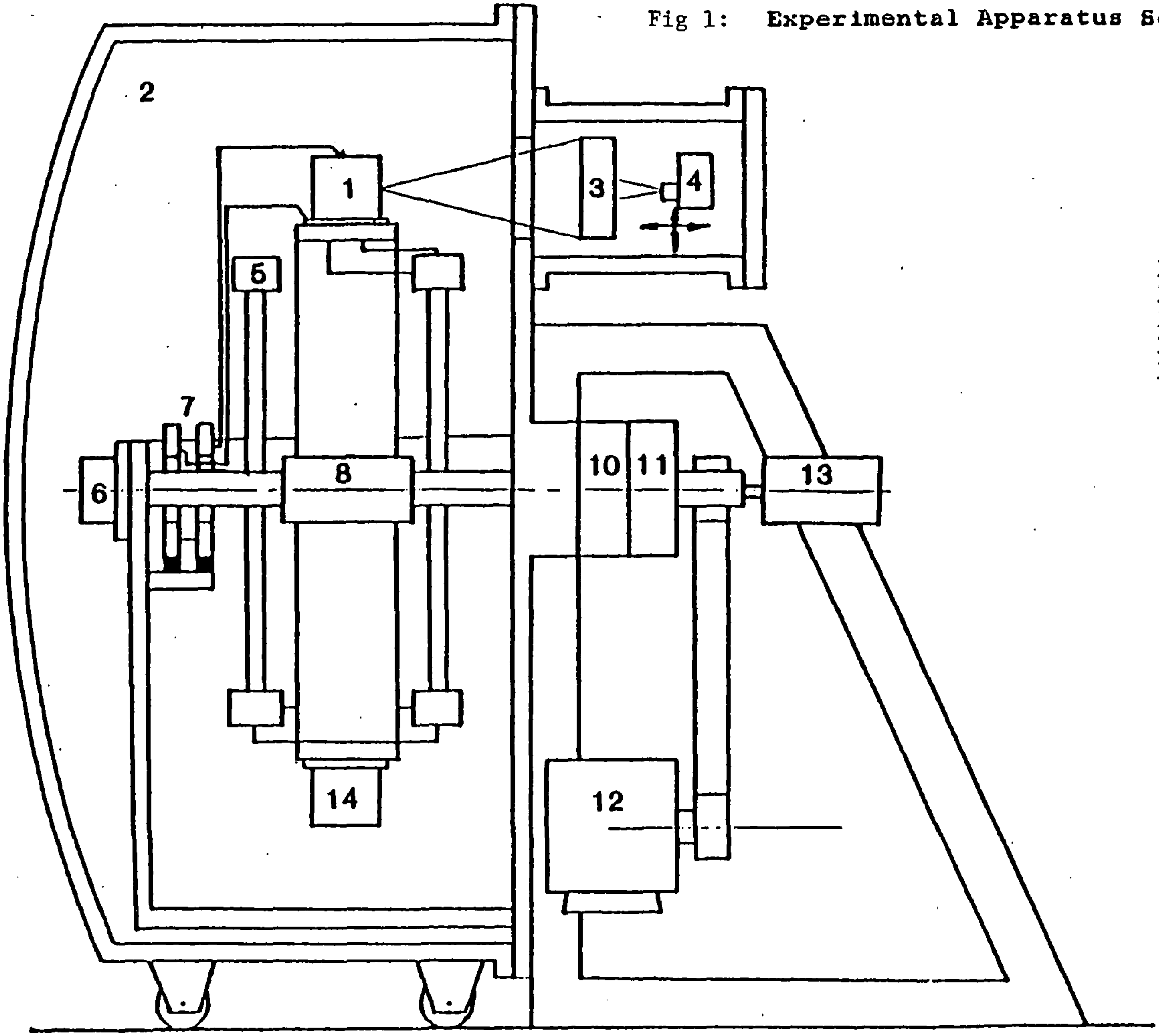

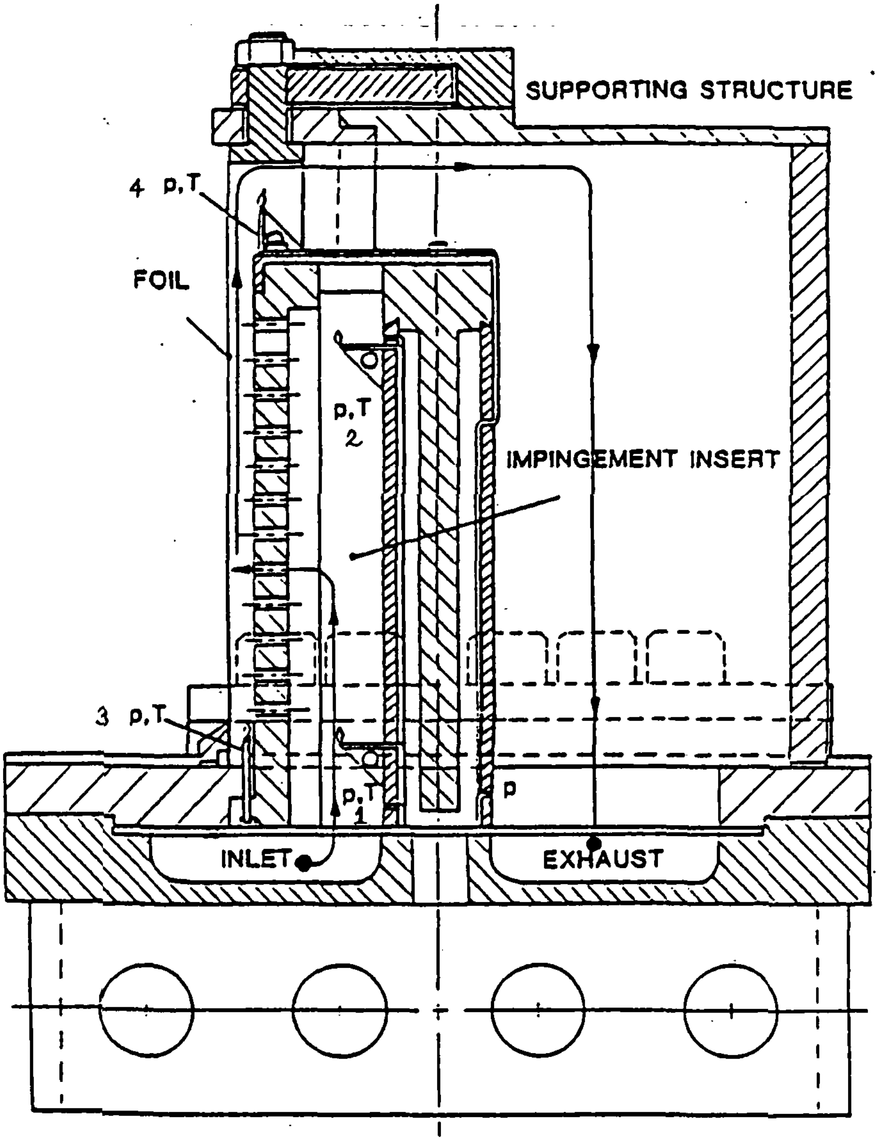

Fig. 2: **Blade Model Cross Section (Side View)**
1. T - Thermocouple
2. P - Pressure Tap

Thermocouple and pressure tap locations*

1. 0.3905 m
2. 0.4747 m
3. 0.4008 m
4. 0.4921 m

* measured from the center of the shaft

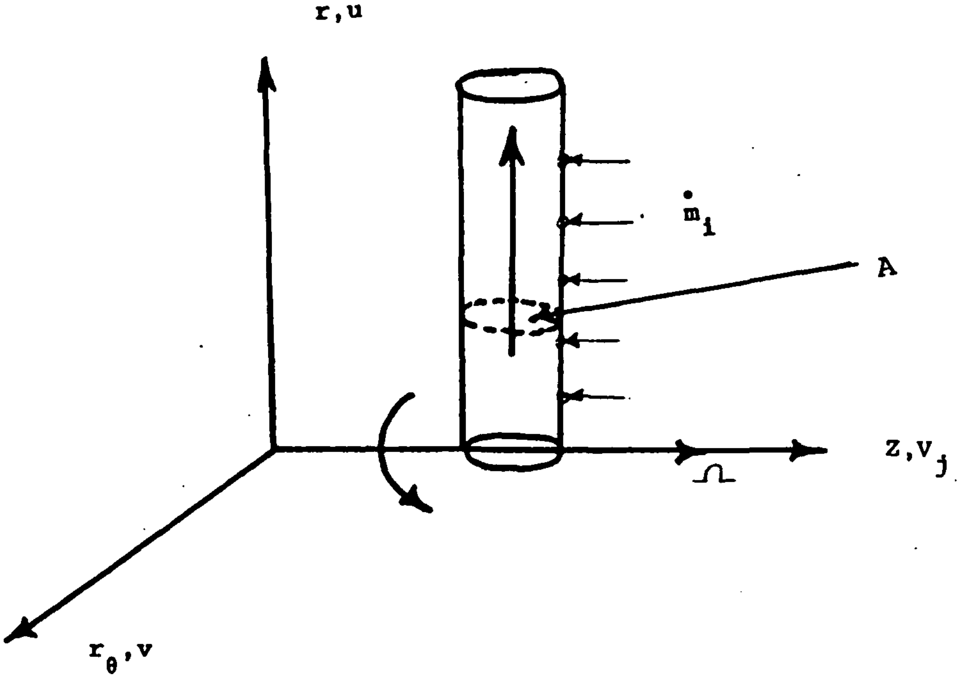

Figure 3: Flow in radial coolant passage

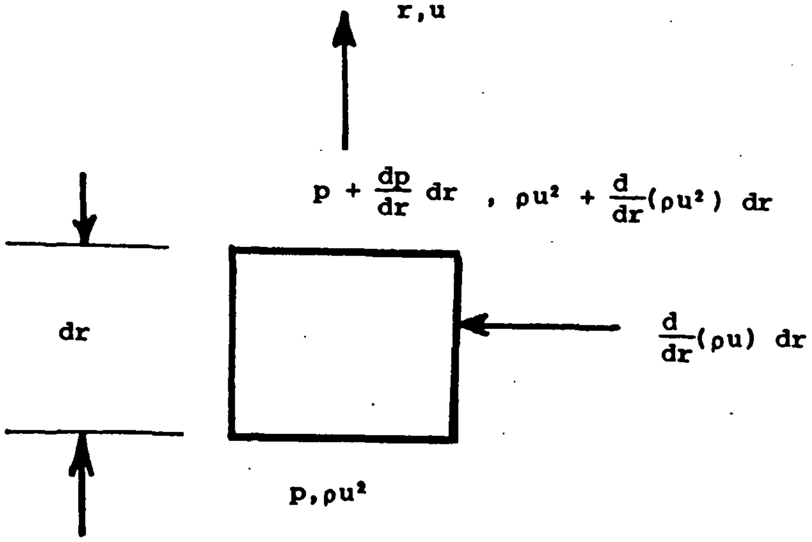

Figure 4: Elementary radial volume

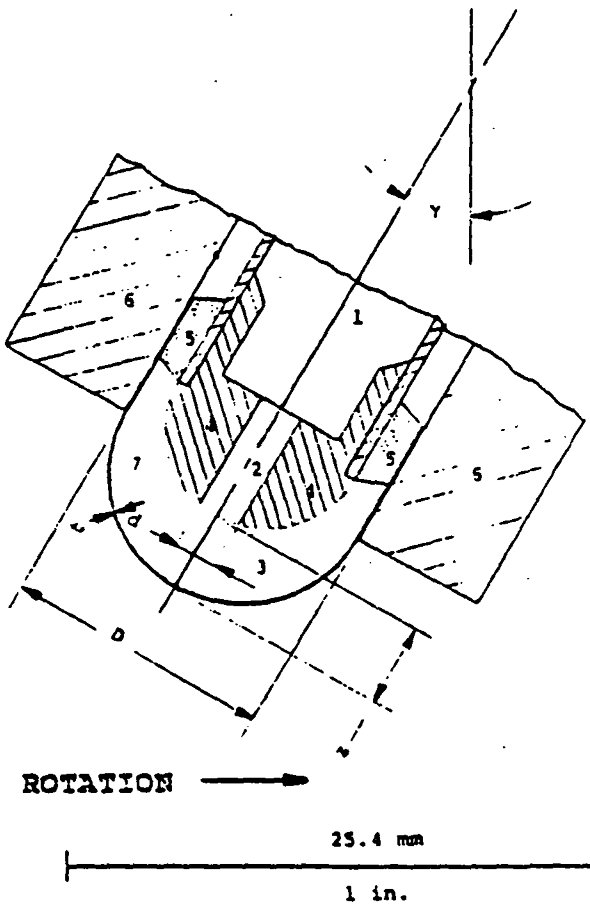

Fig 5: **Test Section Geometry (Top View)**

1. Supply Plenum
2. Jet Hole
3. Impingement Space
4. Impingement Insert
5. Rubber Seal
6. Cover
7. Resistive Wall

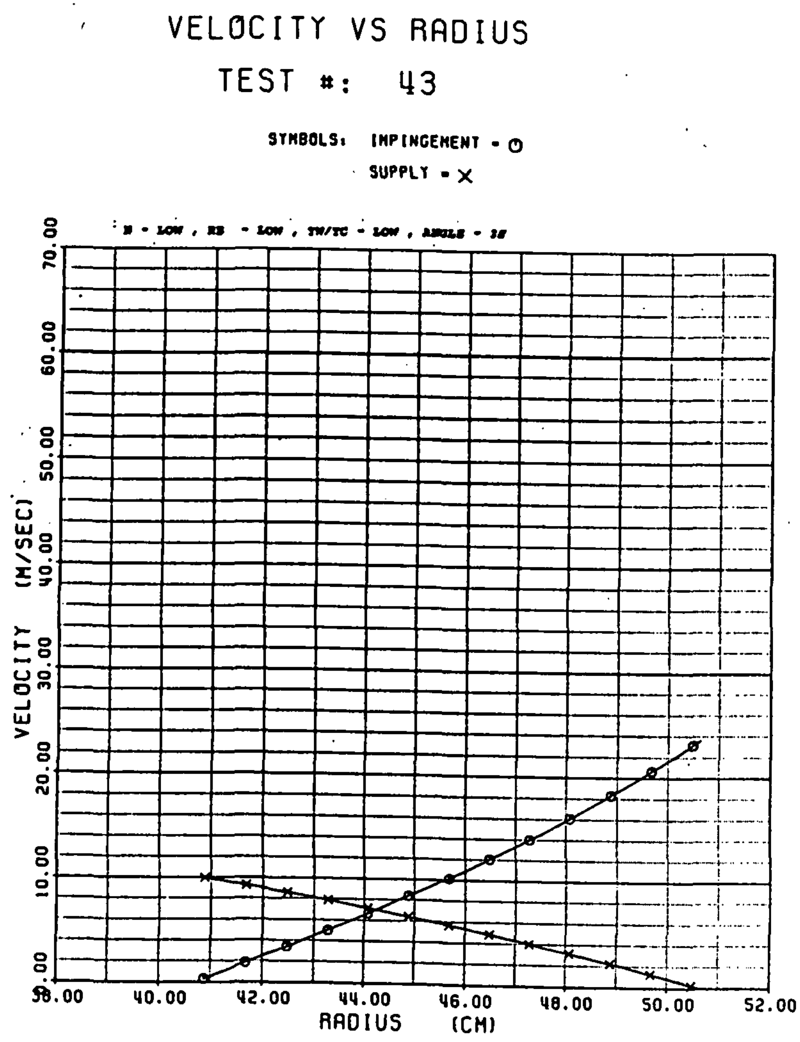

Figure 6A

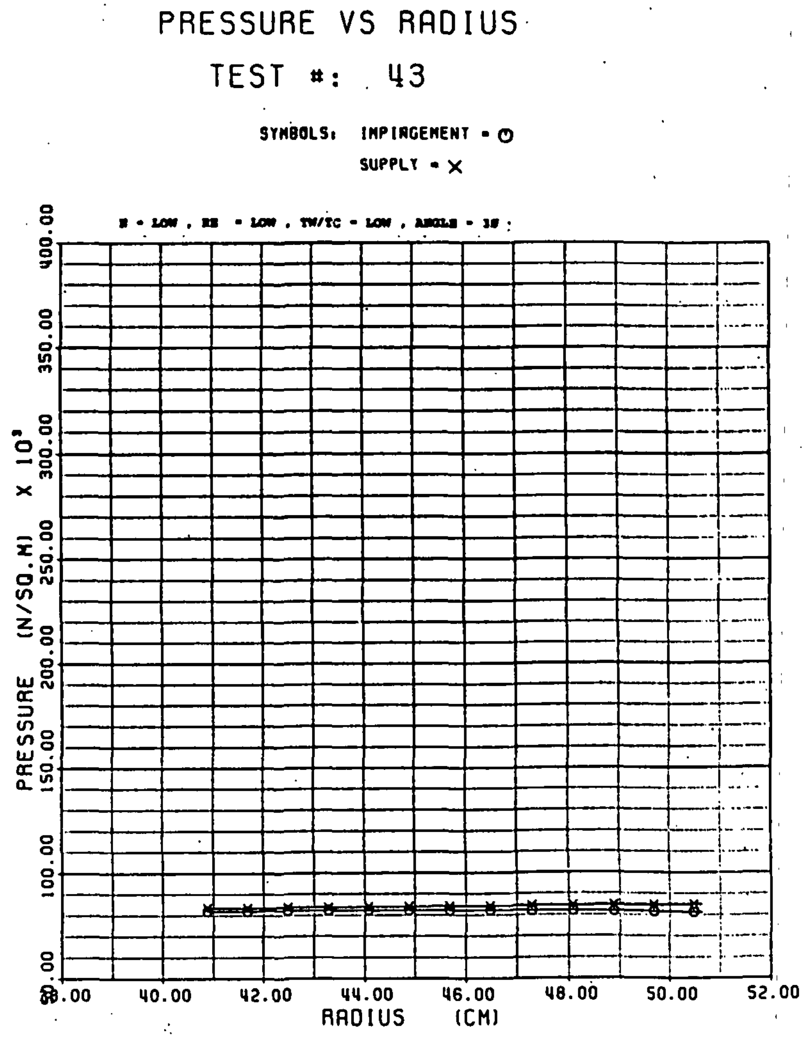

Figure 6B

ORIGINAL PAGE IS OF POOR QUALITY

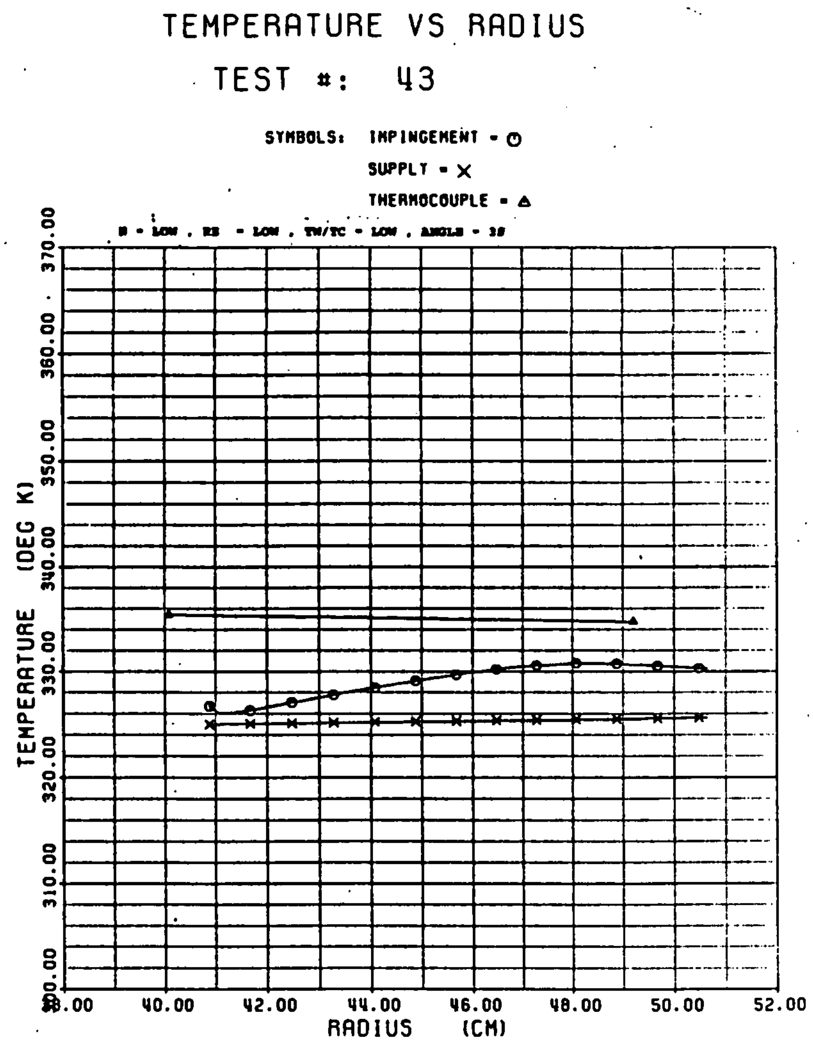

Figure 6C

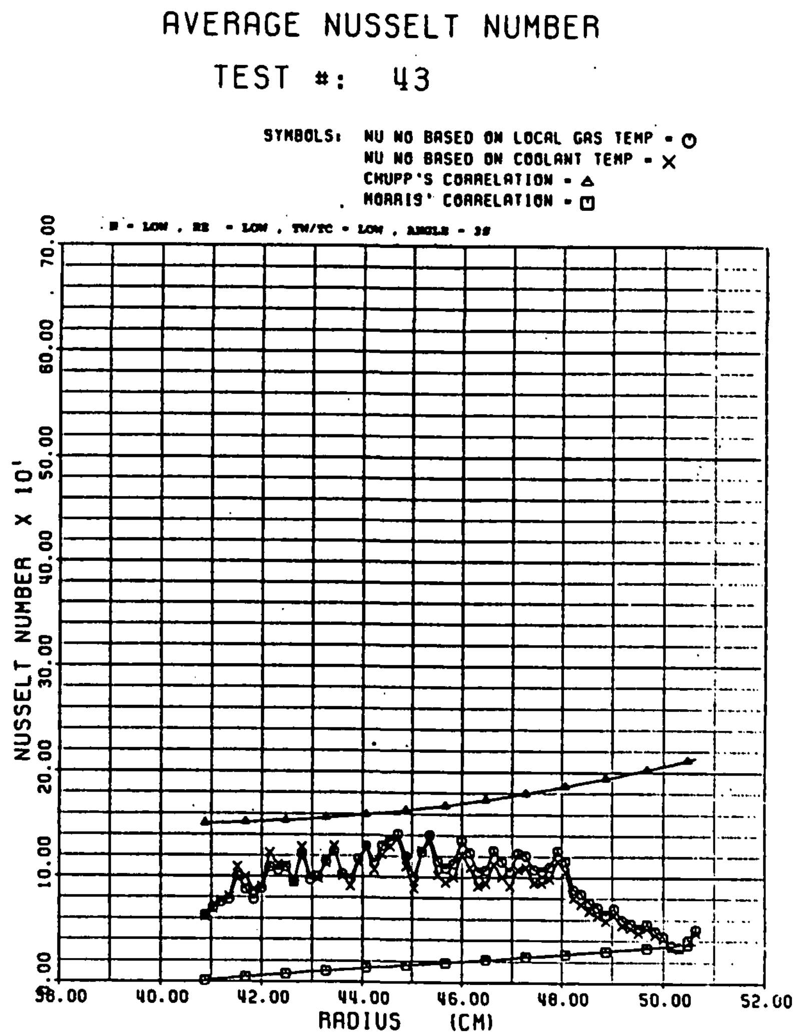

Figure 6D

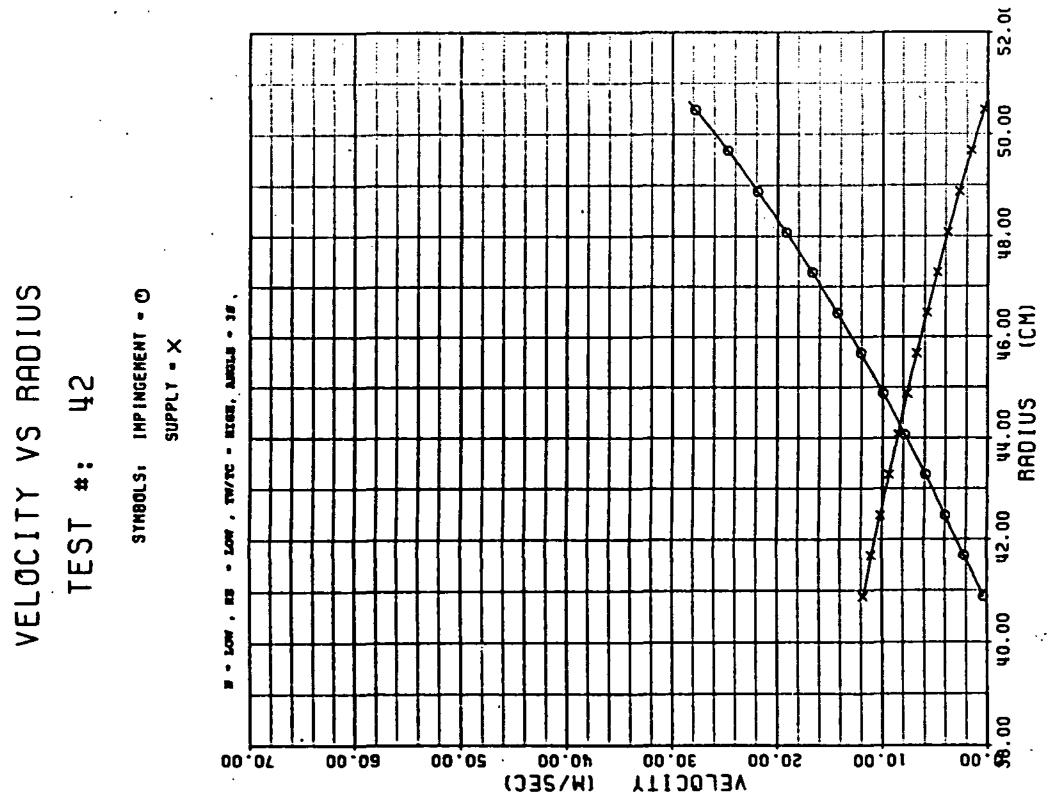

Figure 7A

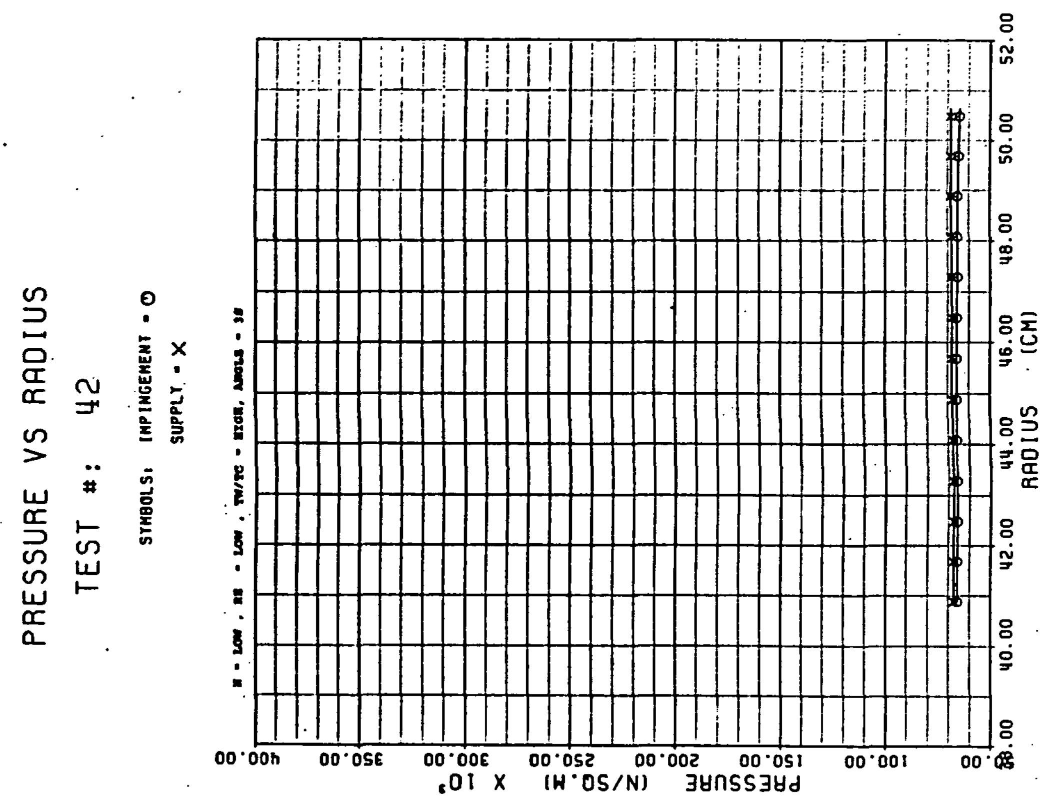

Figure 7B

ORIGINAL PAGE IS
OF POOR QUALITY

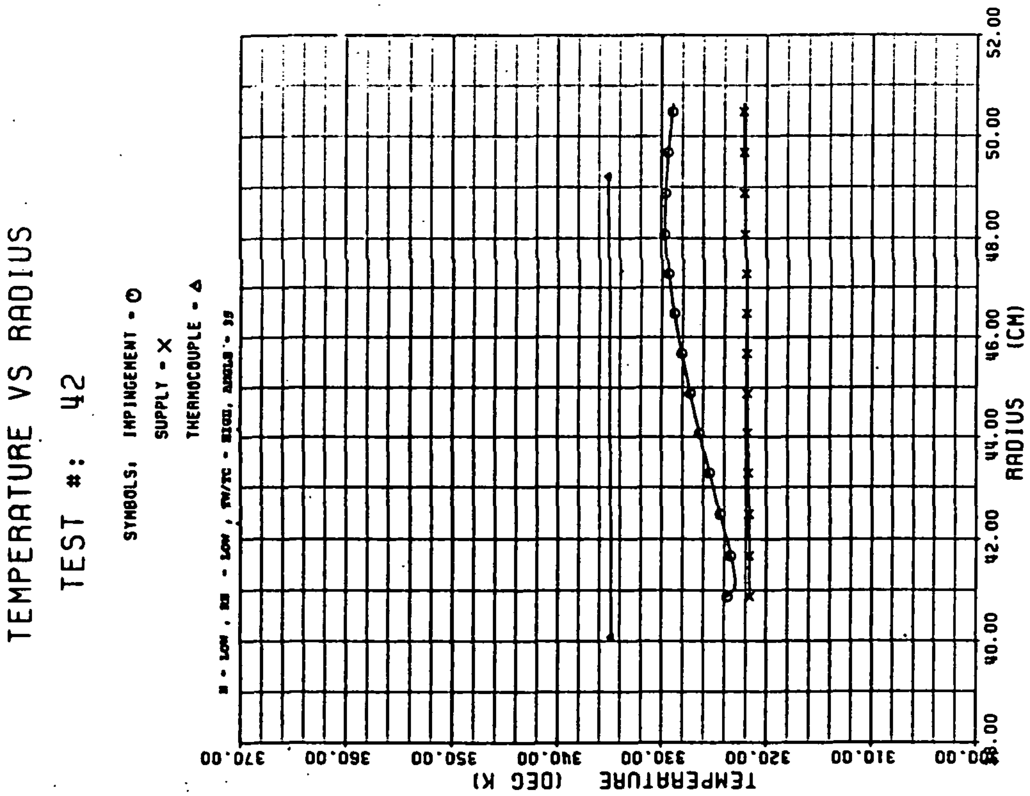

Figure 7C

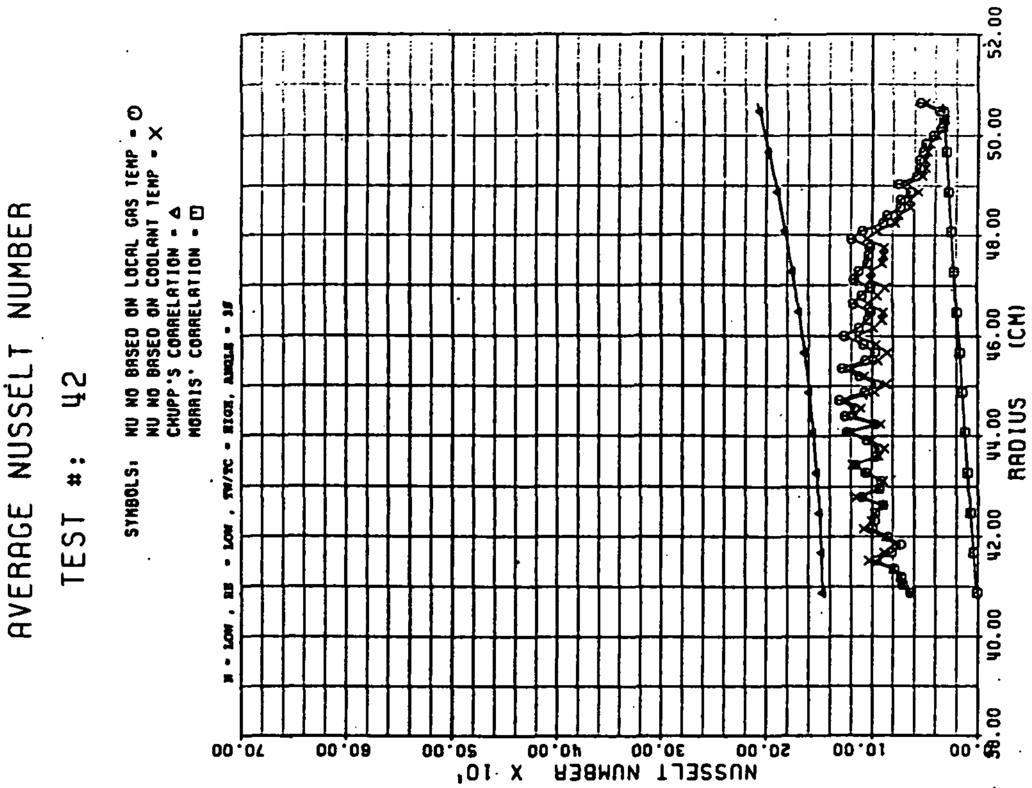

Figure 7D

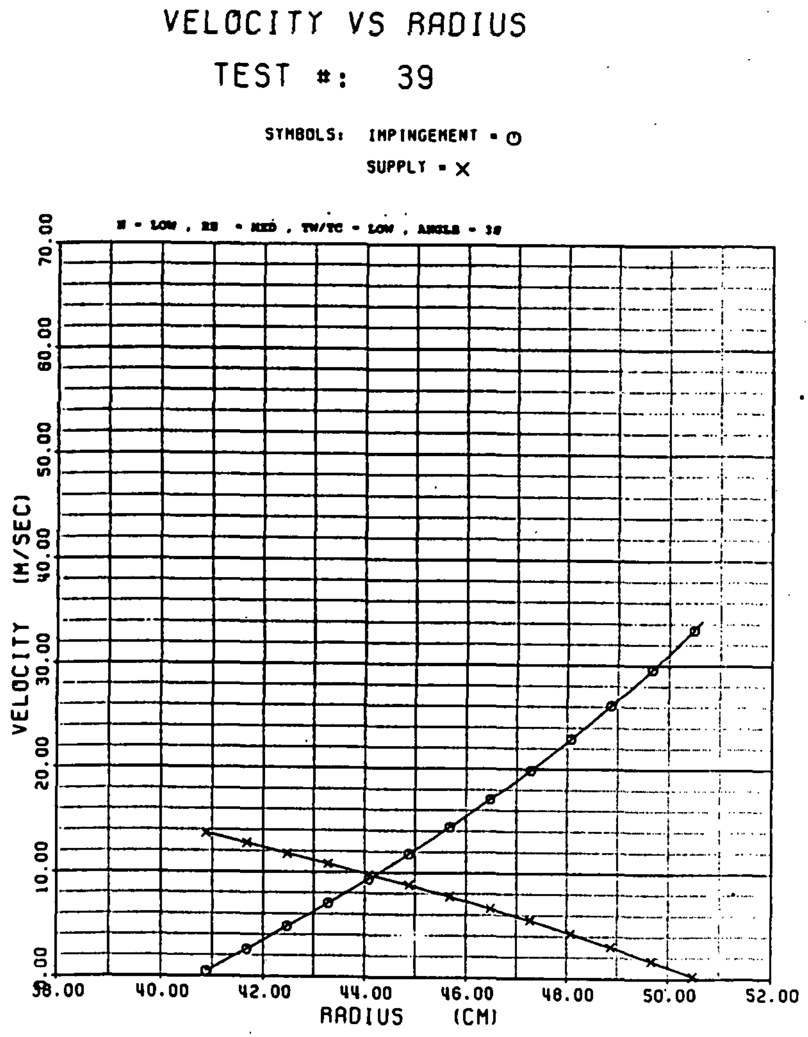

Figure 8A

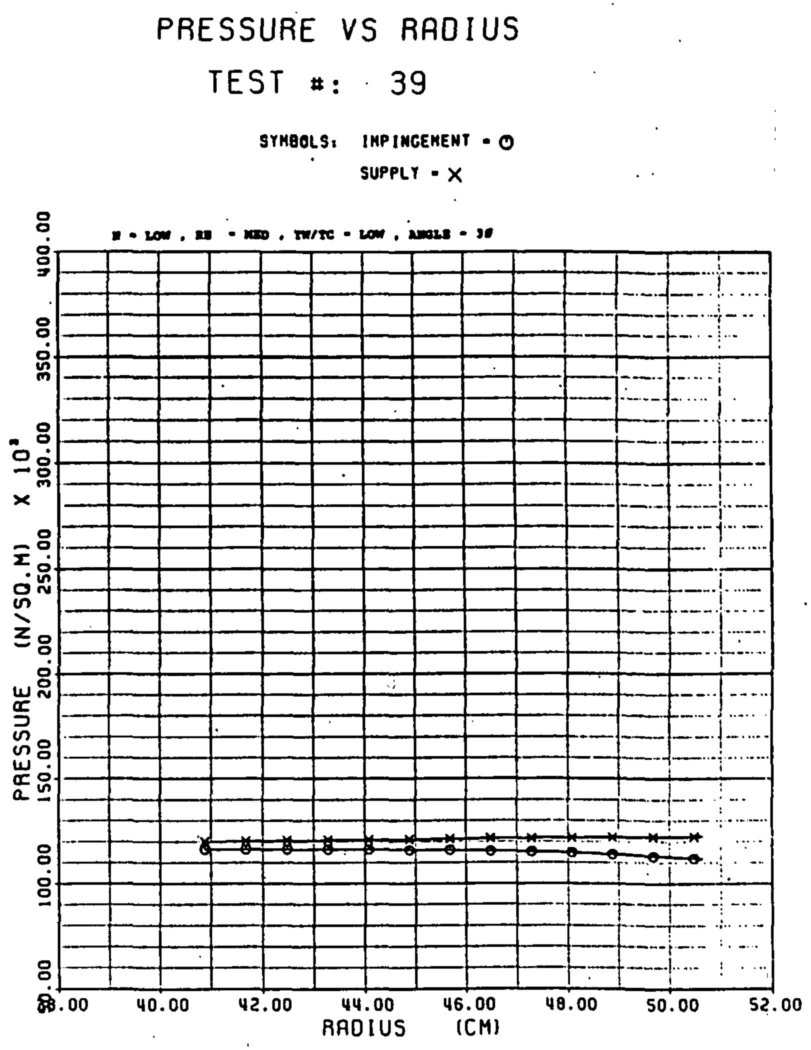

Figure 8B

ORIGINAL PAGE IS
OF POOR QUALITY

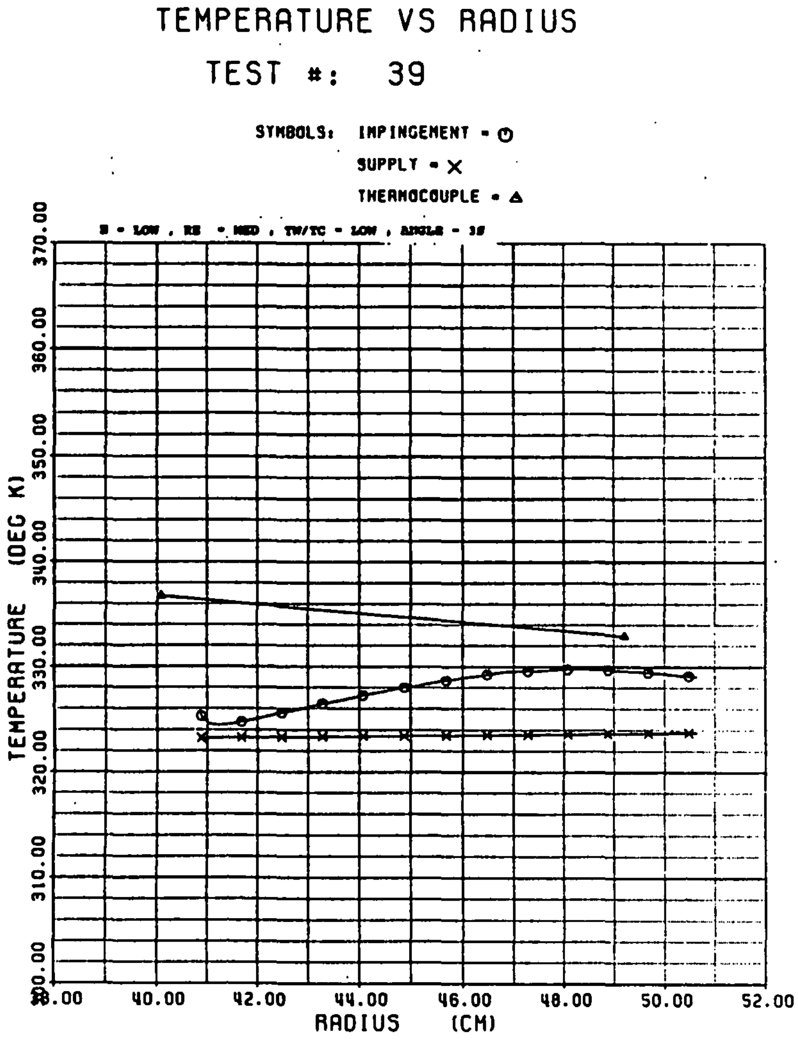

Figure 8C

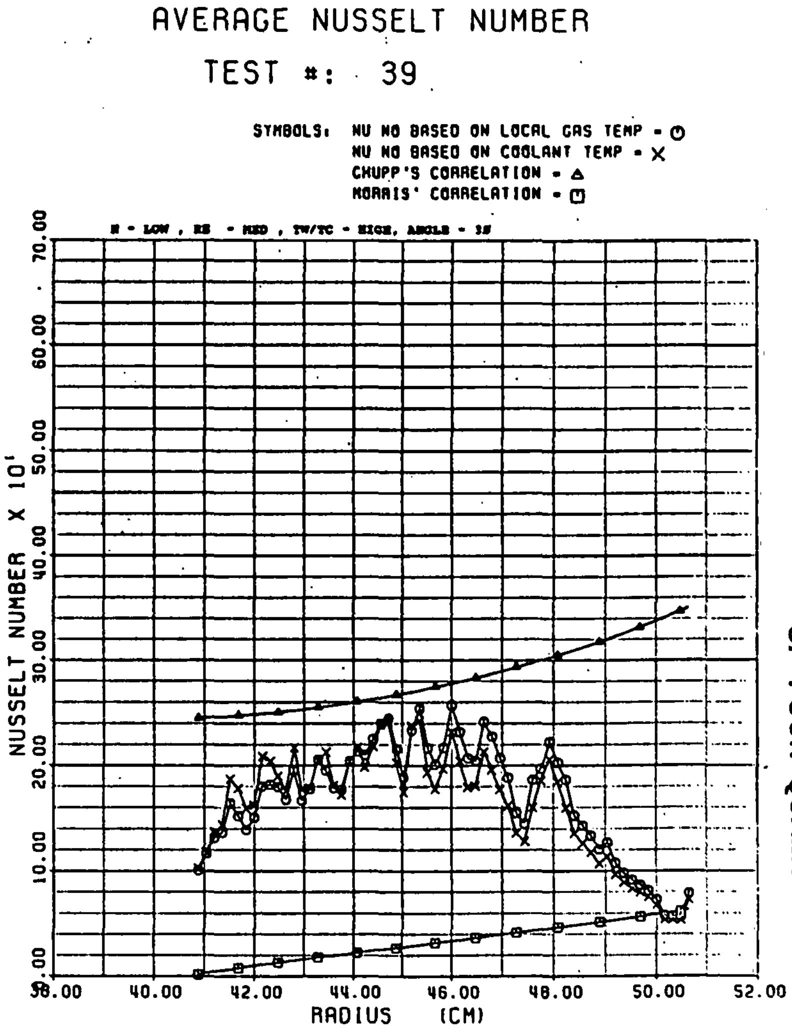

Figure 8D

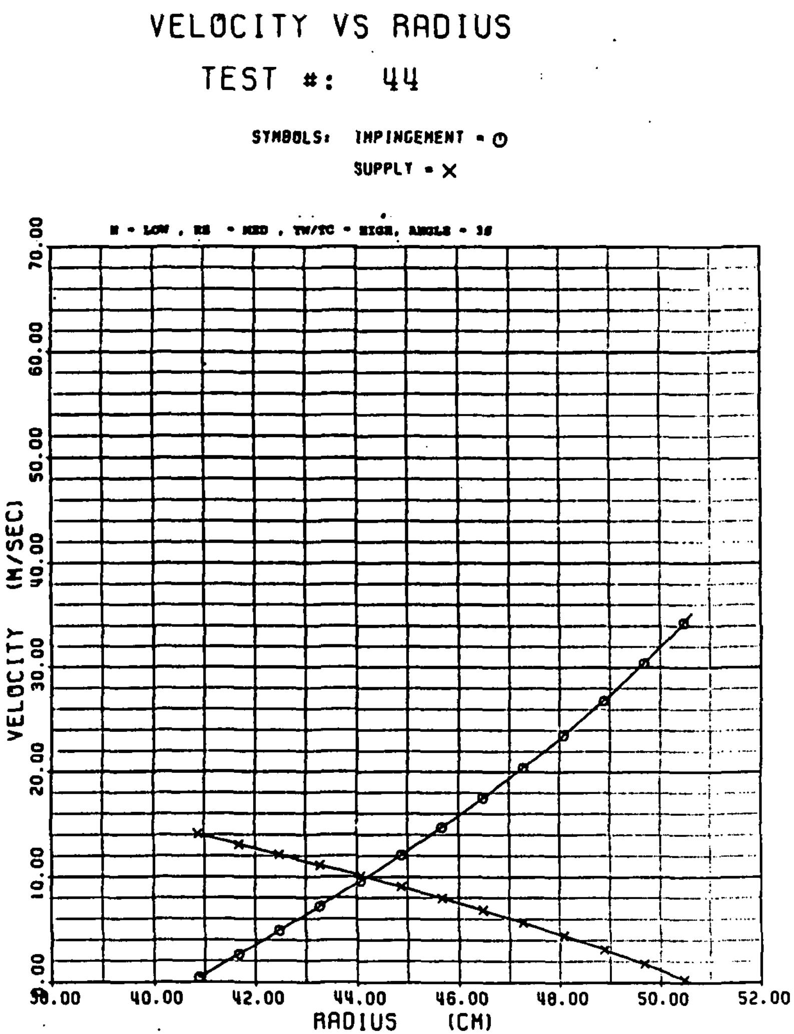

Figure 9A

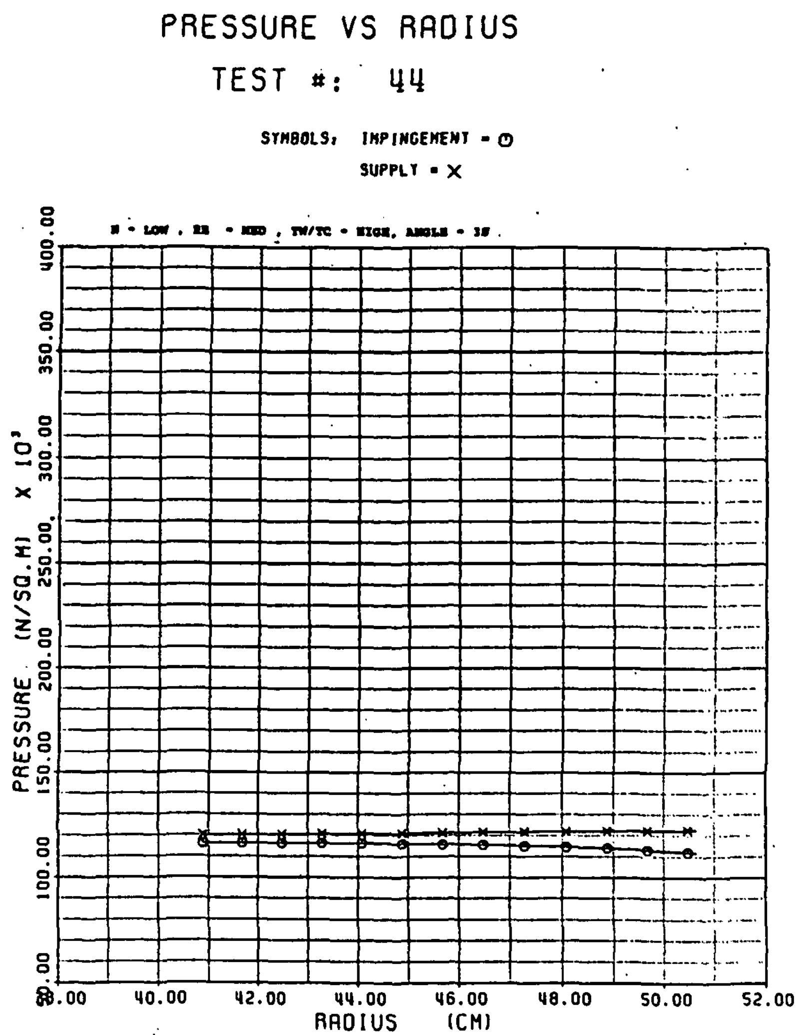

Figure 9B

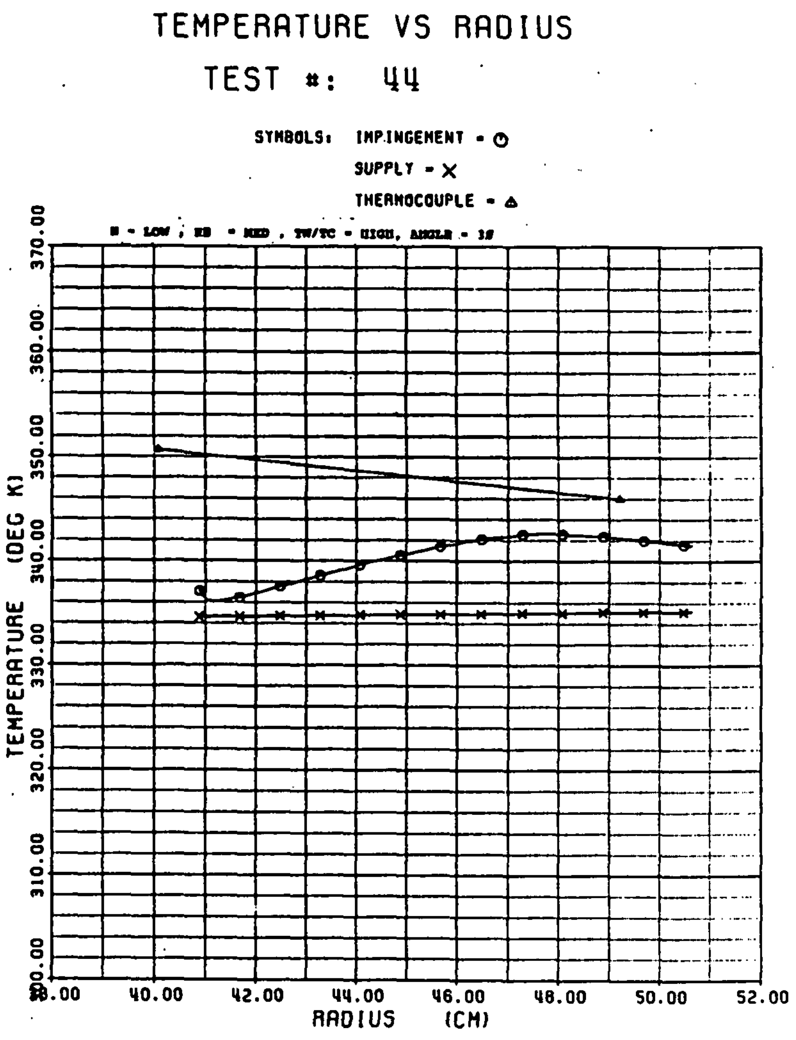

Figure 9C

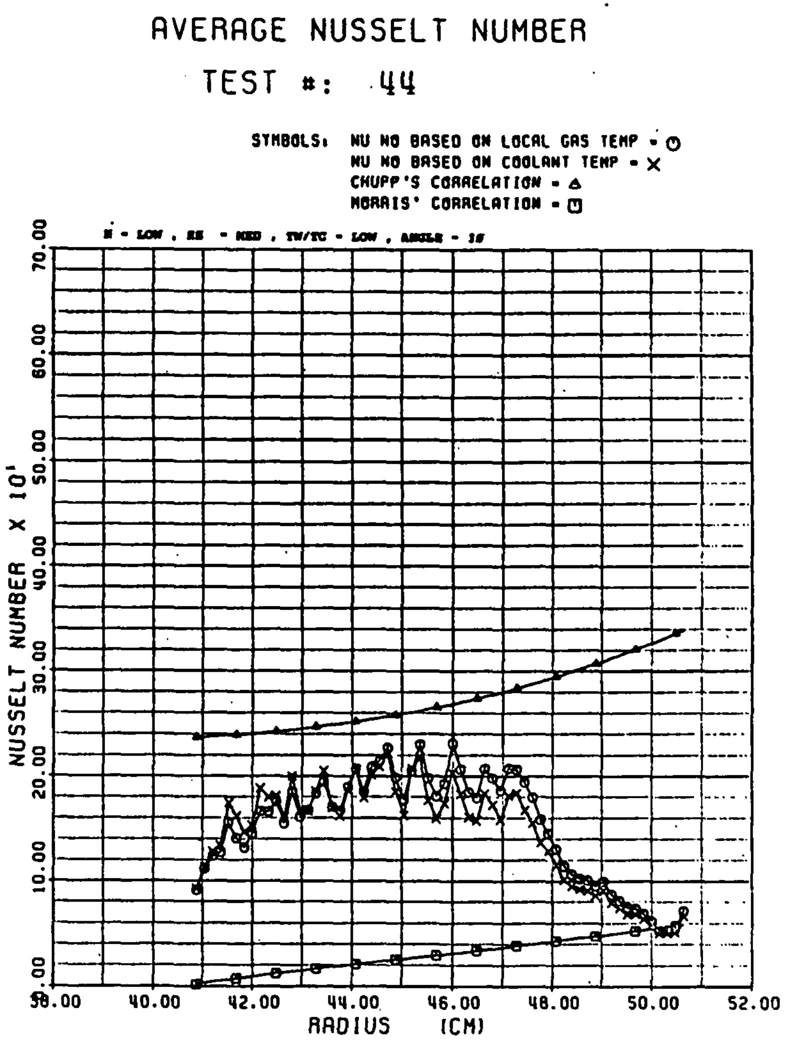

Figure 9D

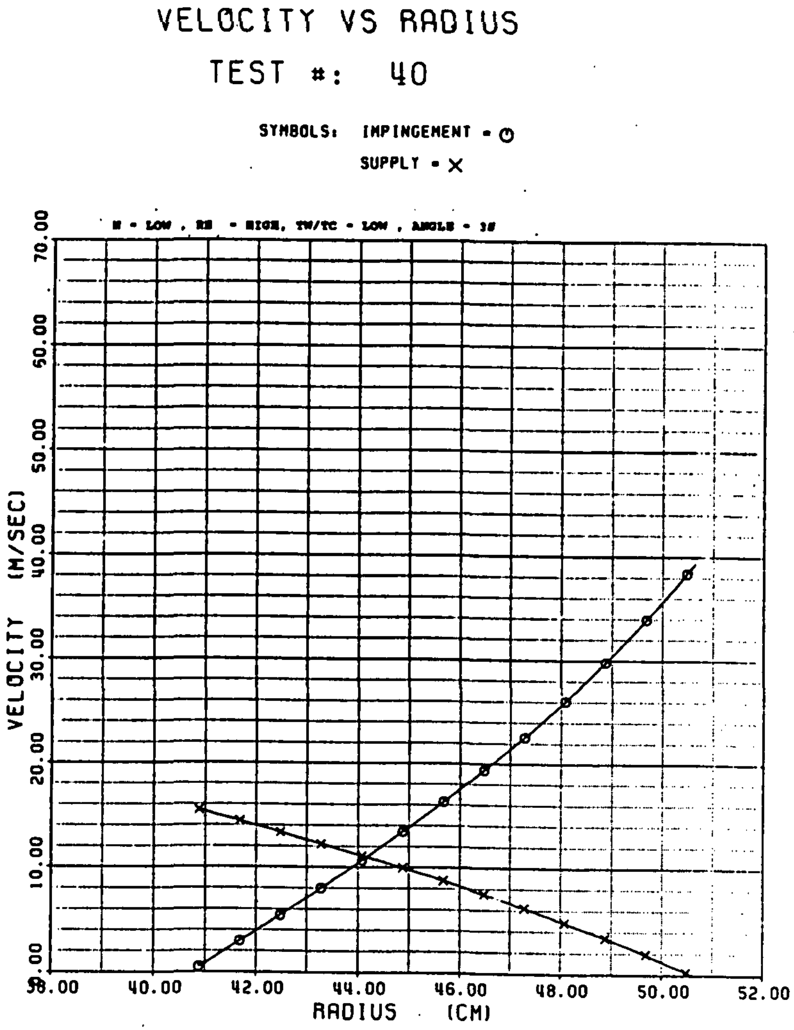

Figure 10A

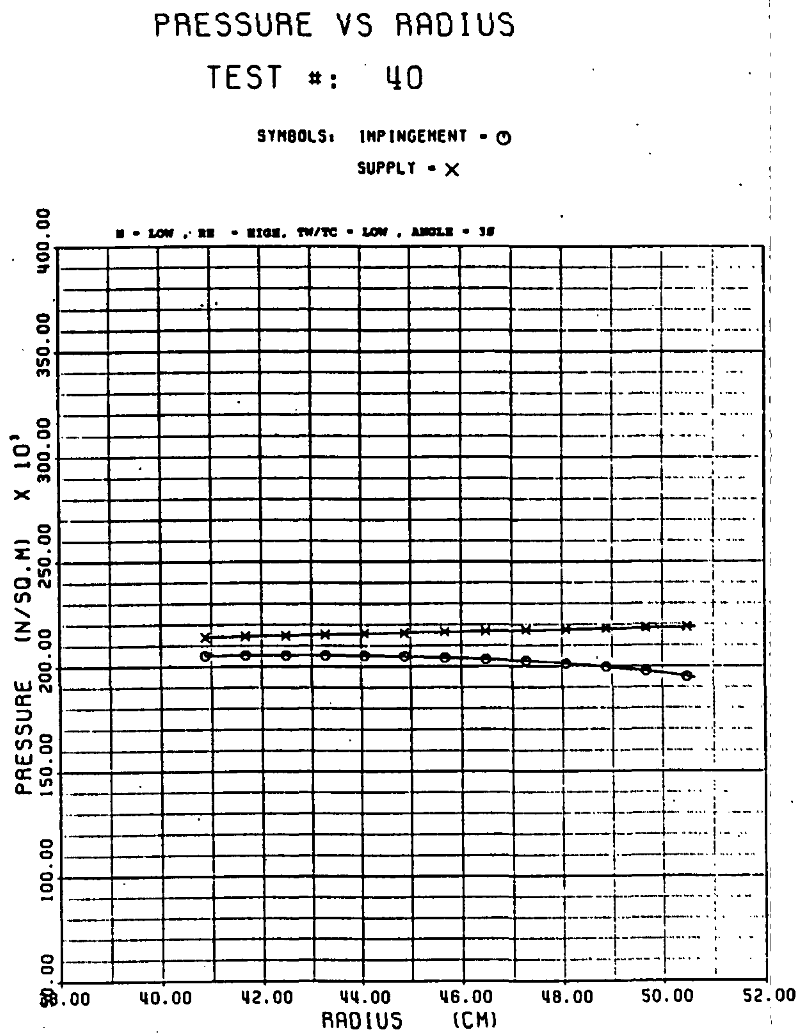

Figure 10B

ORIGINAL PAGE IS
OF POOR QUALITY

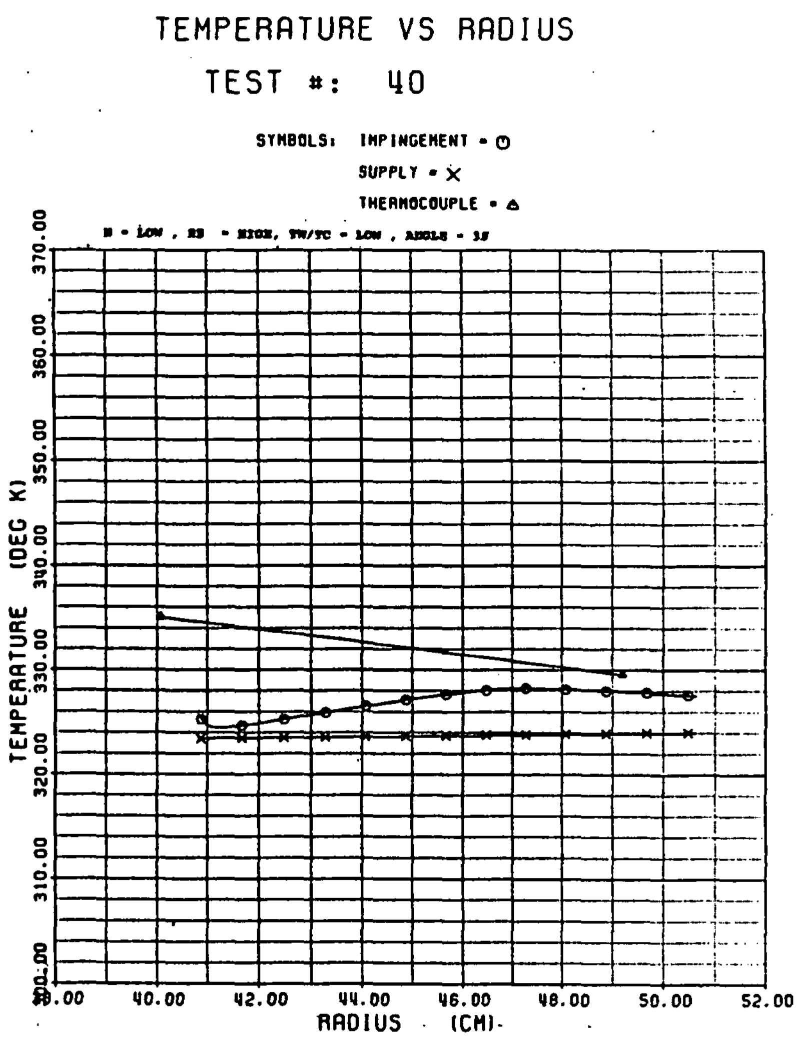

Figure 10C

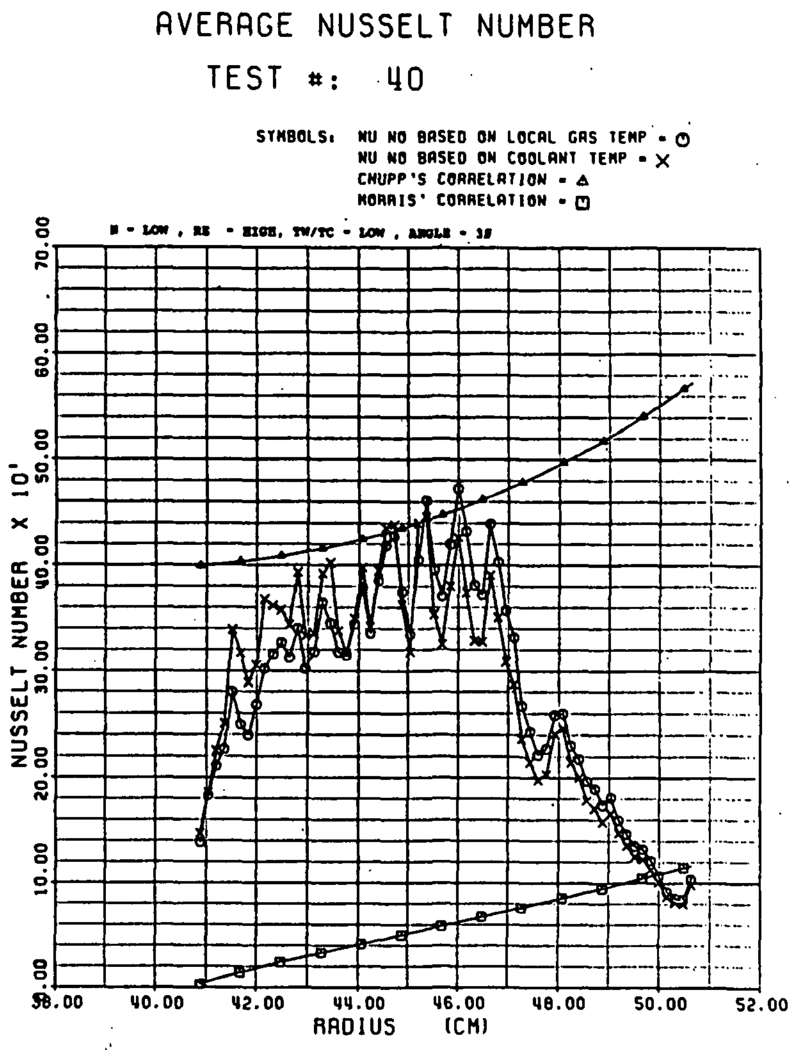

Figure 10D

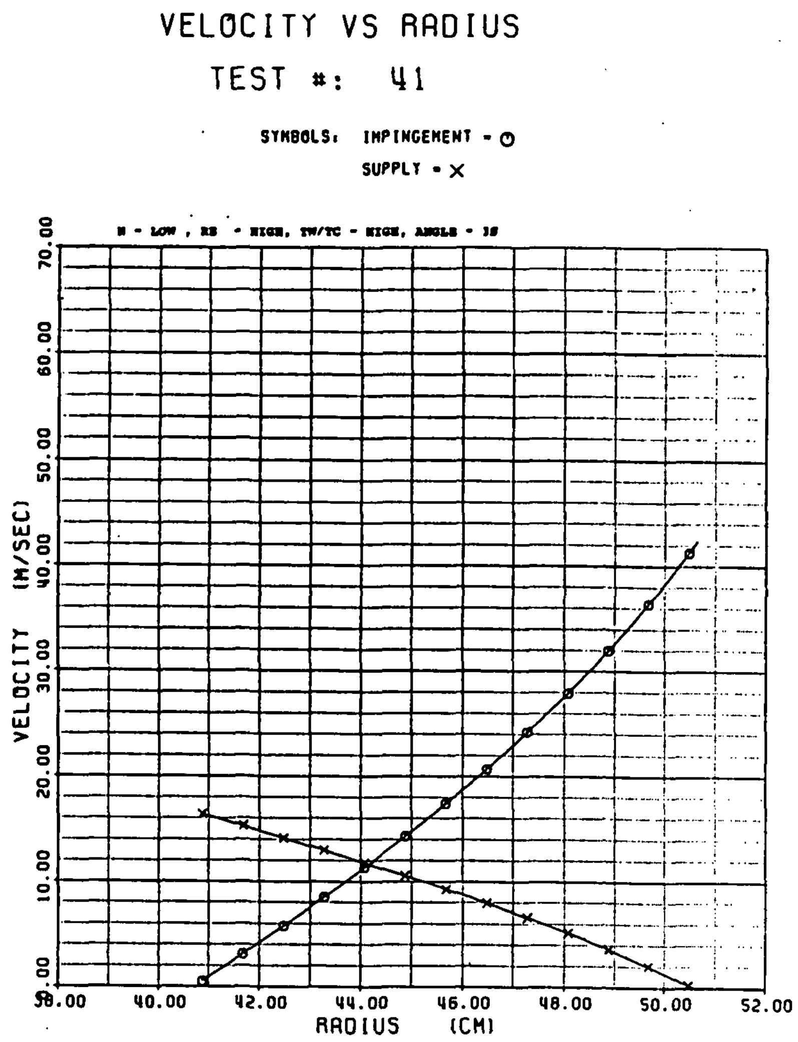

Figure 11A

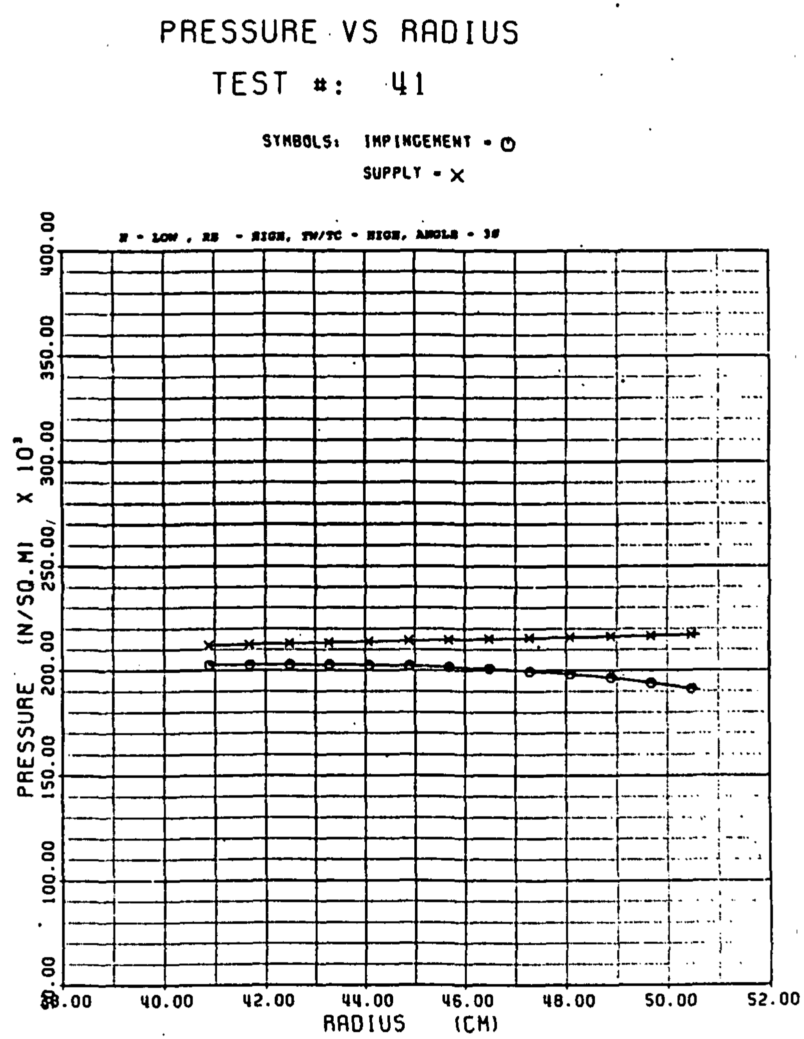

Figure 11B

ORIGINAL PAGE IS
OF POOR QUALITY

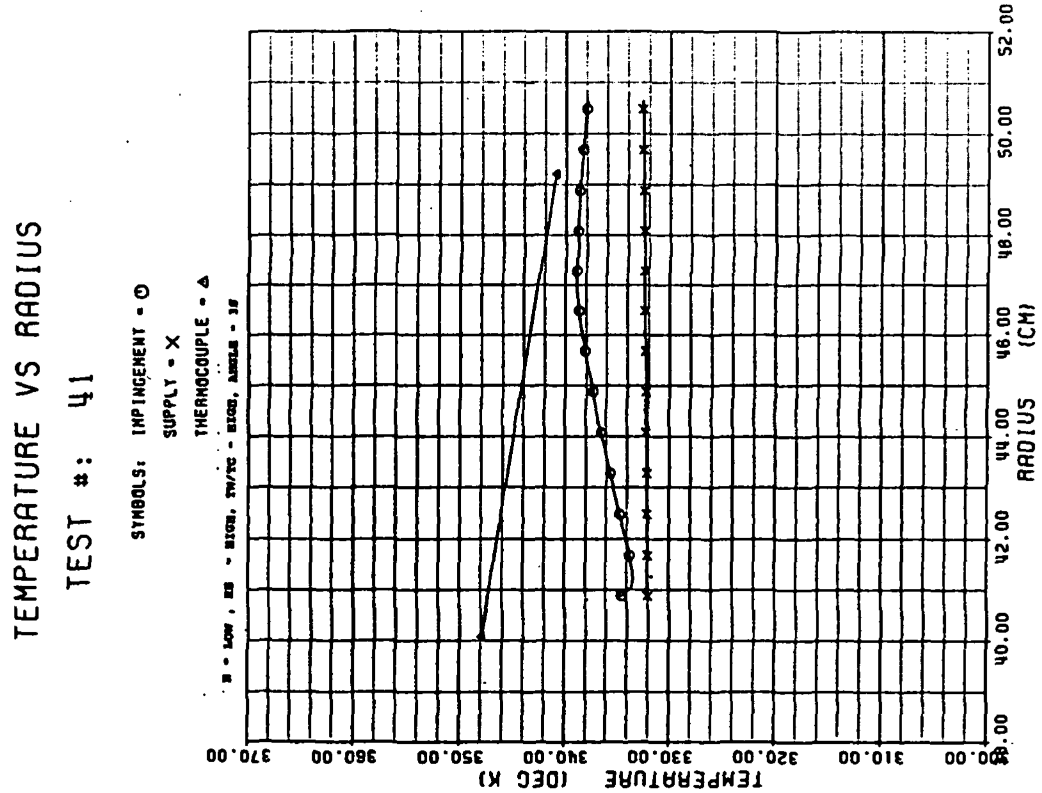

Figure 11C

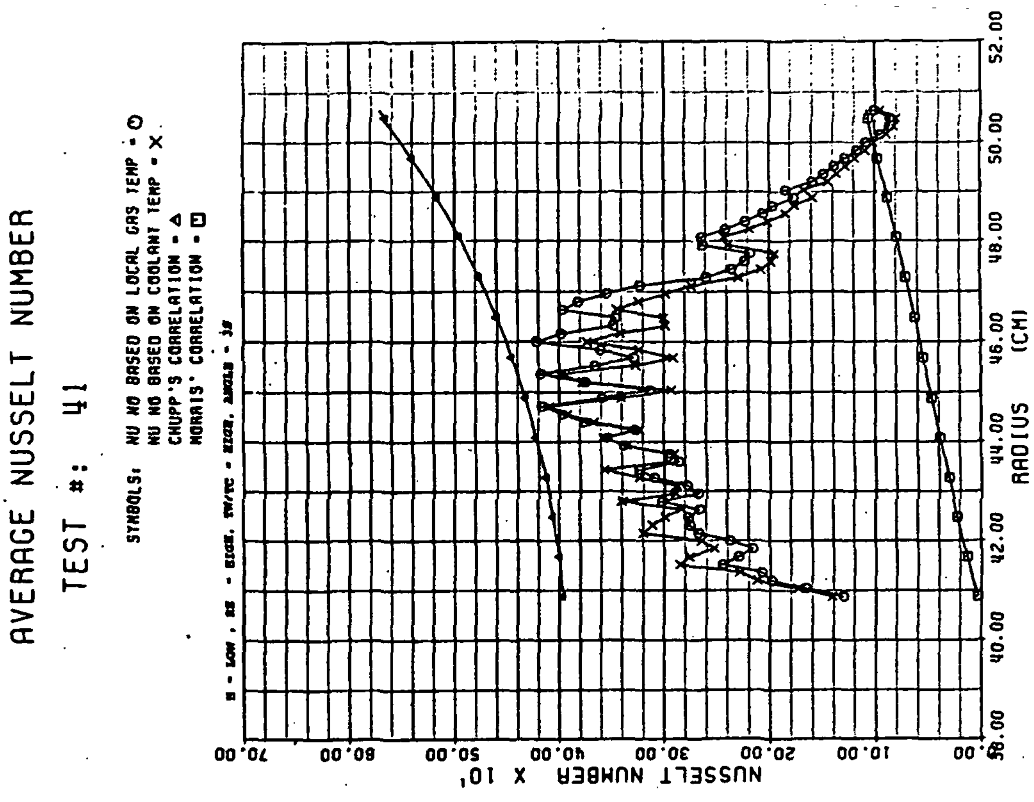

Figure 11D

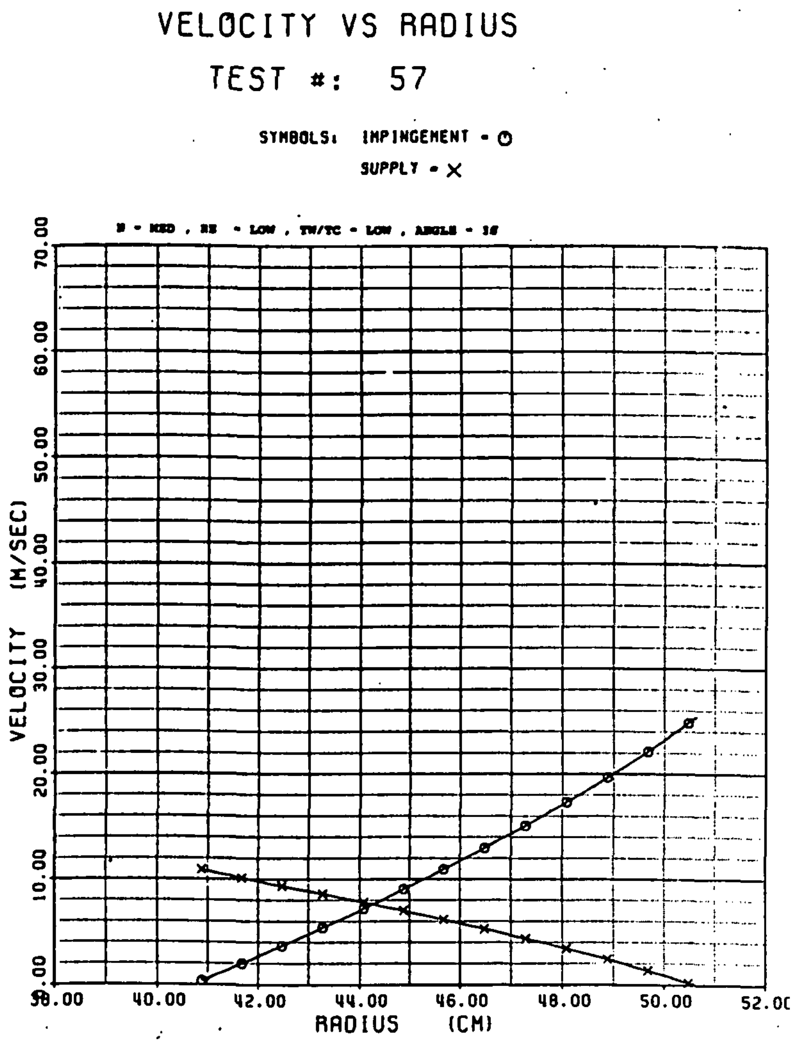

Figure 12A

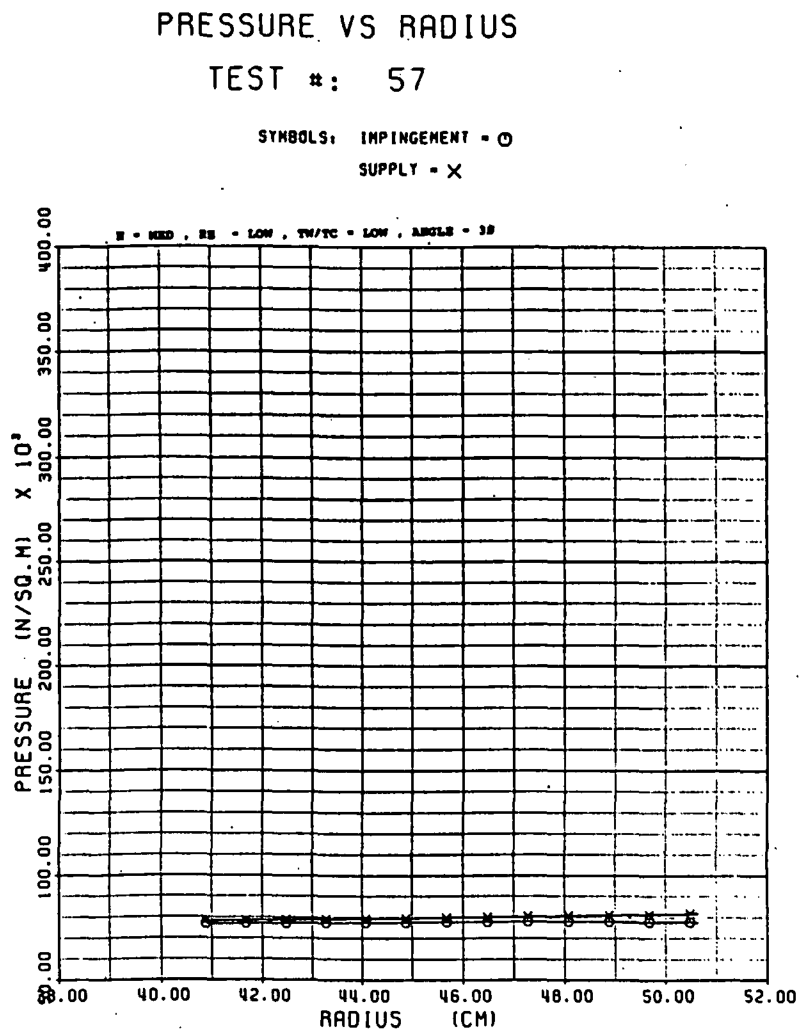

Figure 12B

ORIGINAL PAGE IS
OF POOR QUALITY

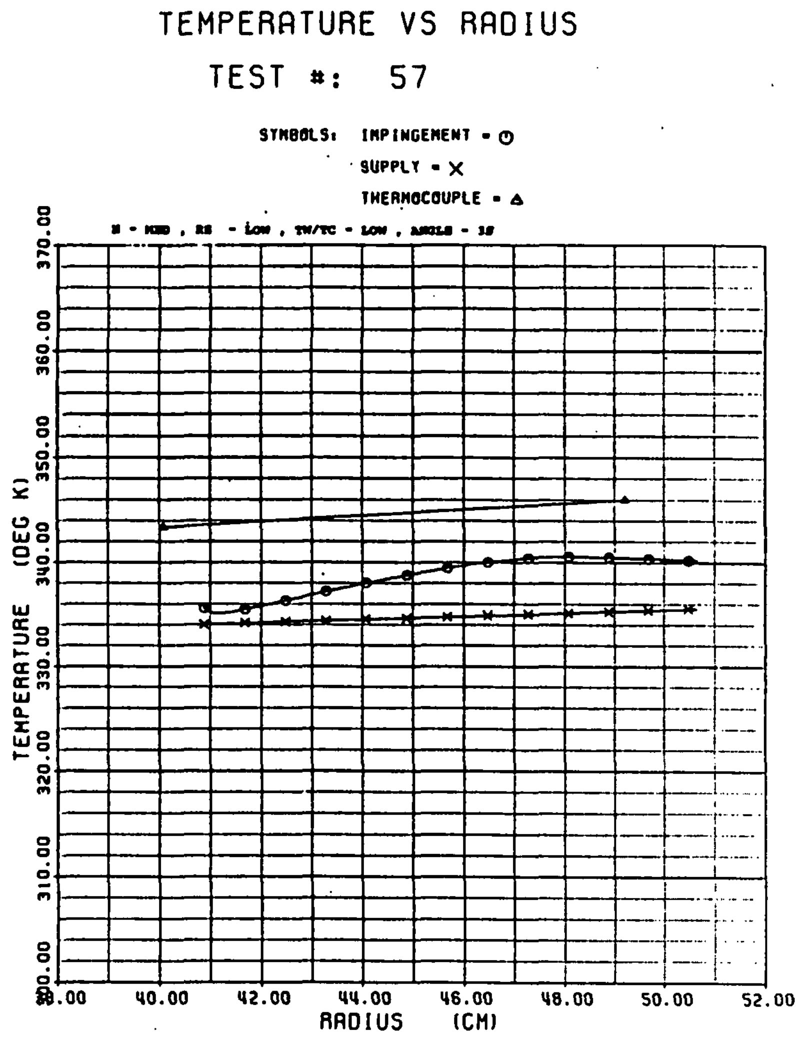

Figure 12C

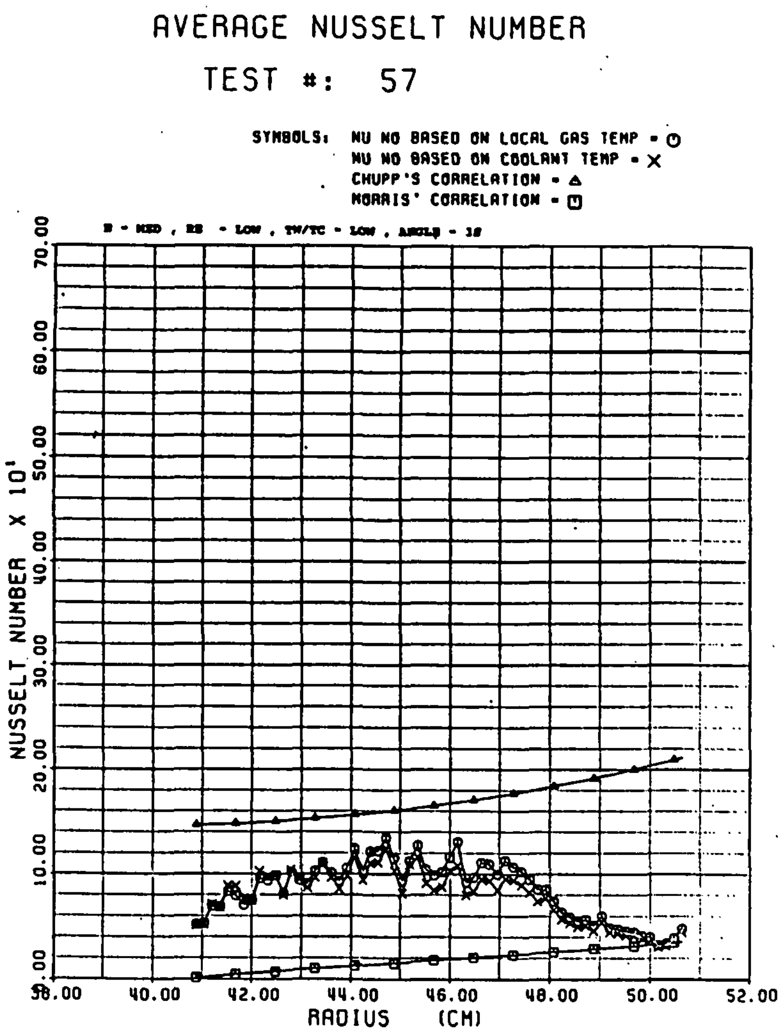

Figure 12D

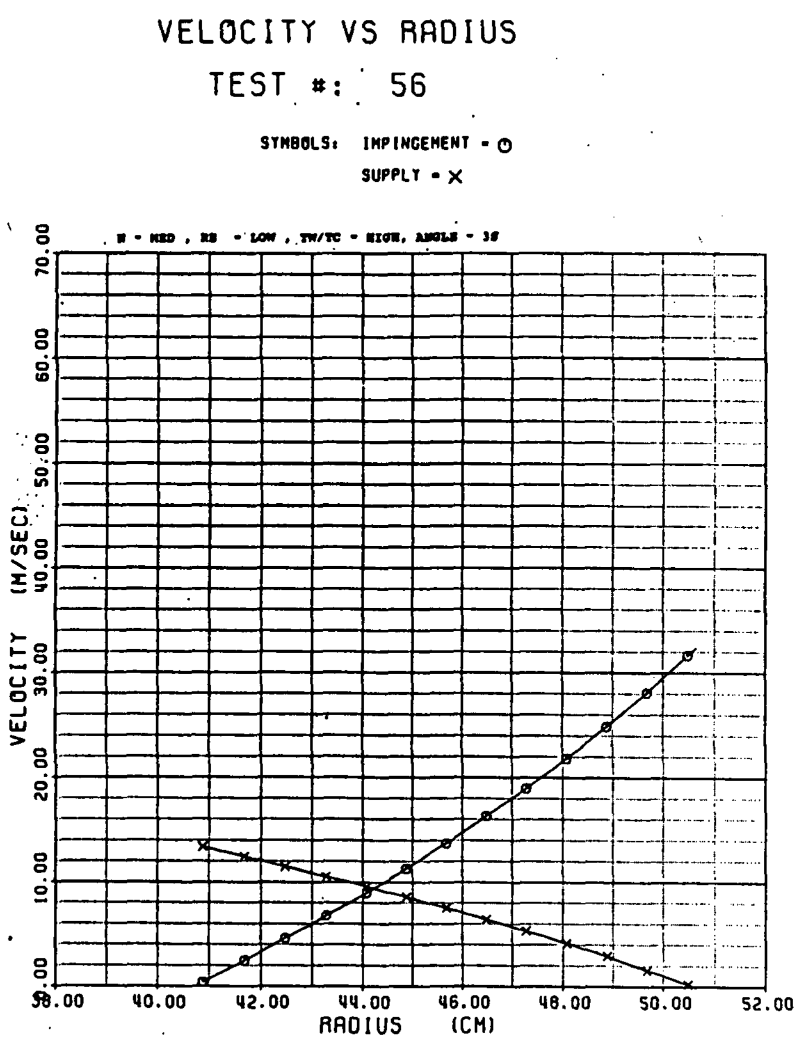

Figure 13A

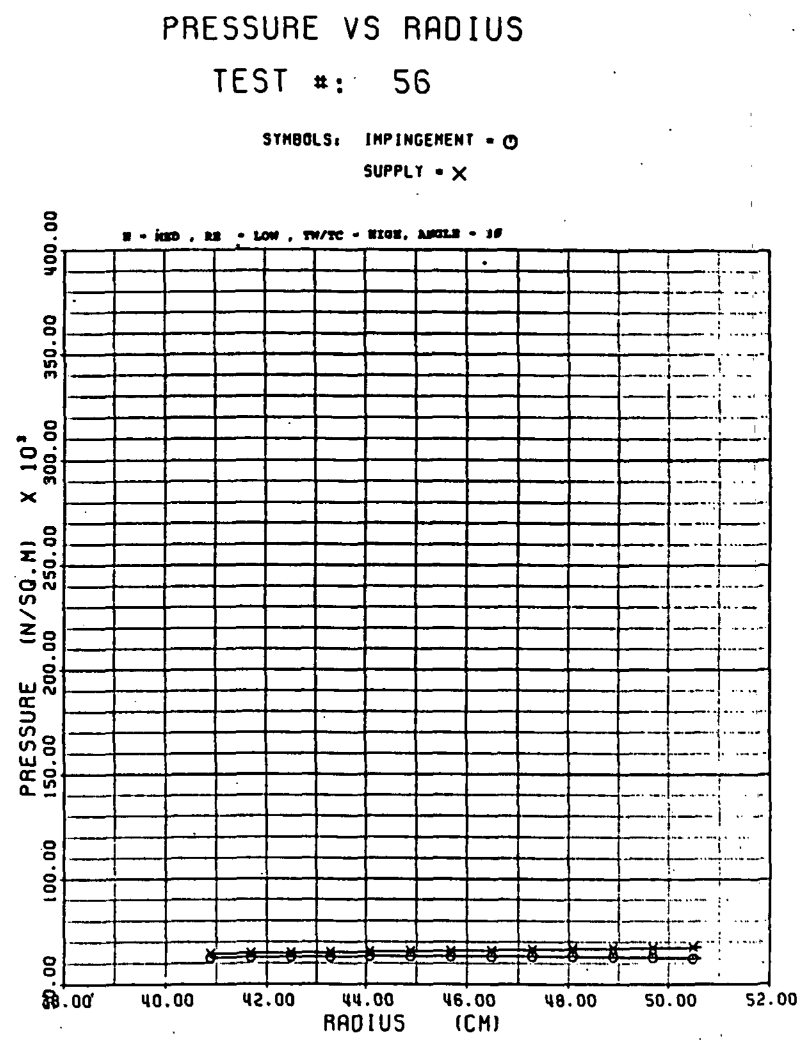

Figure 13B

ORIGINAL PAGE IS
OF POOR QUALITY

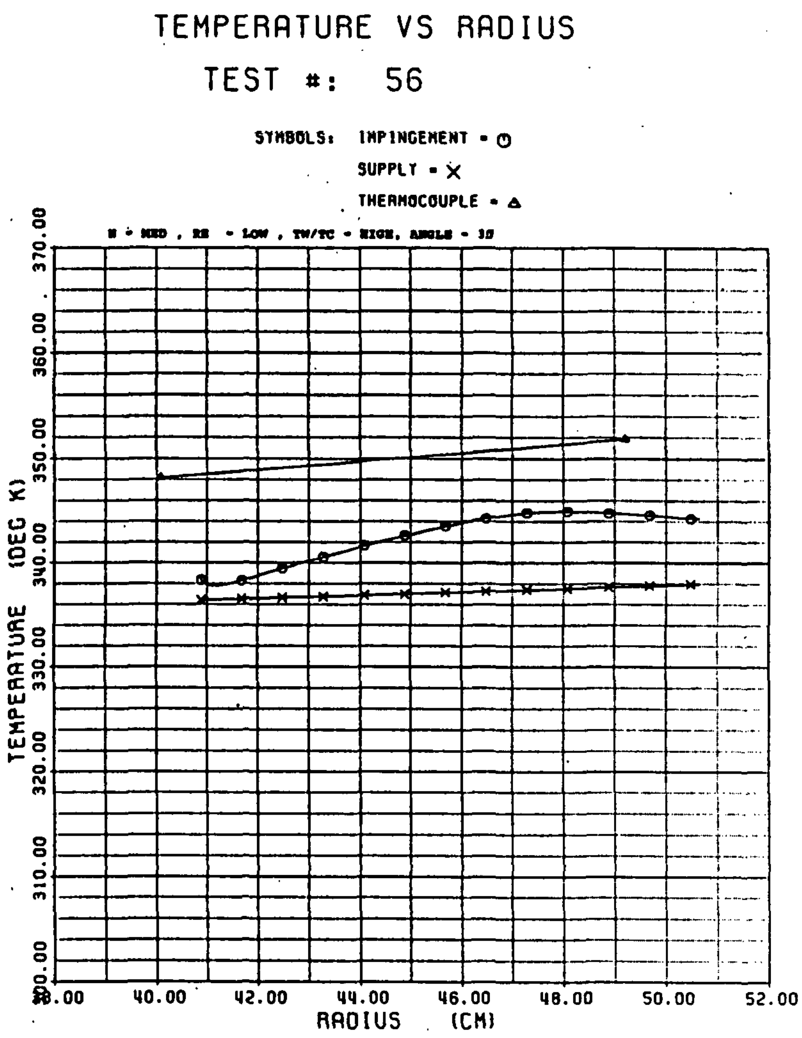

Figure 13C

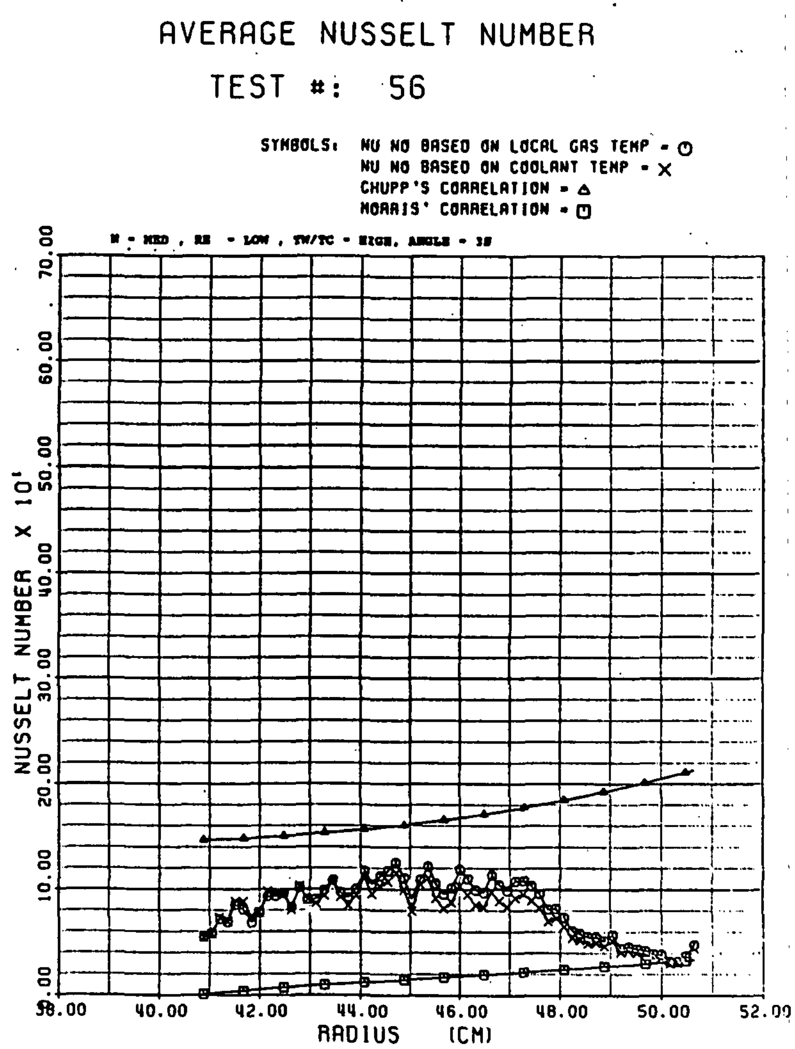

Figure 13D

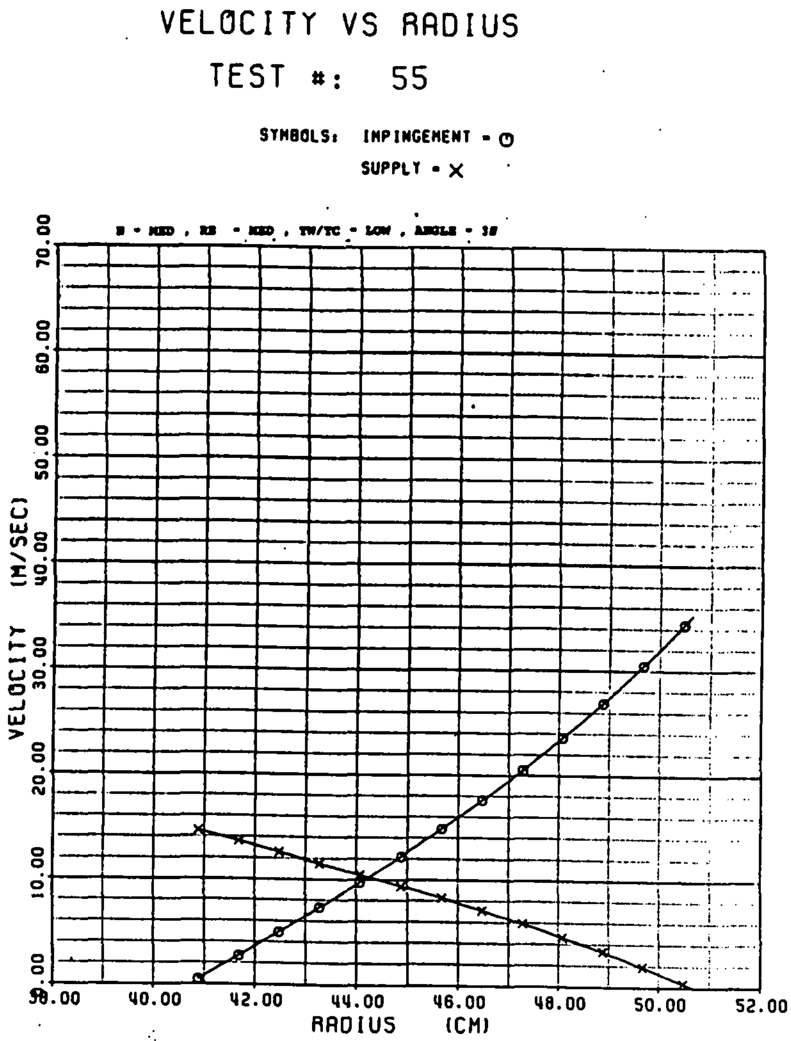

Figure 14A

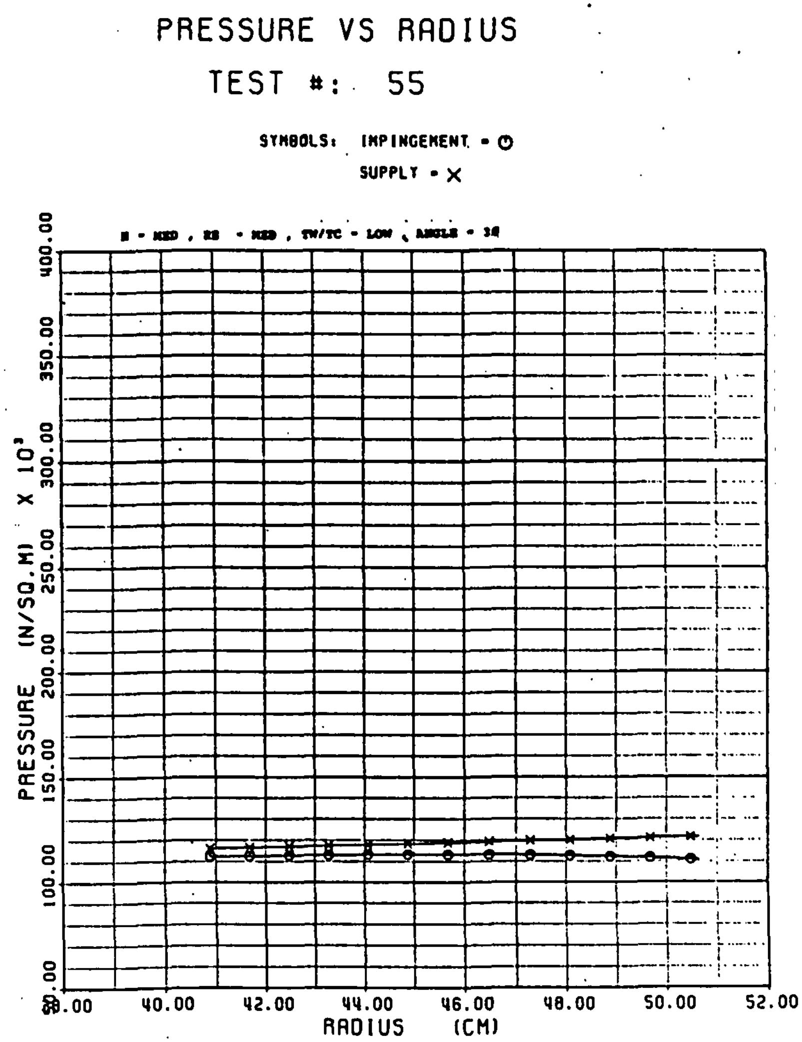

Figure 14B

ORIGINAL PAGE IS
OF POOR QUALITY

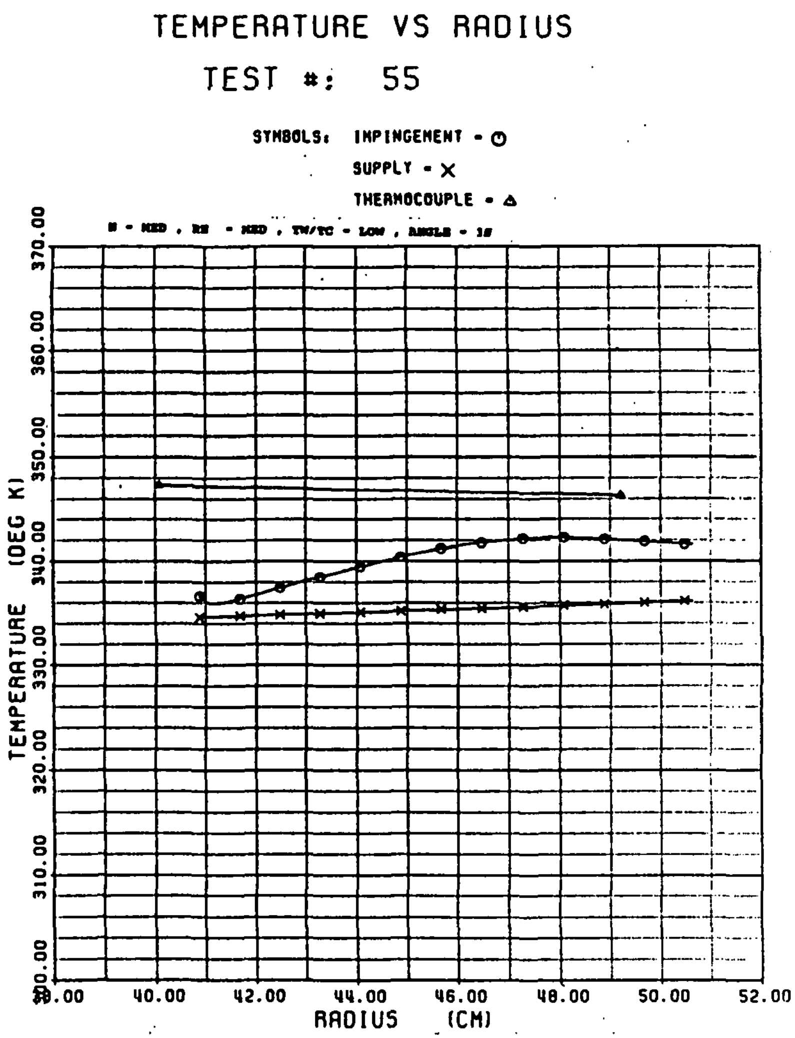

Figure 14C

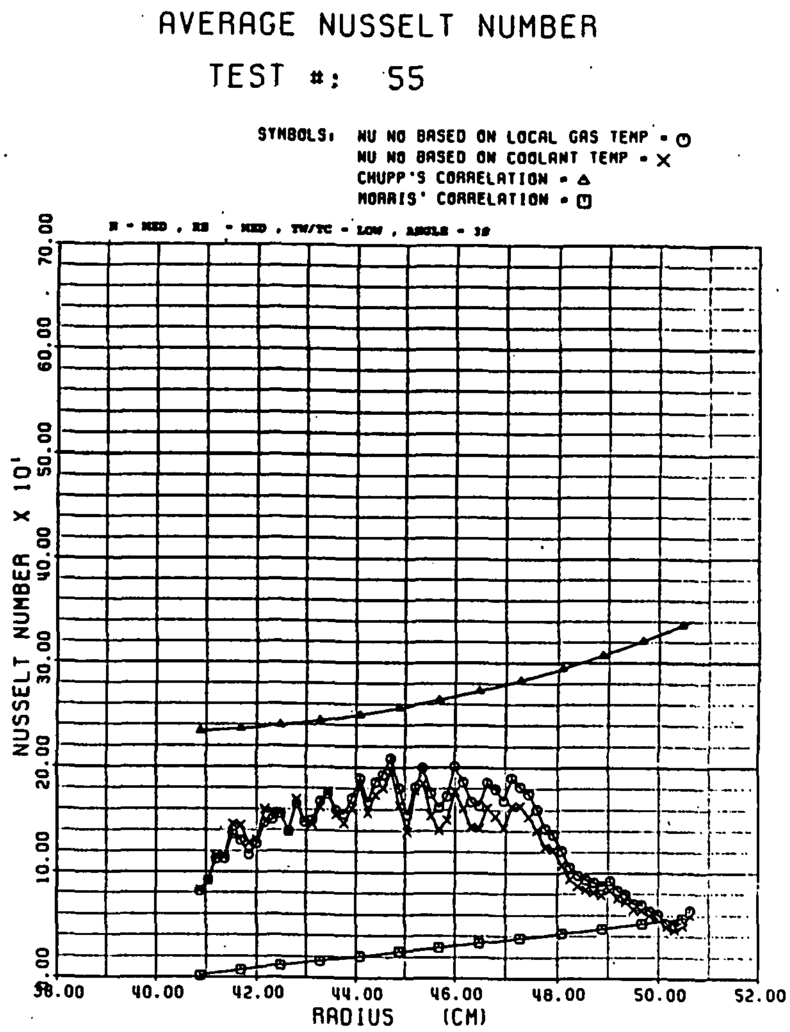

Figure 14D

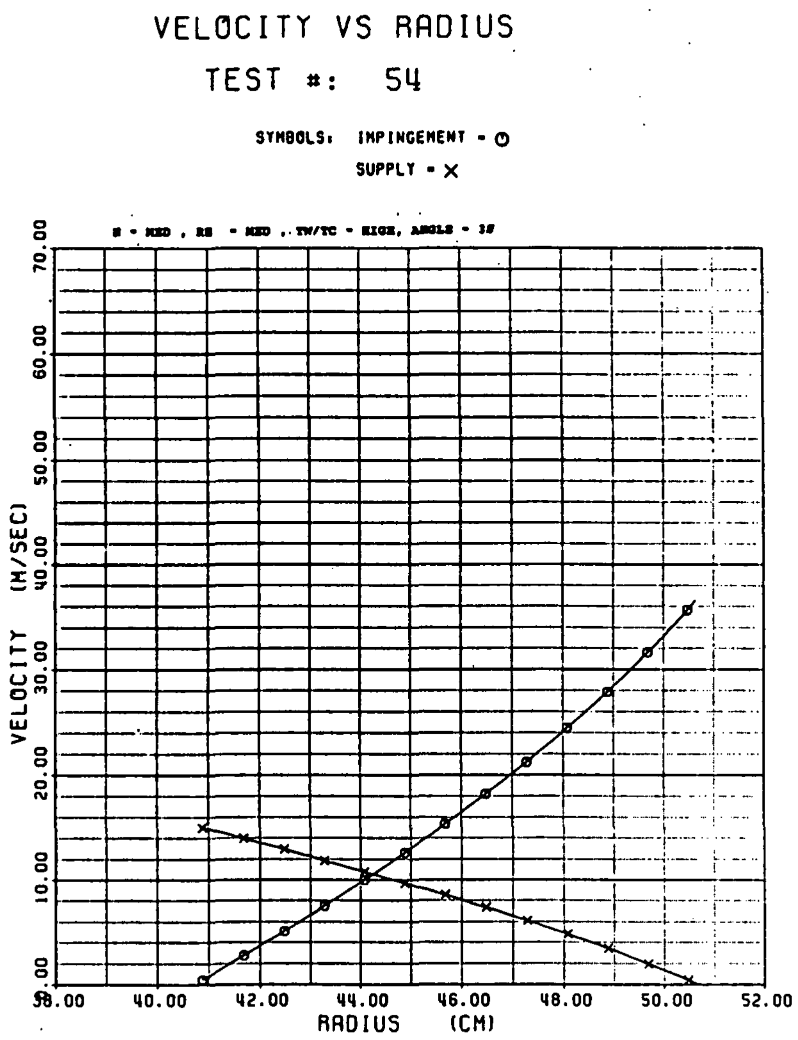

Figure 15A

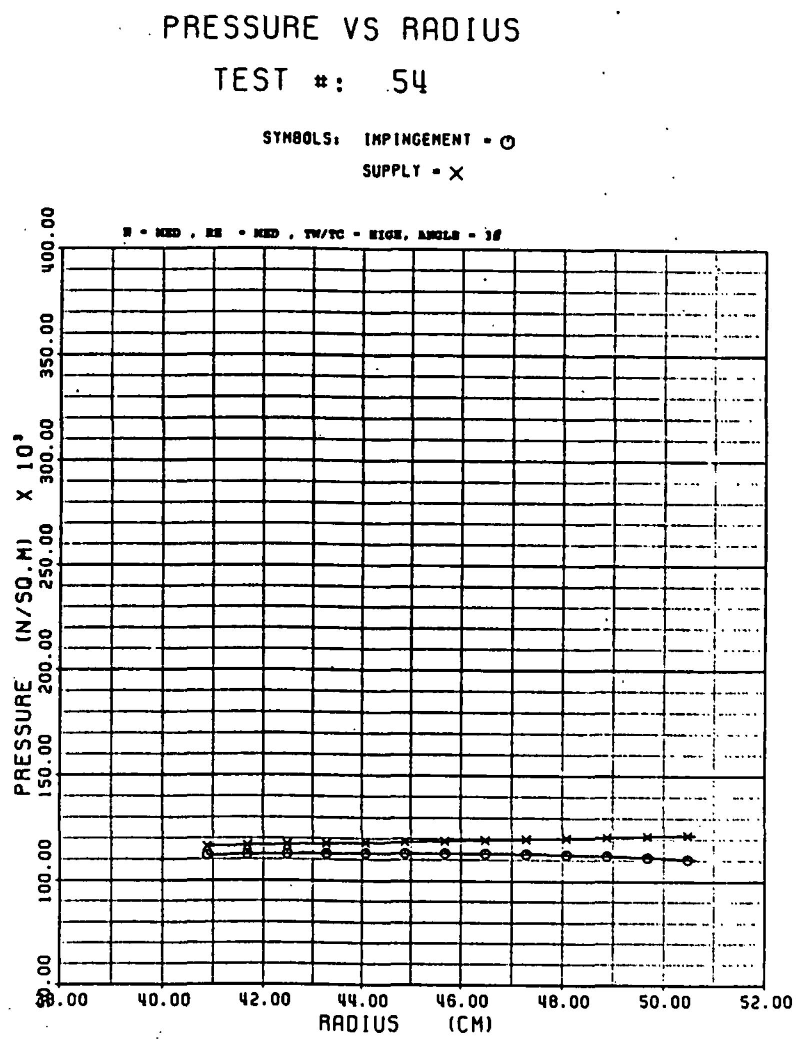

Figure 15B

ORIGINAL PAGE IS OF POOR QUALITY

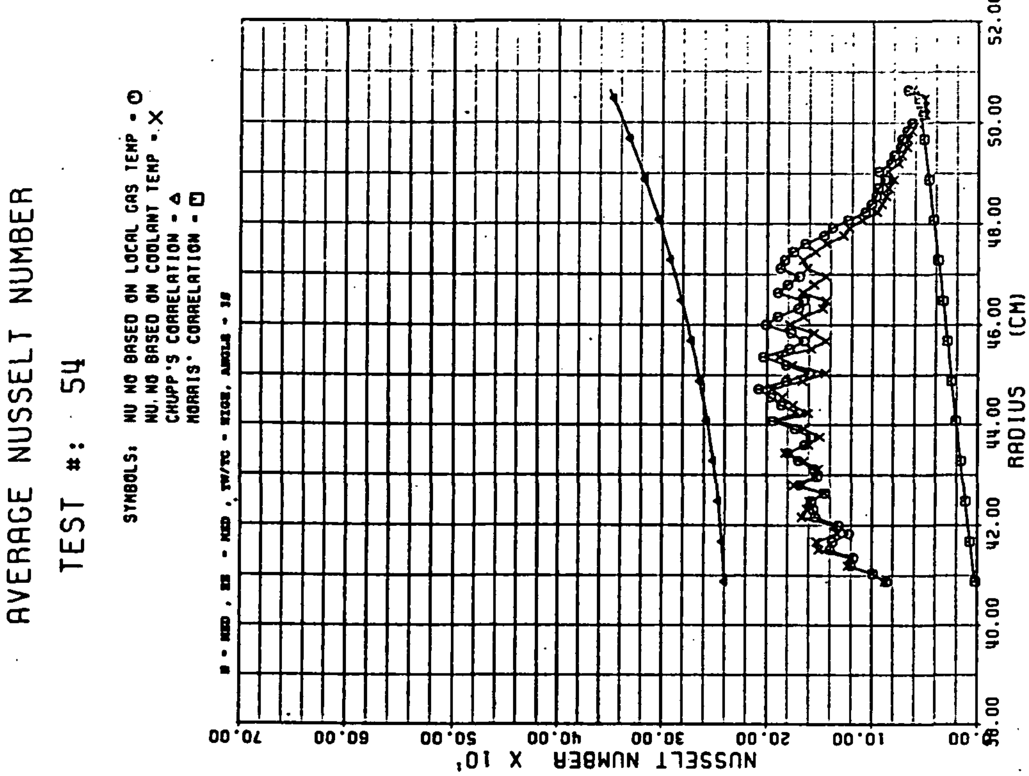

Figure 15D

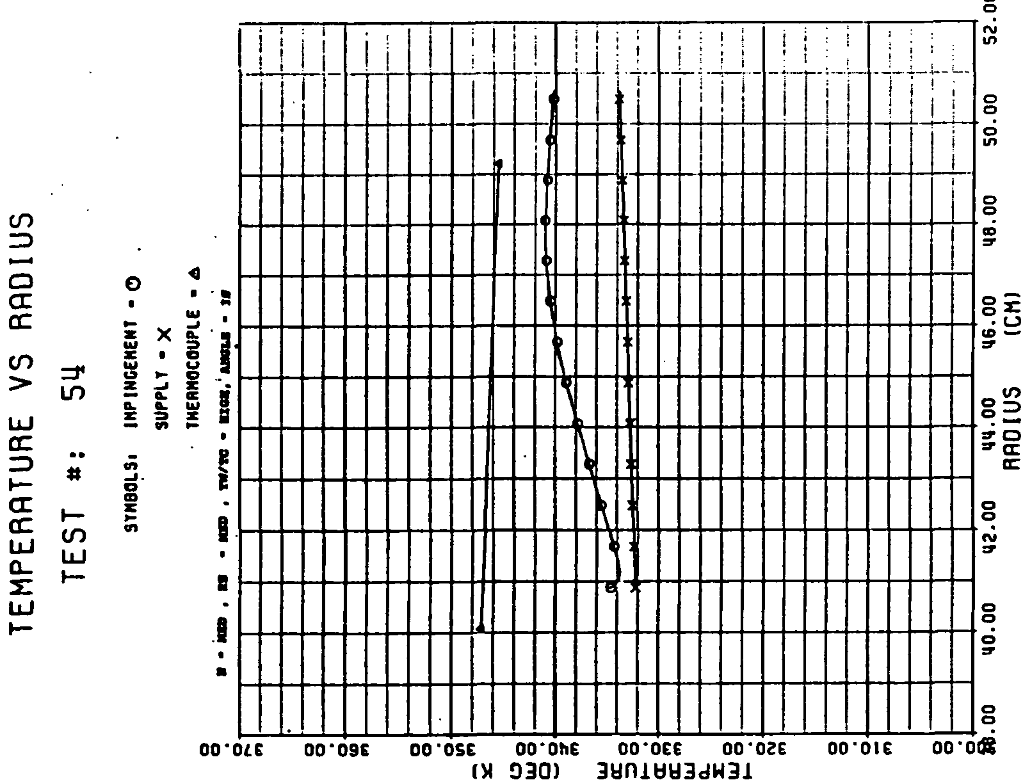

Figure 15C

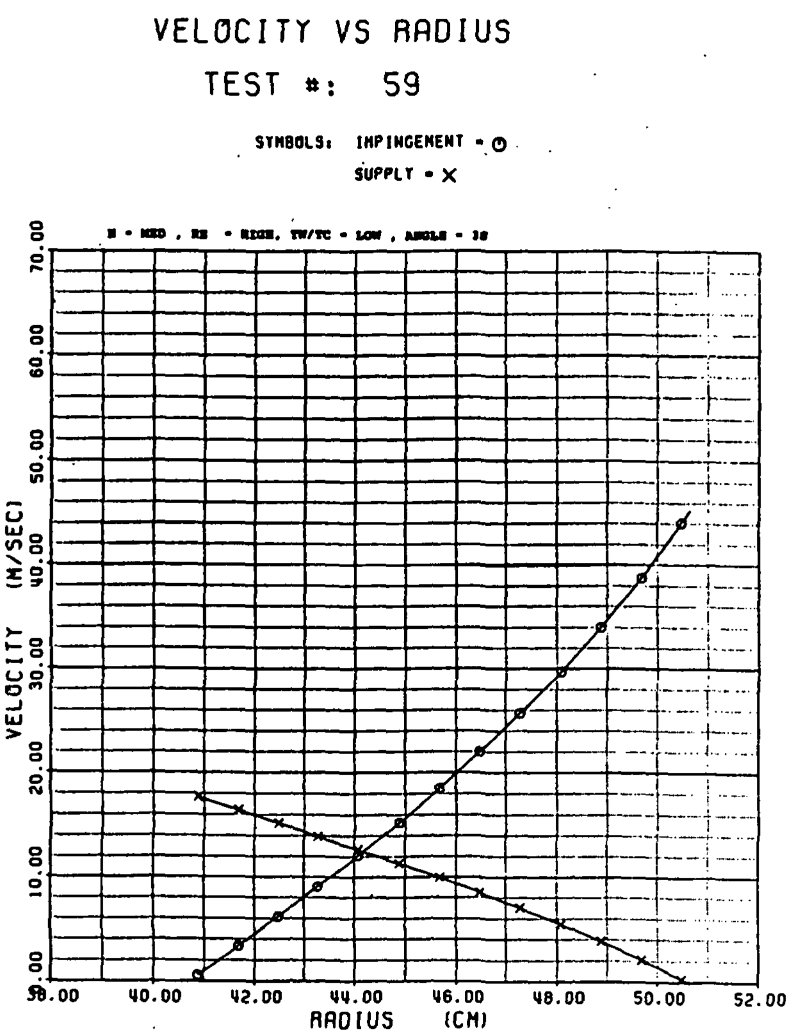

Figure 16A

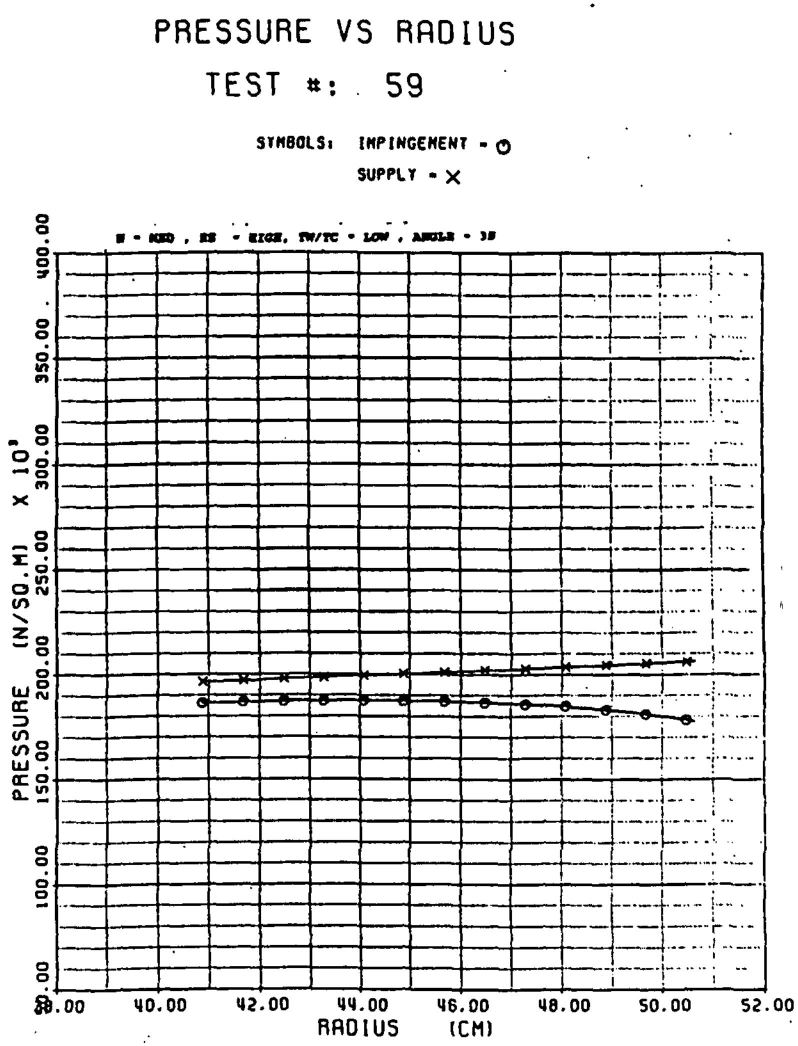

Figure 16B

ORIGINAL PAGE IS
OF POOR QUALITY

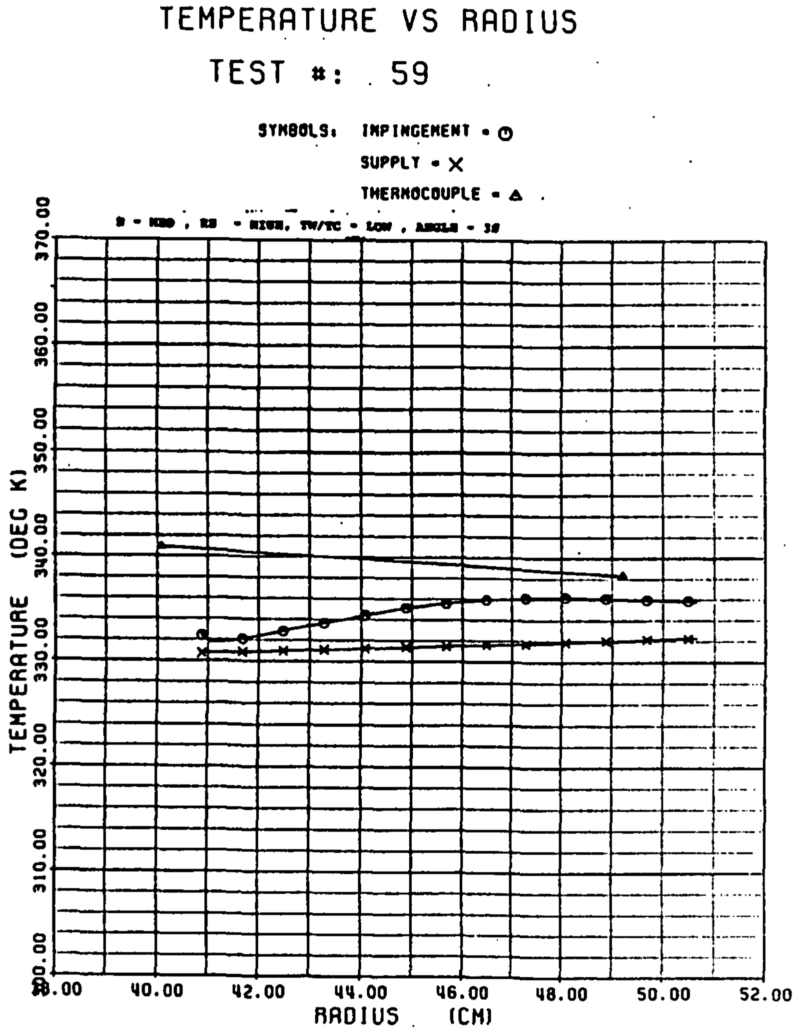

Figure 16C

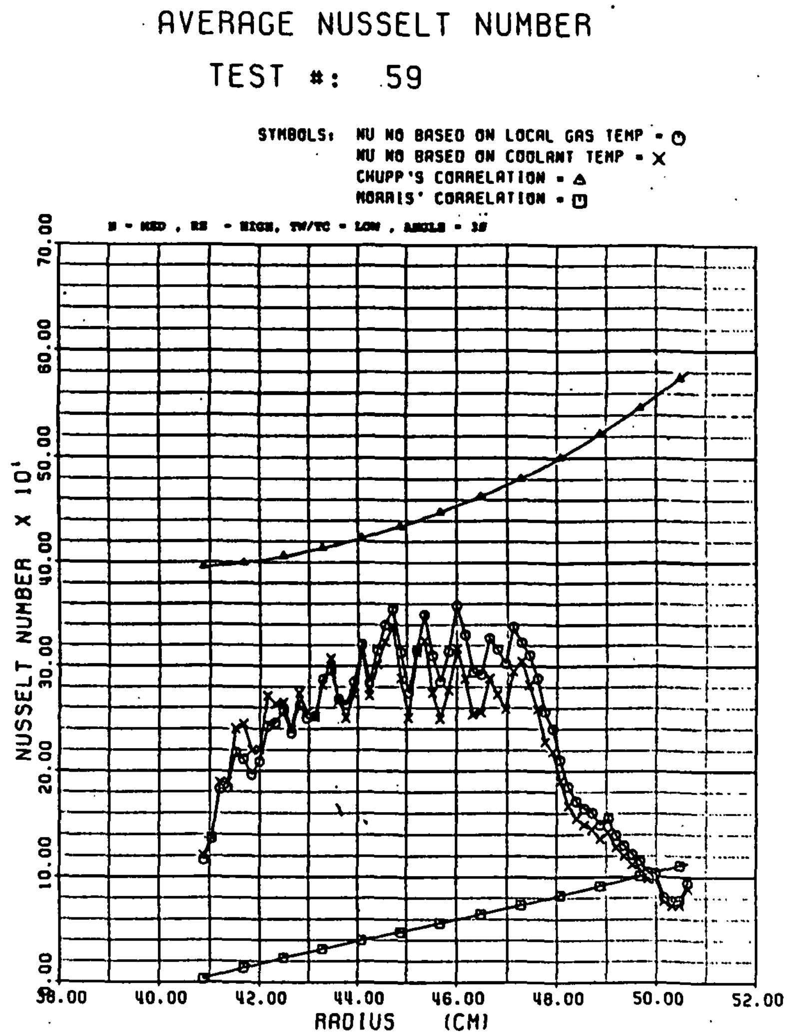

Figure 16D

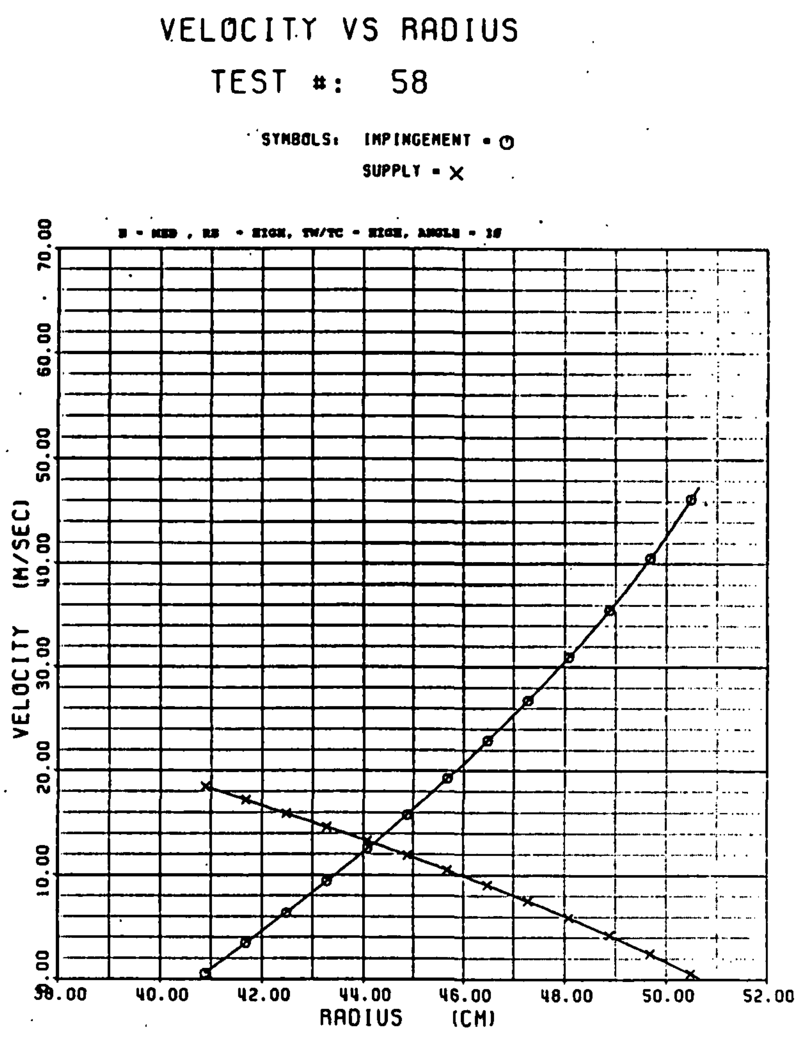

Figure 17A

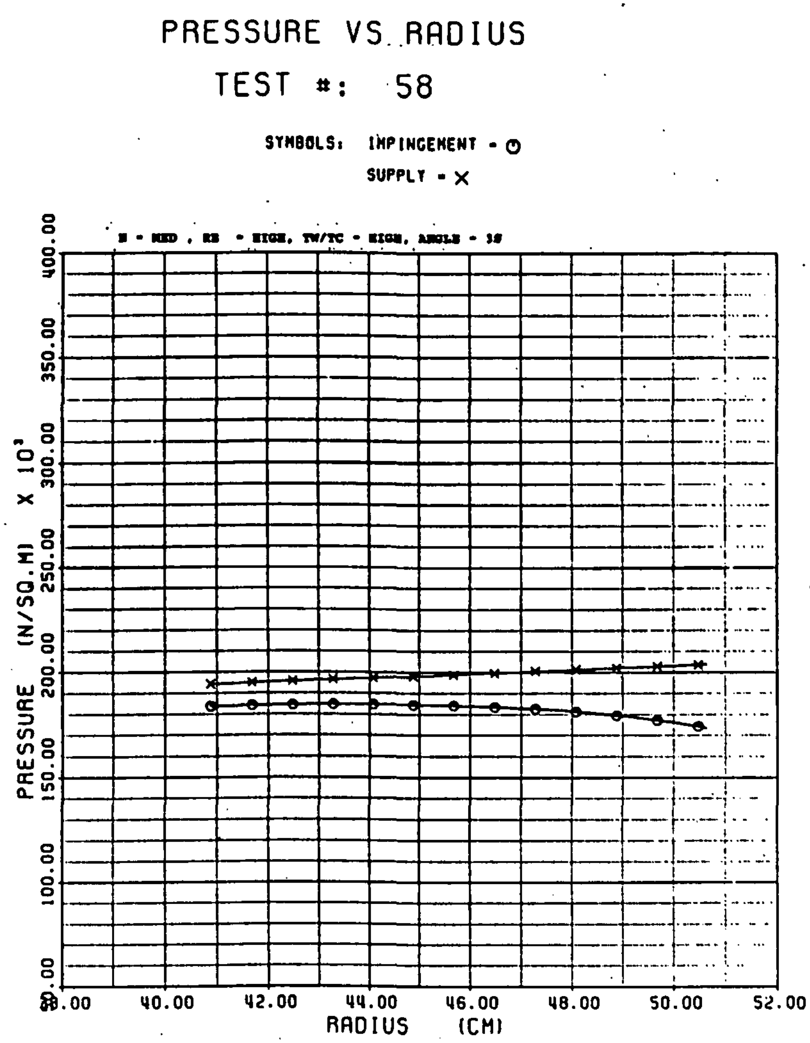

Figure 17B

ORIGINAL PAGE IS OF POOR QUALITY

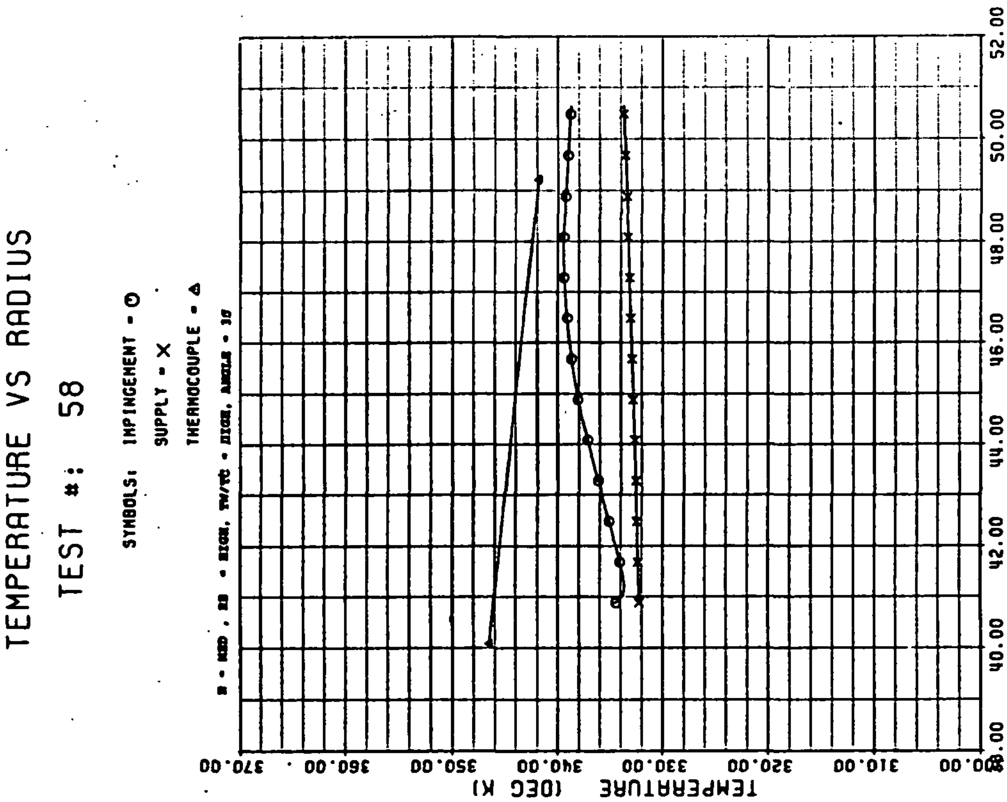

Figure 17C

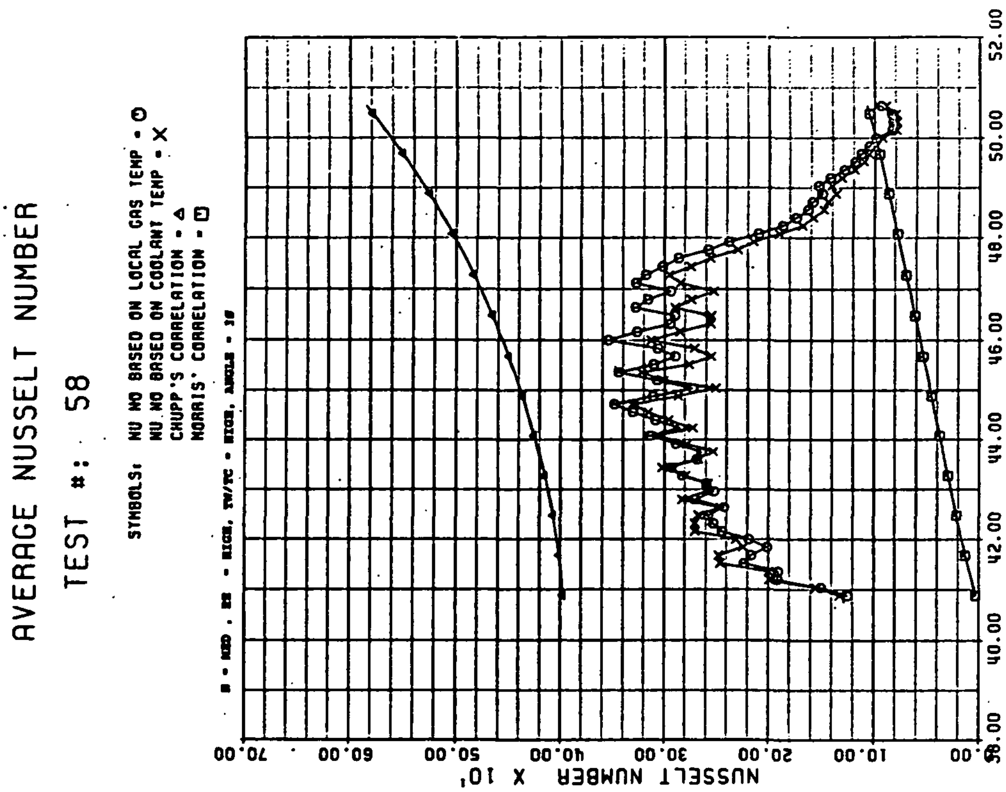

Figure 17D

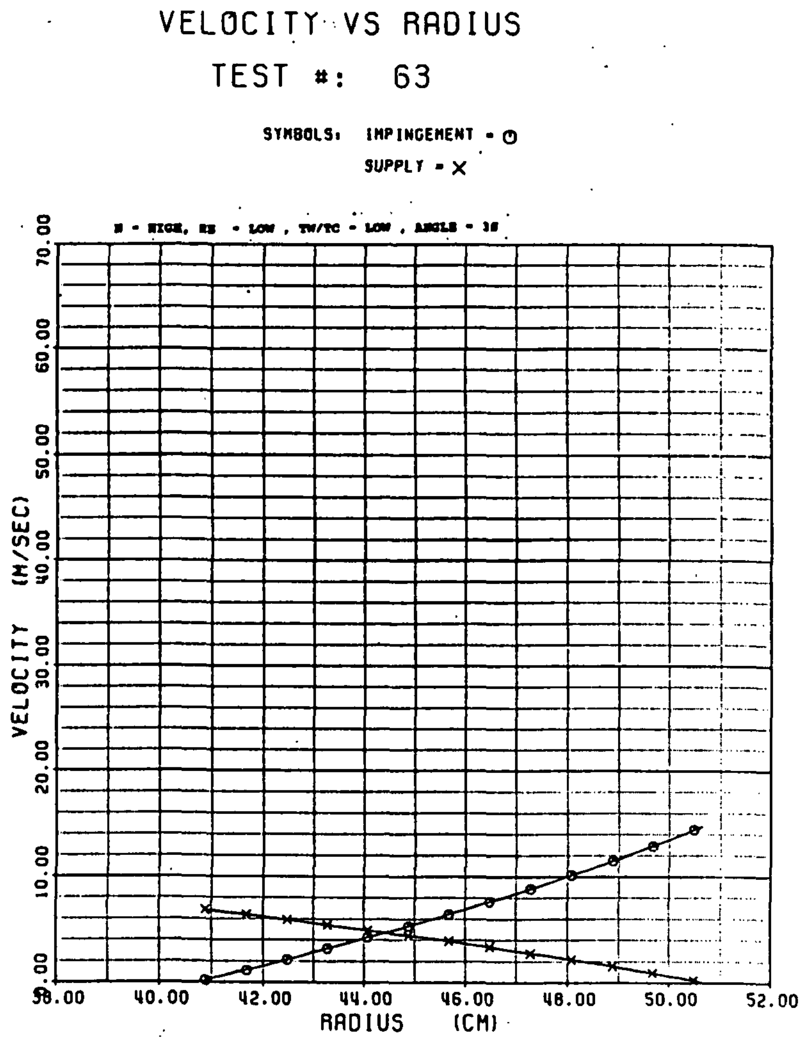

Figure 18A

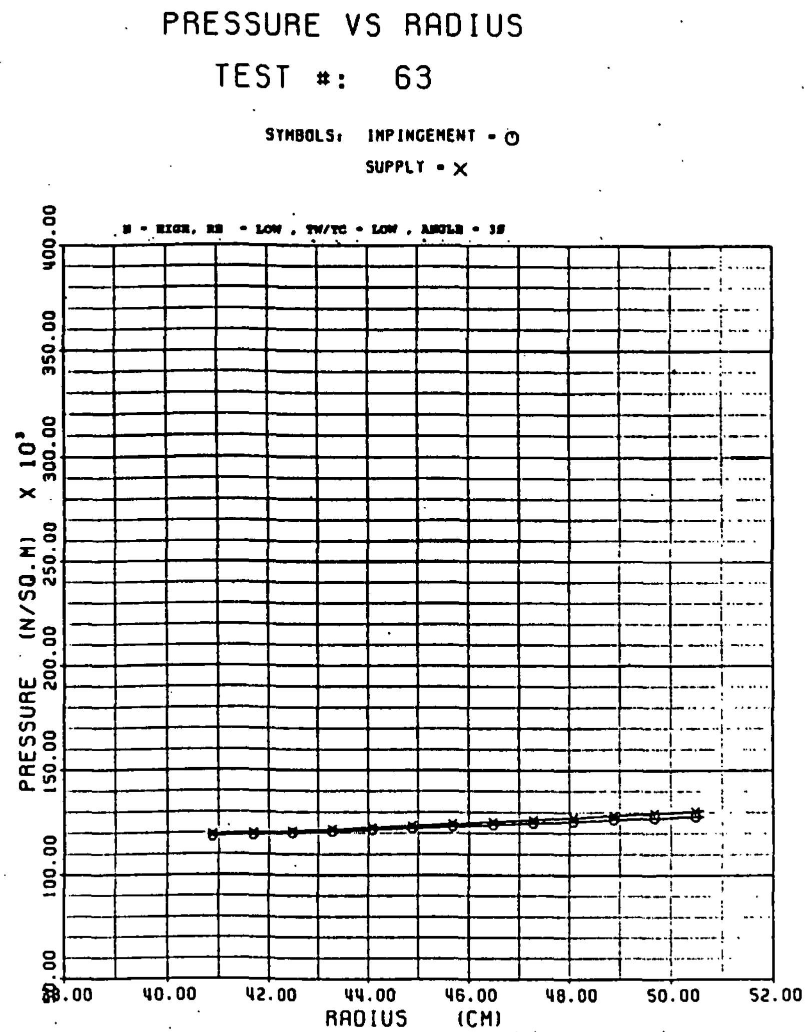

Figure 18B

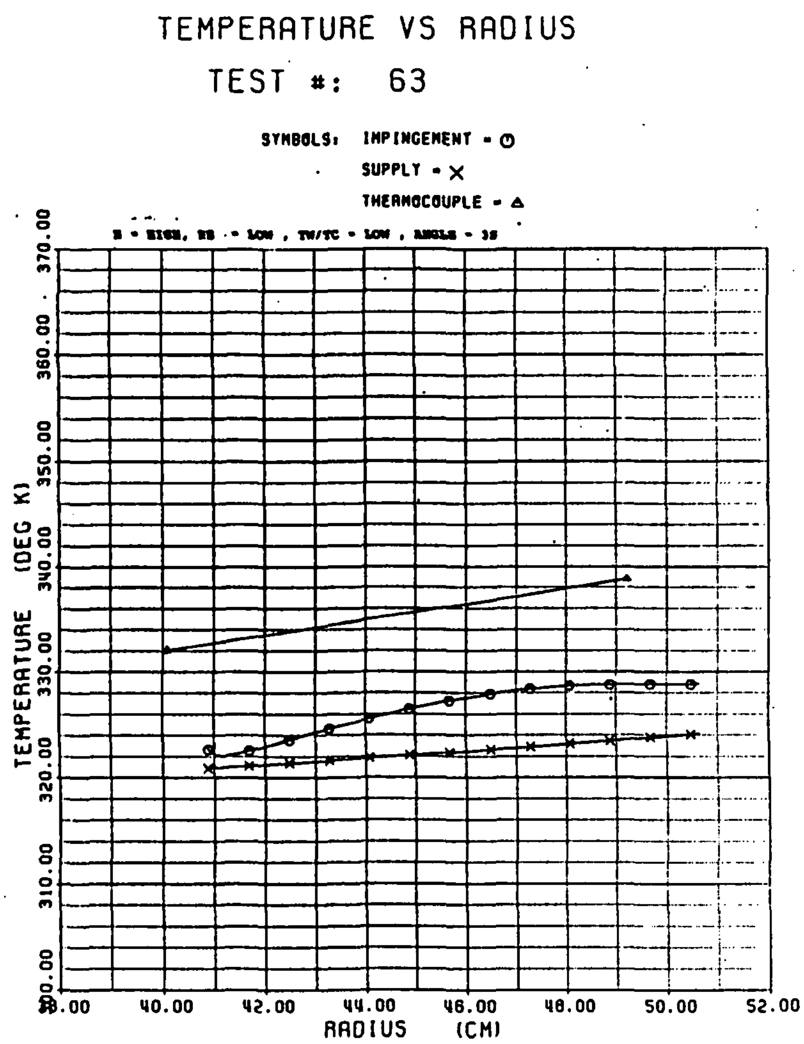

Figure 18C

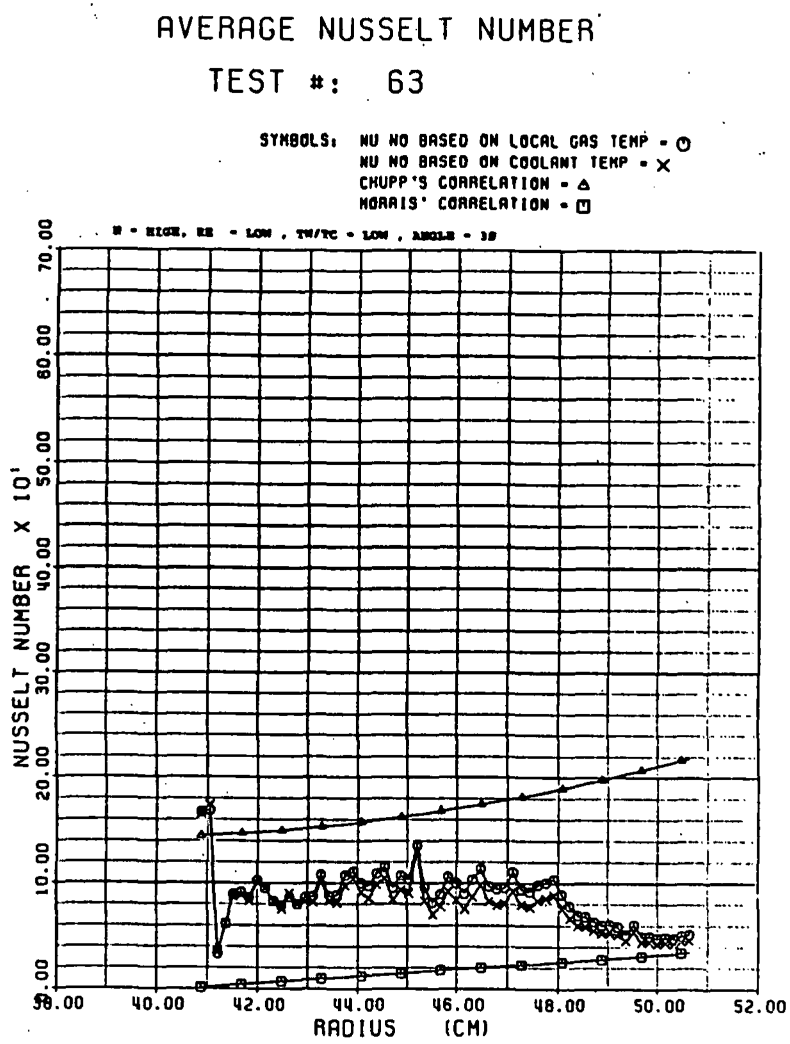

Figure 18D

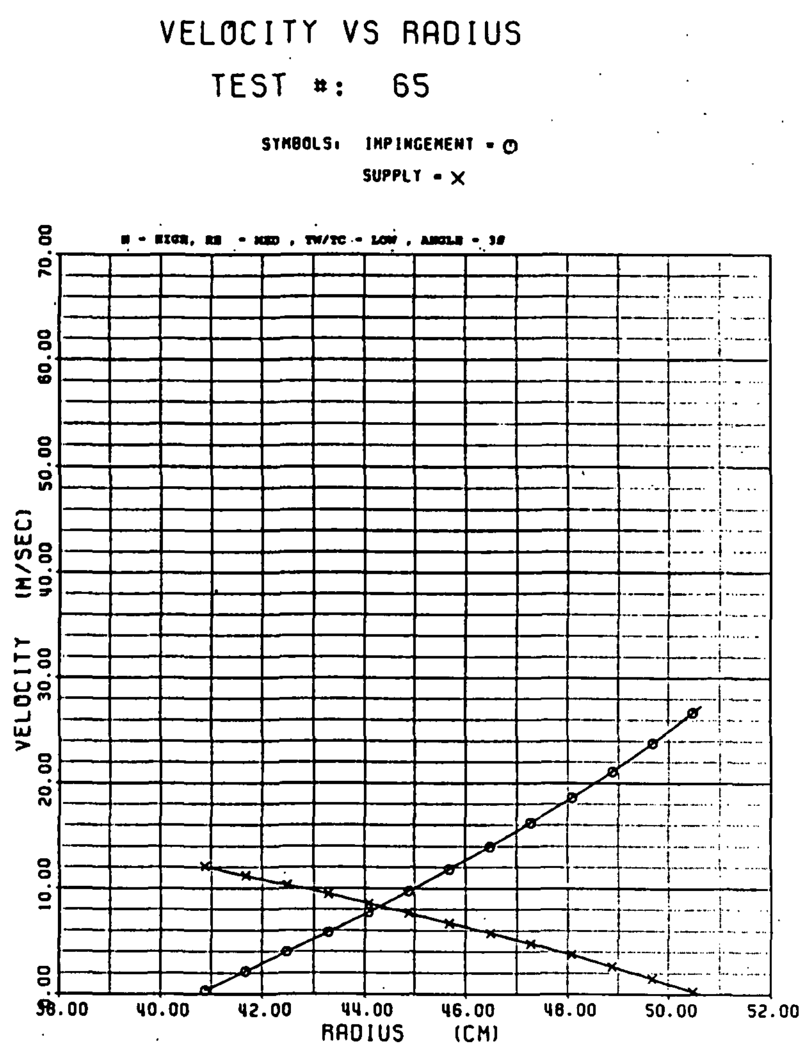

Figure 19A

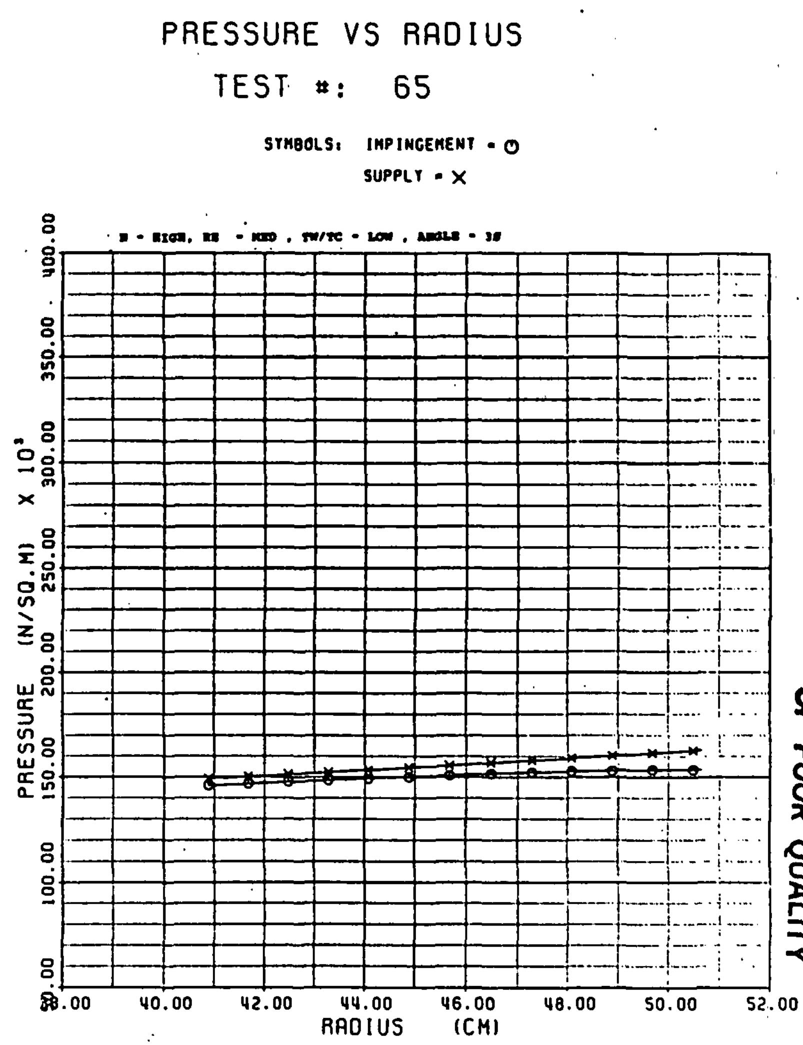

Figure 19B

ORIGINAL PAGE IS
OF POOR QUALITY

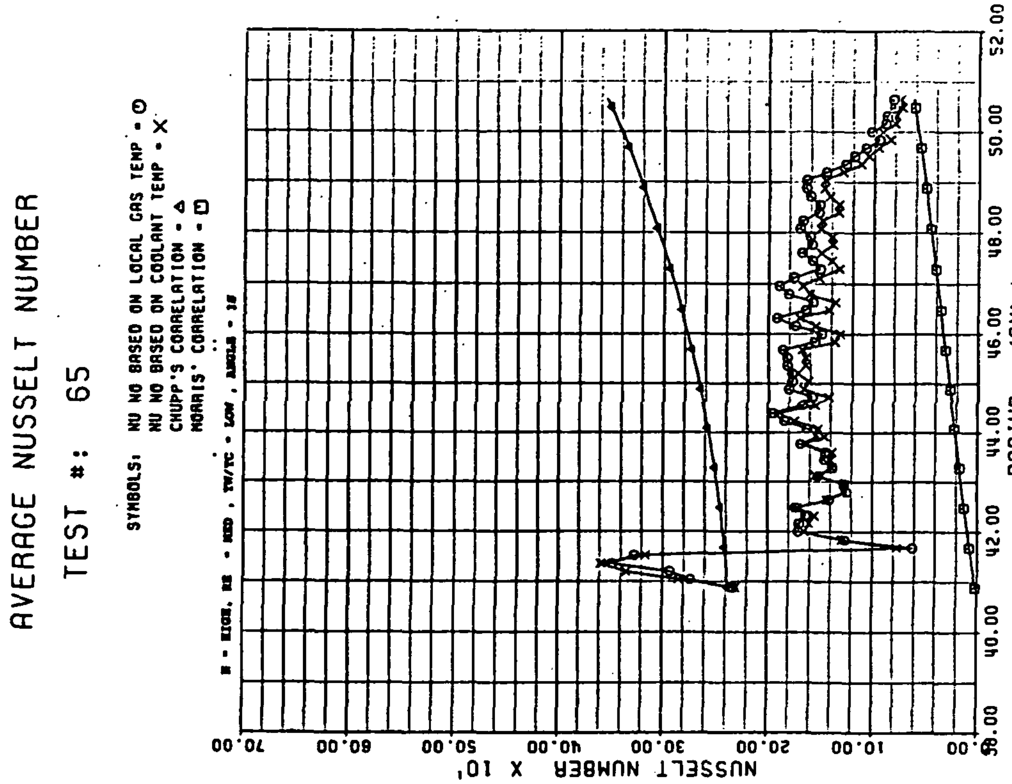

Figure 19D

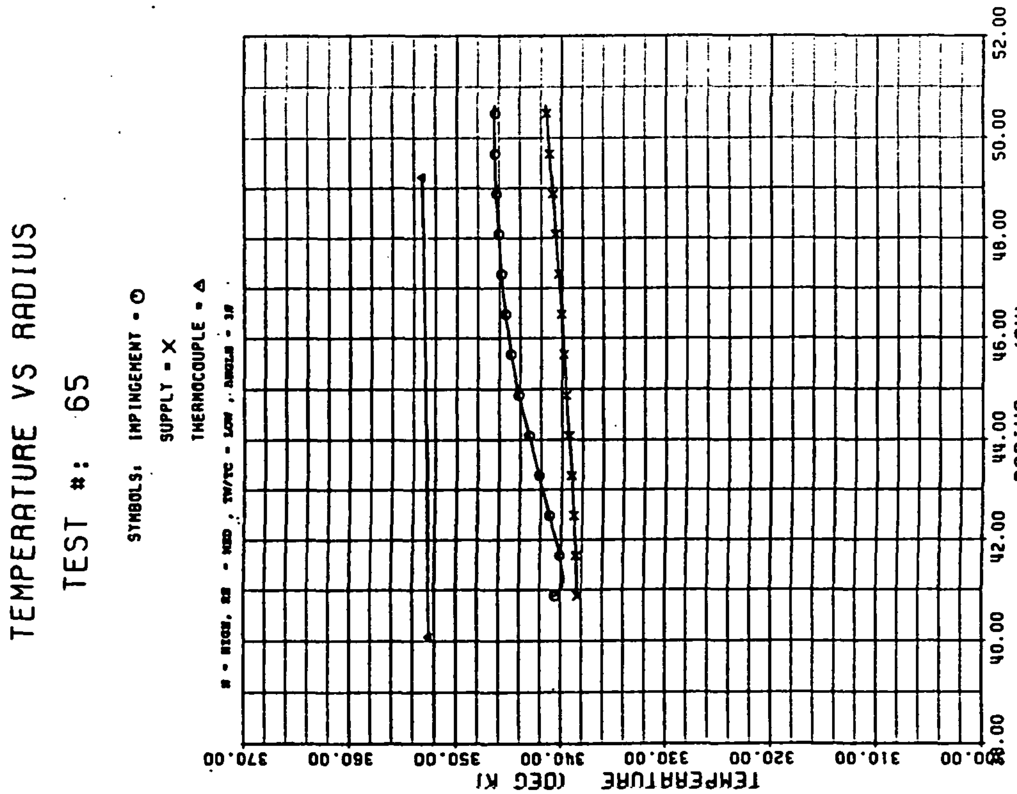

Figure 19C

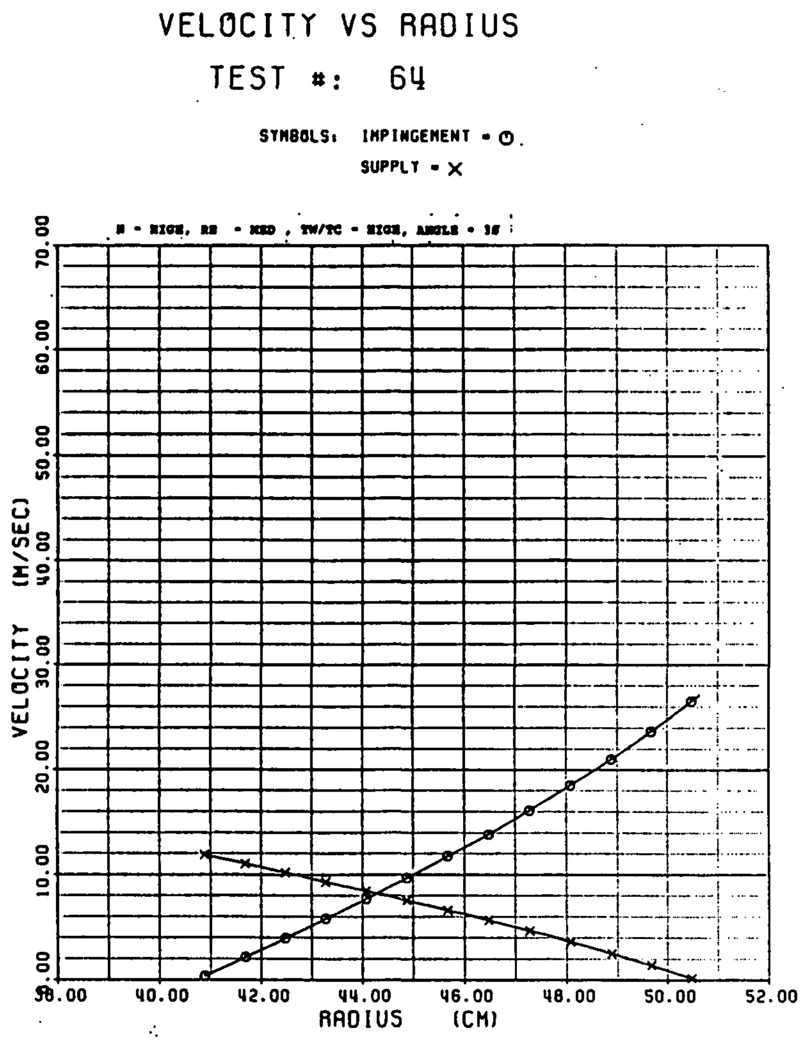

Figure 20A

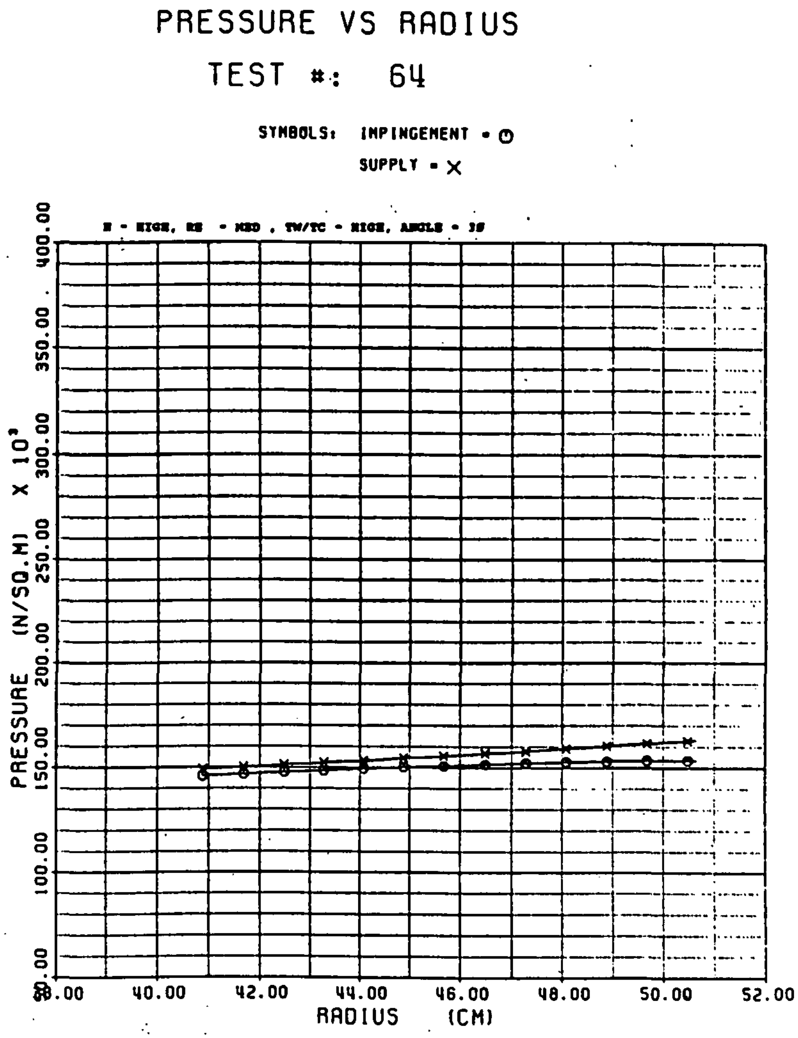

Figure 20B

ORIGINAL PAGE IS
OF POOR QUALITY

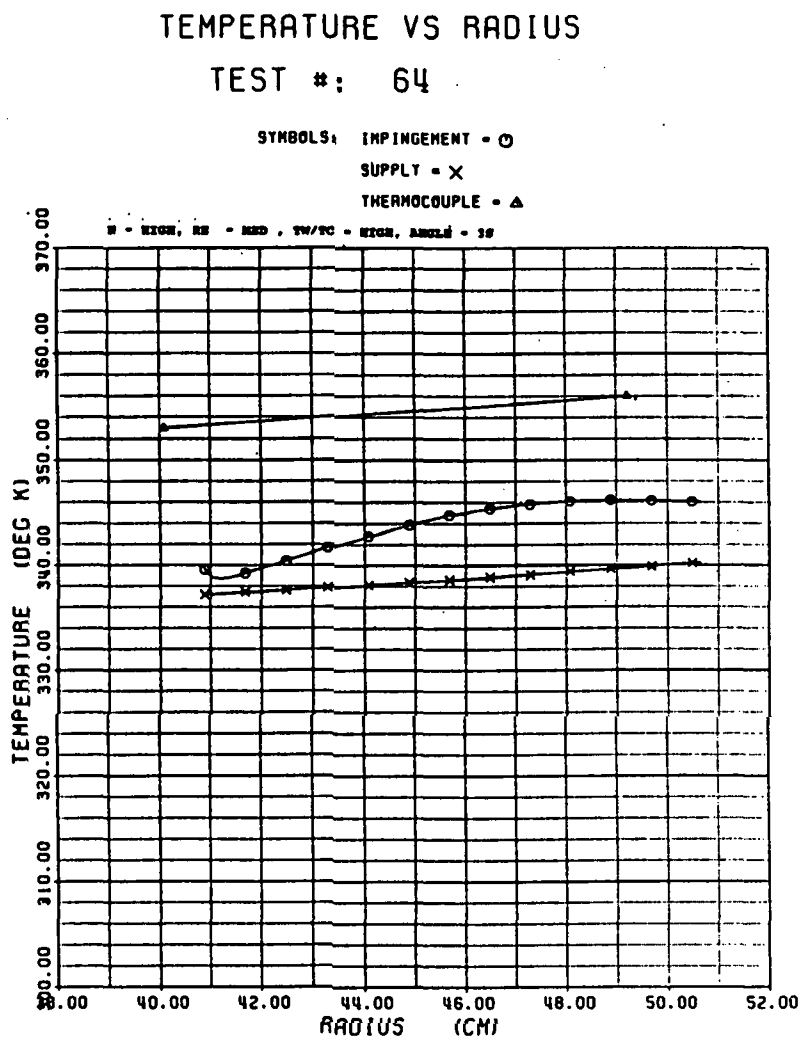

Figure 20C

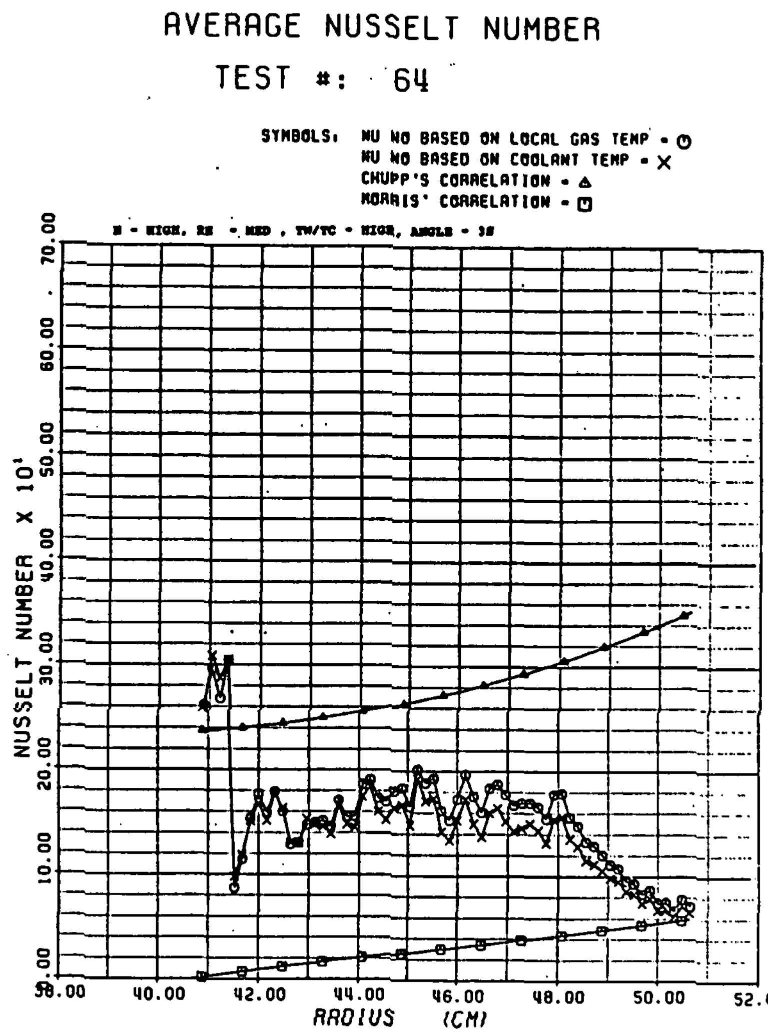

Figure 20D

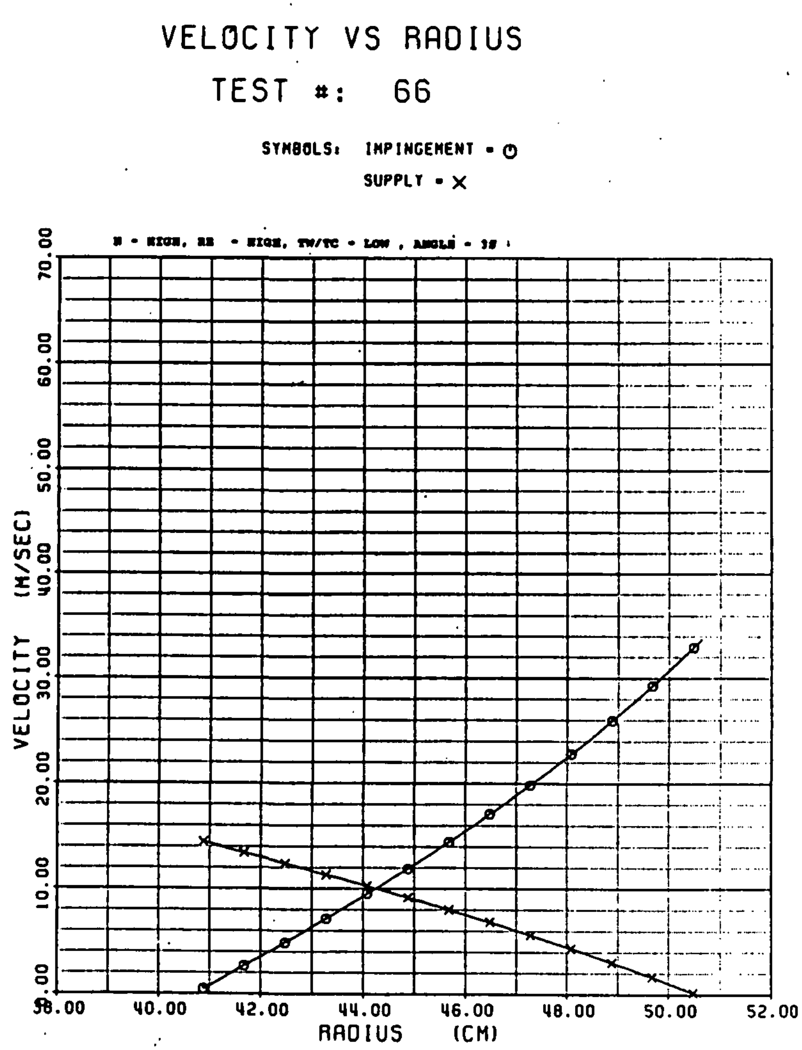

Figure 21A

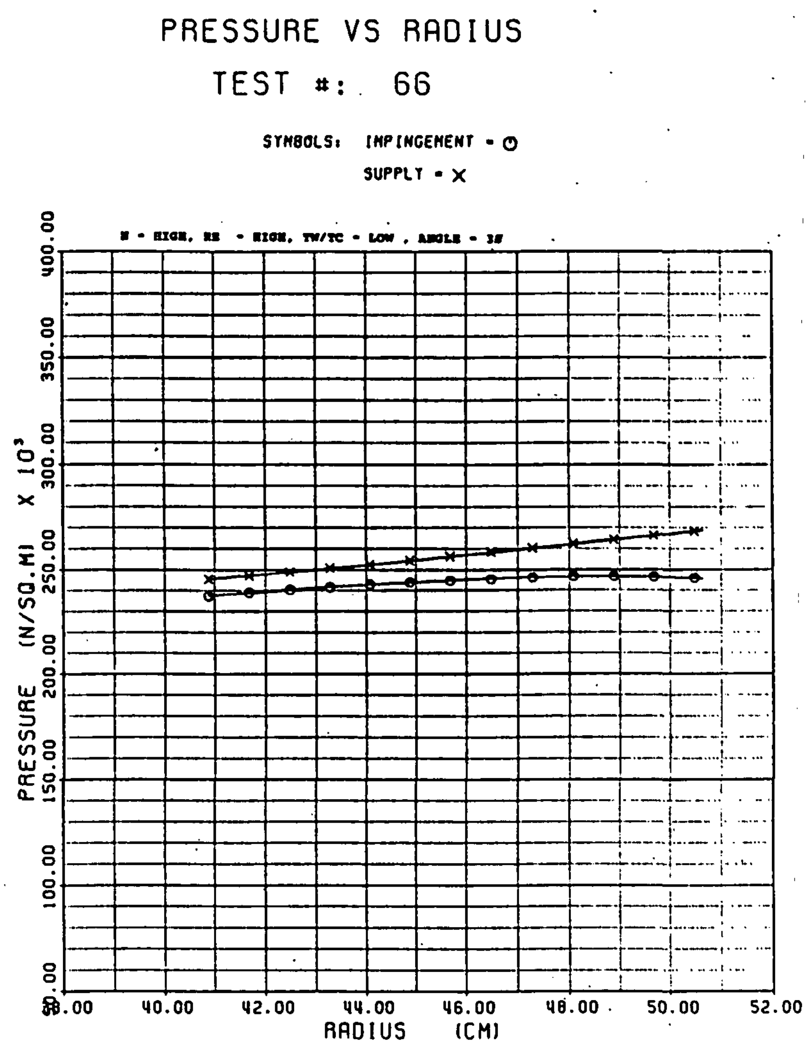

Figure 21B

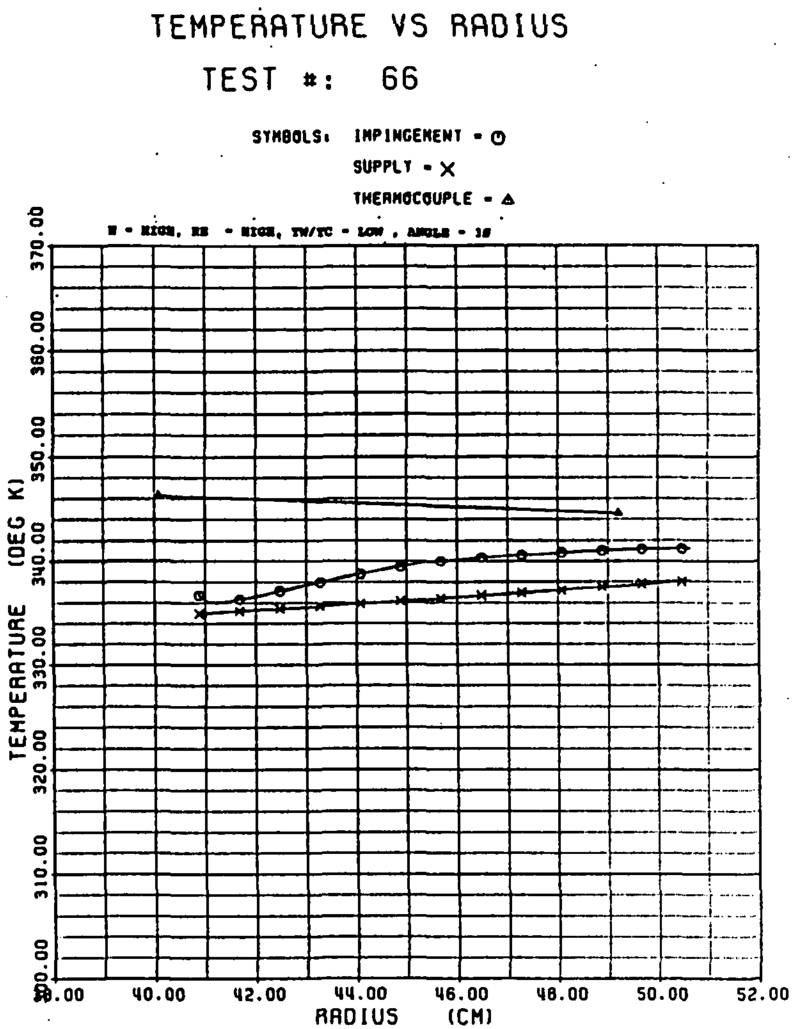

Figure 21C

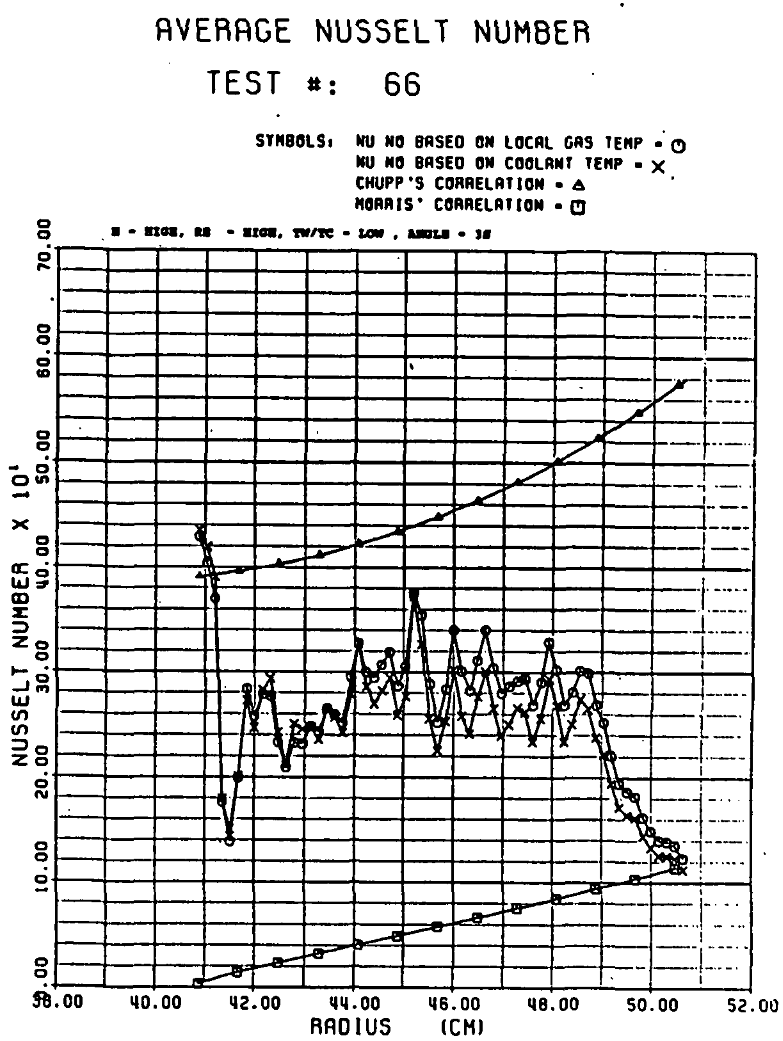

Figure 21D

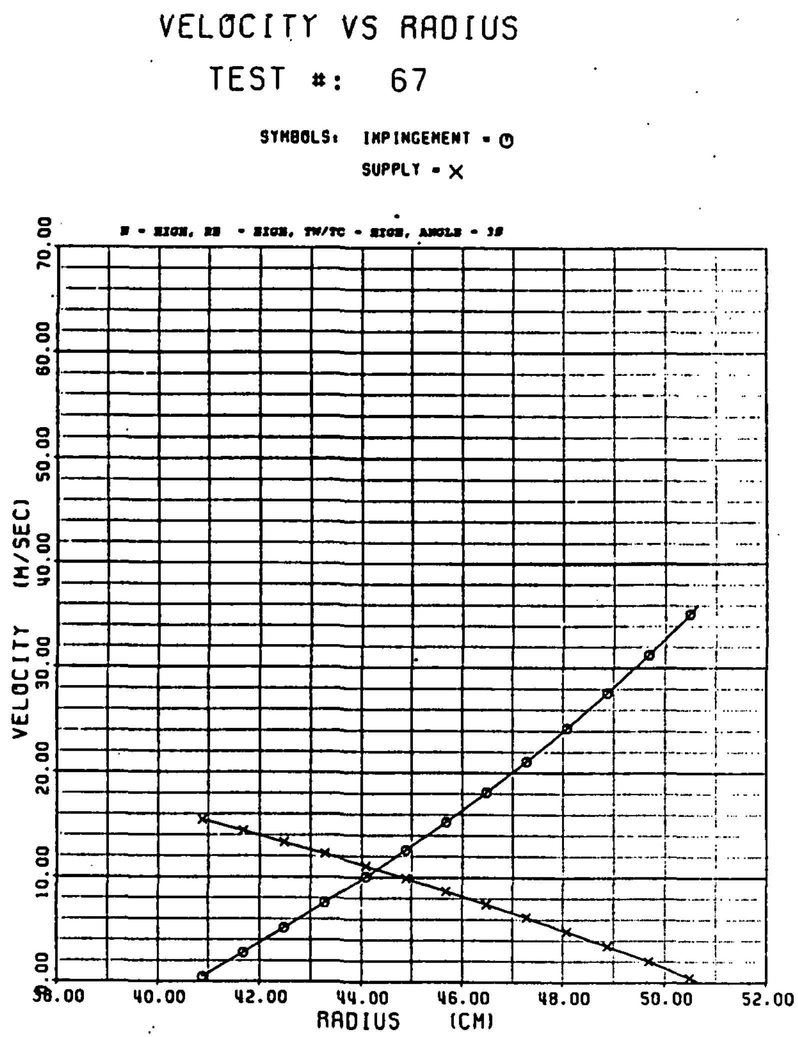

Figure 22A

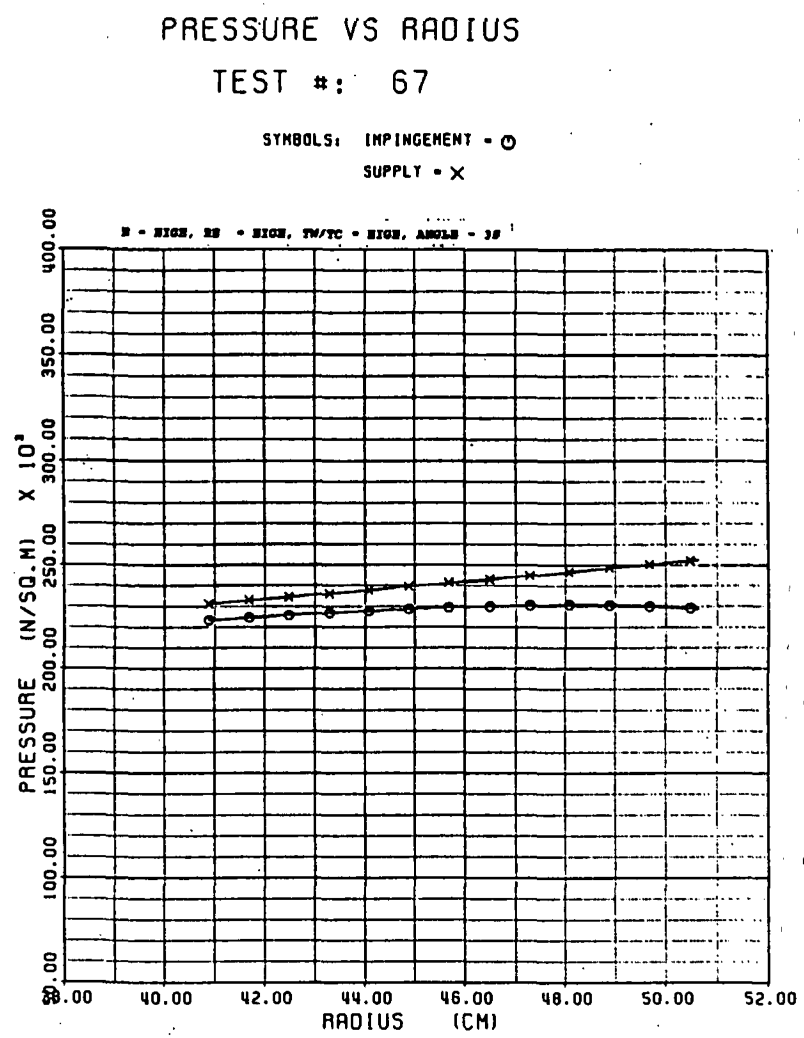

Figure 22B

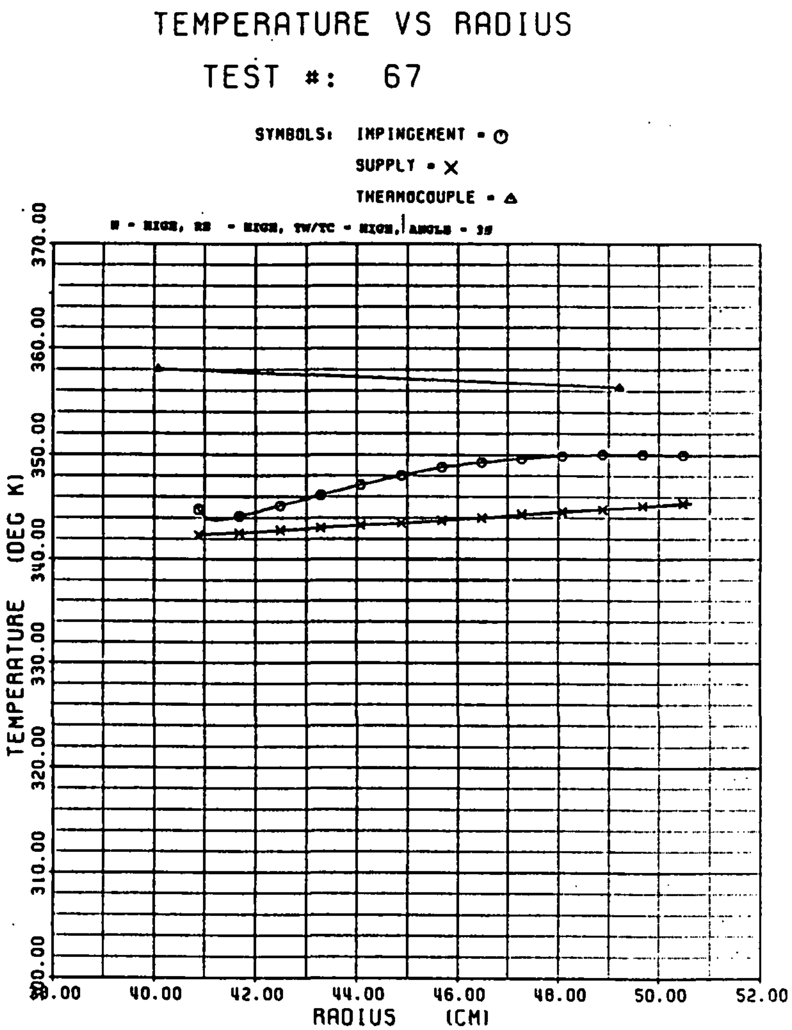

Figure 22C

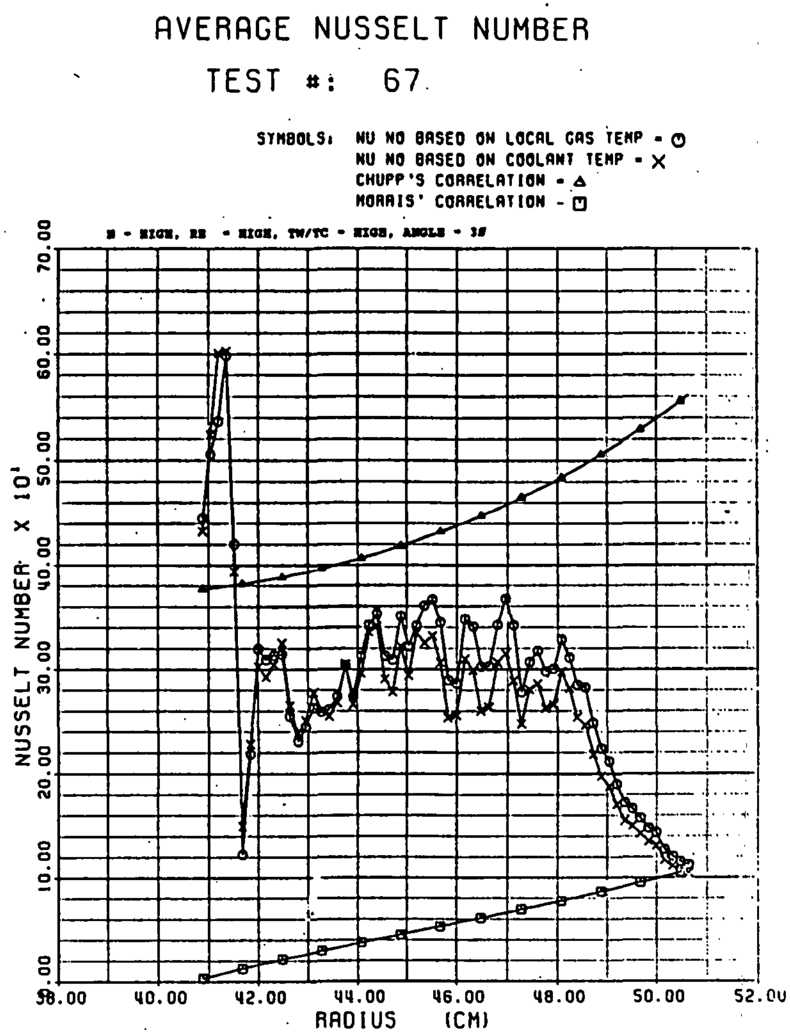

Figure 22D

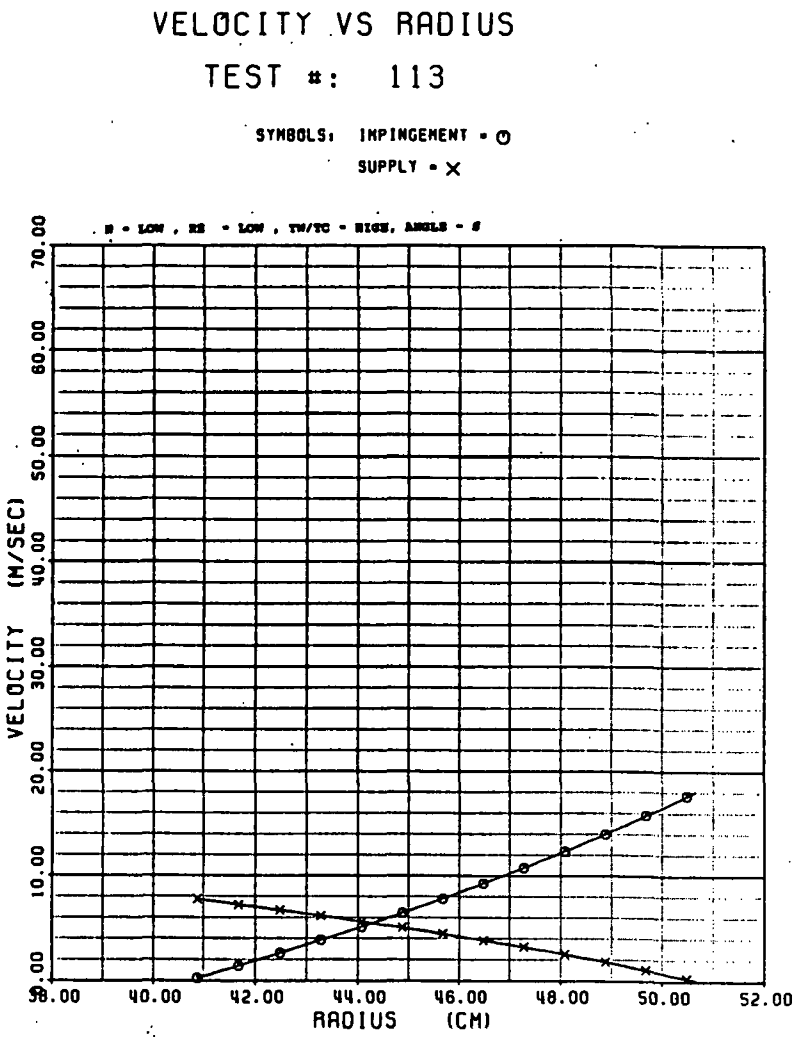

Figure 23A

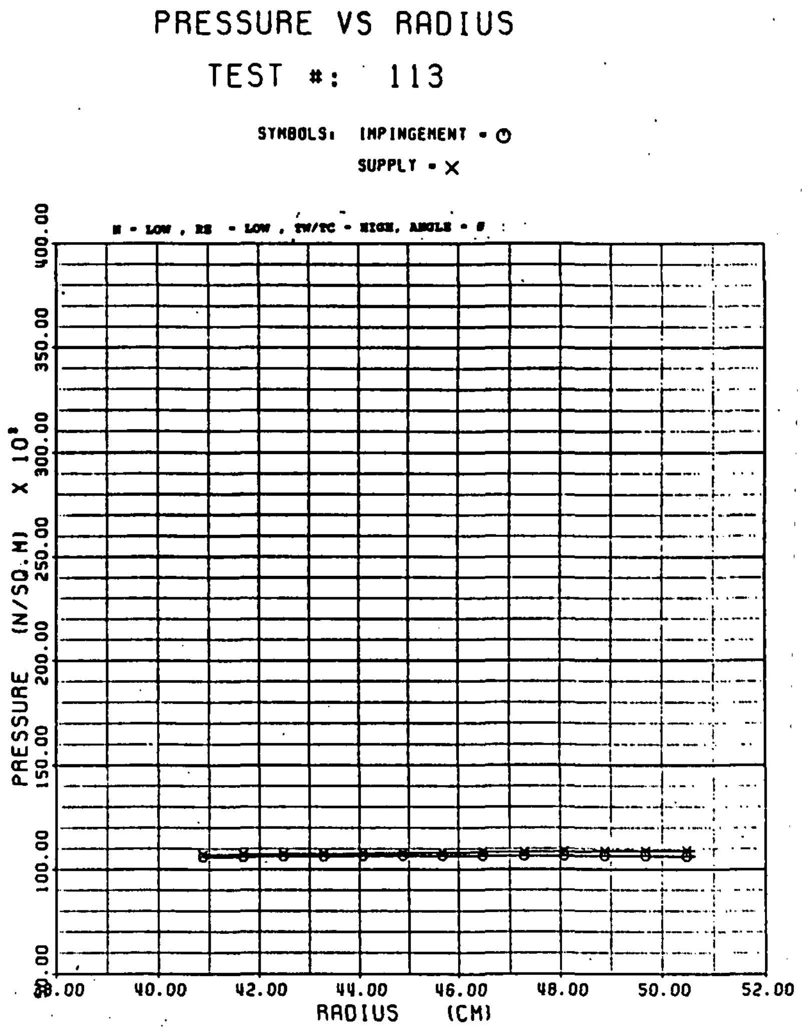

Figure 23B

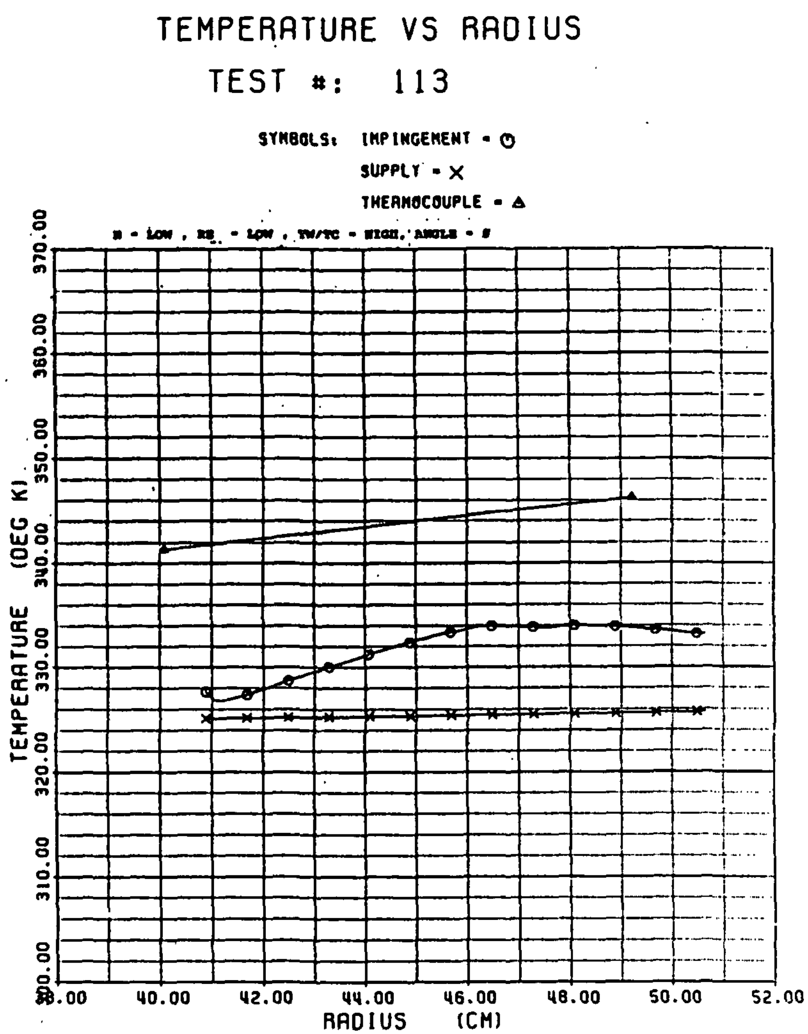

Figure 23C

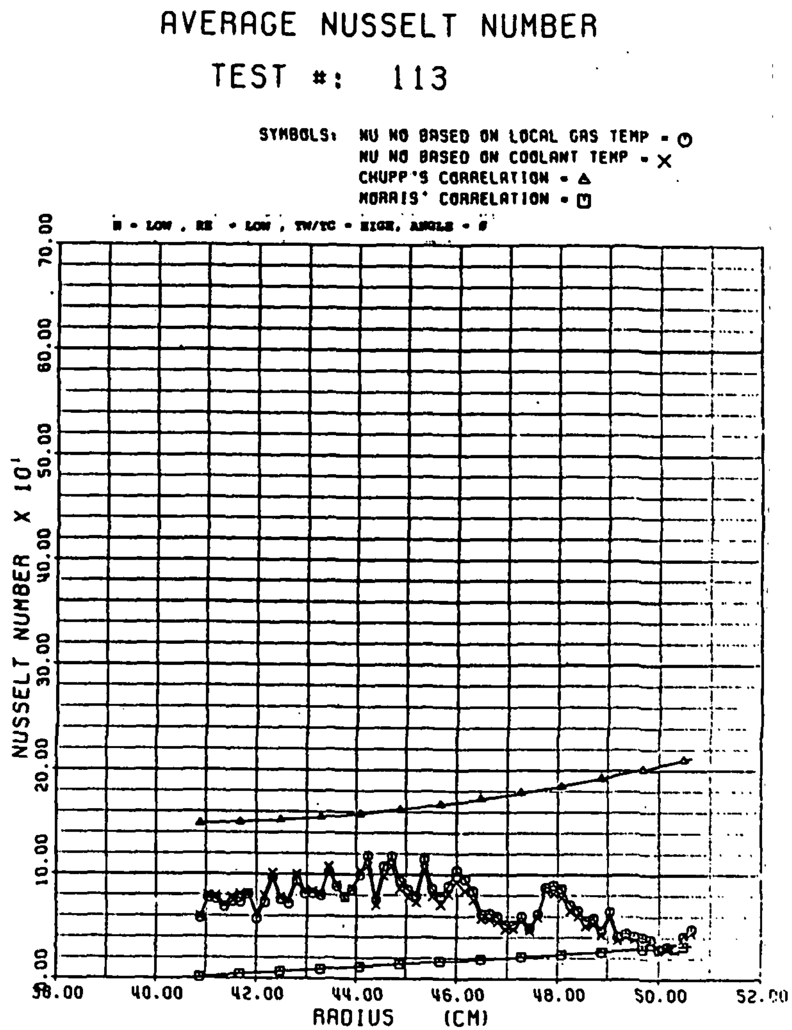

Figure 23D

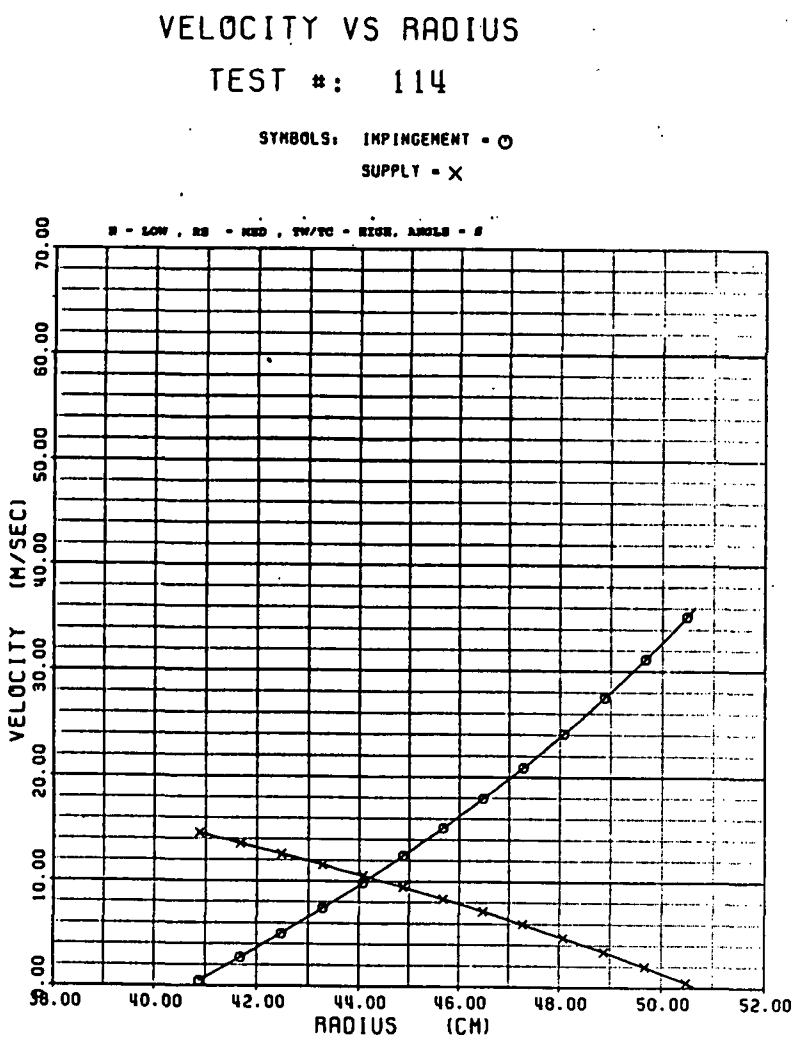

Figure 24A

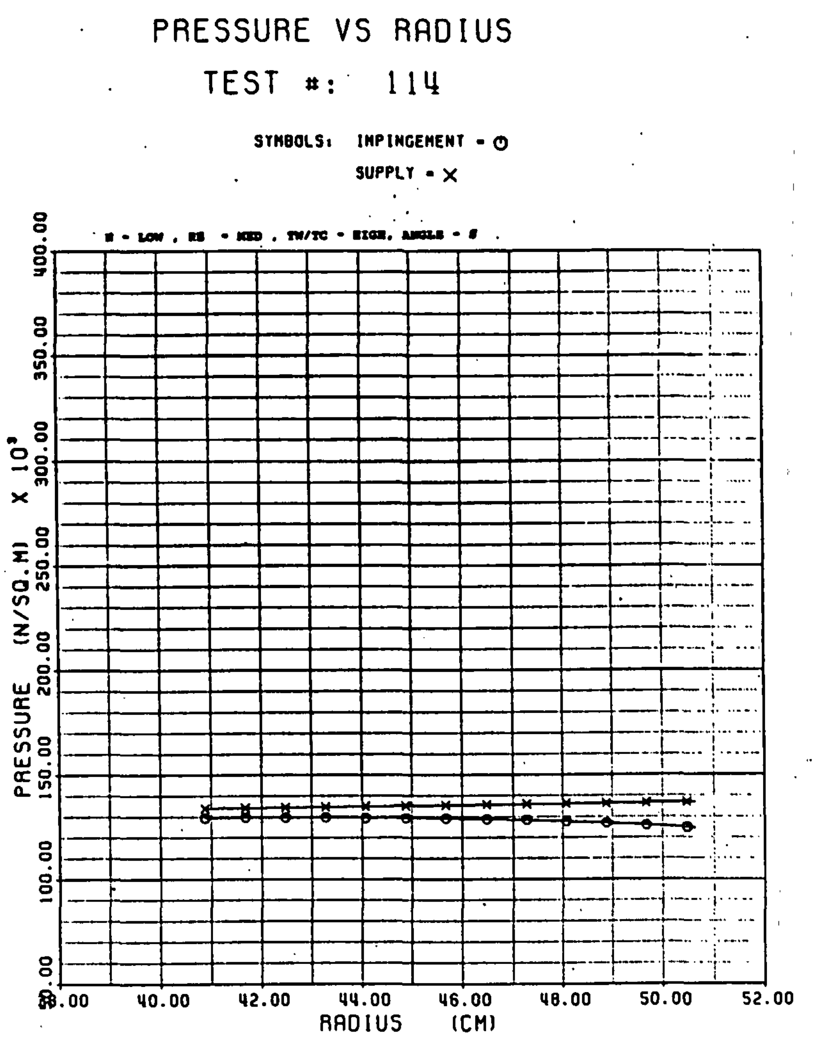

Figure 24B

ORIGINAL PAGE IS OF POOR QUALITY

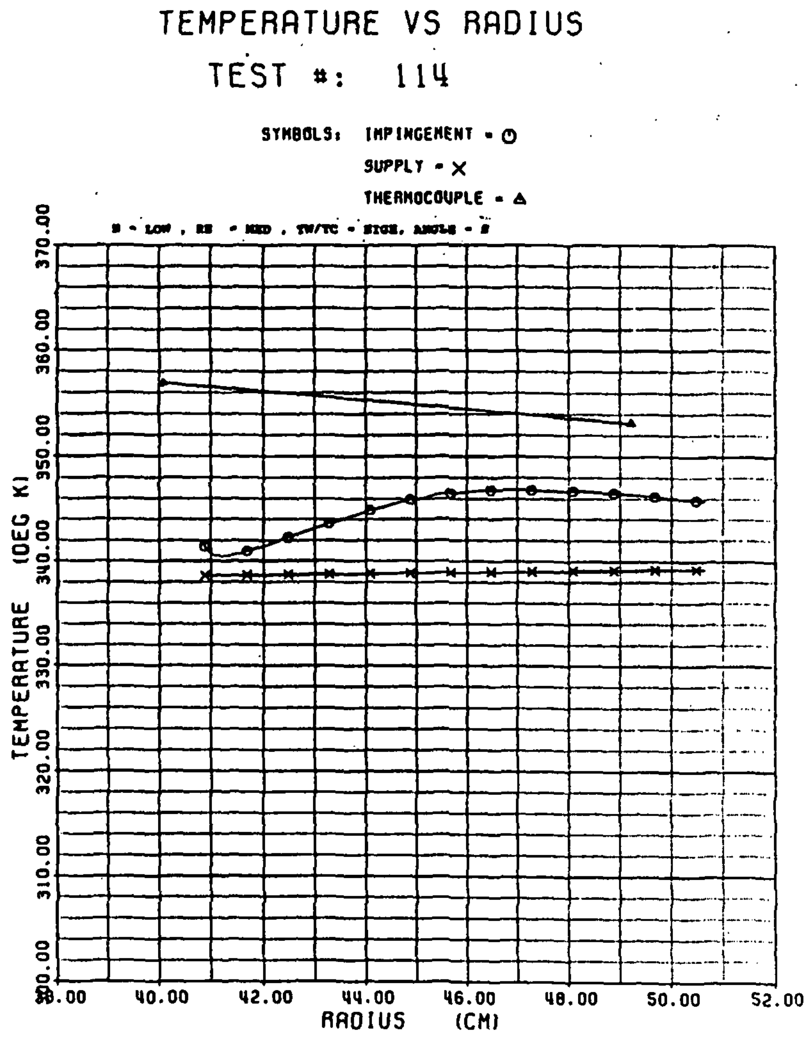

Figure 24C

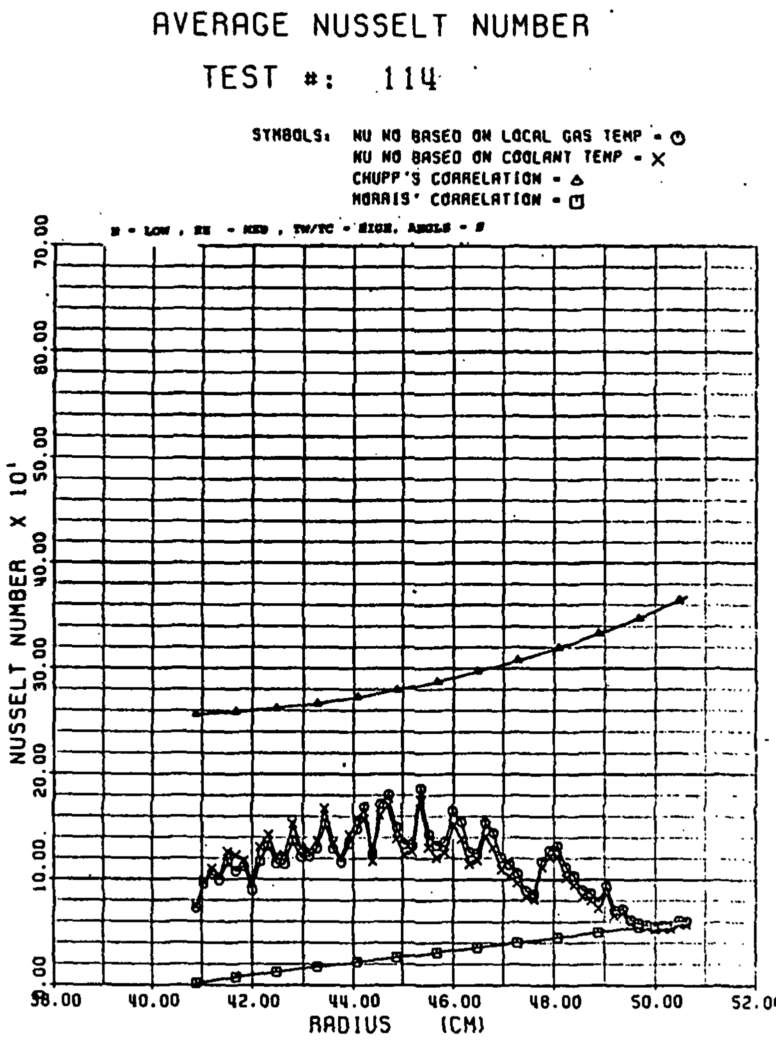

Figure 24D

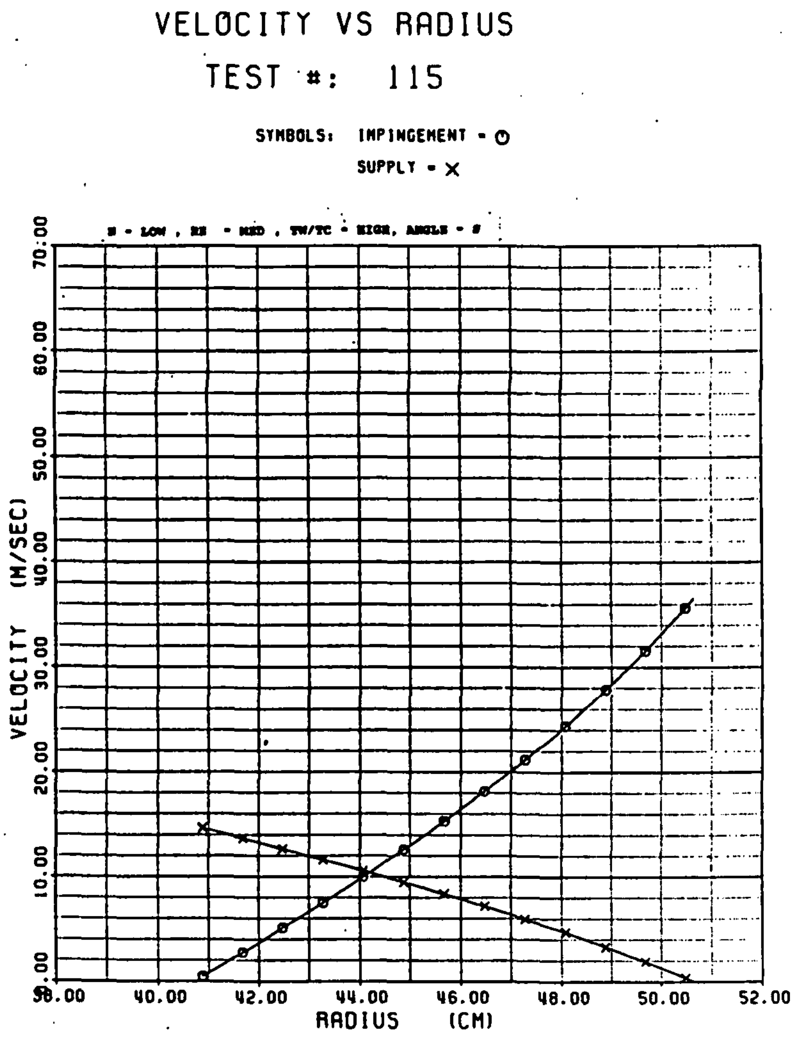

Figure 25A

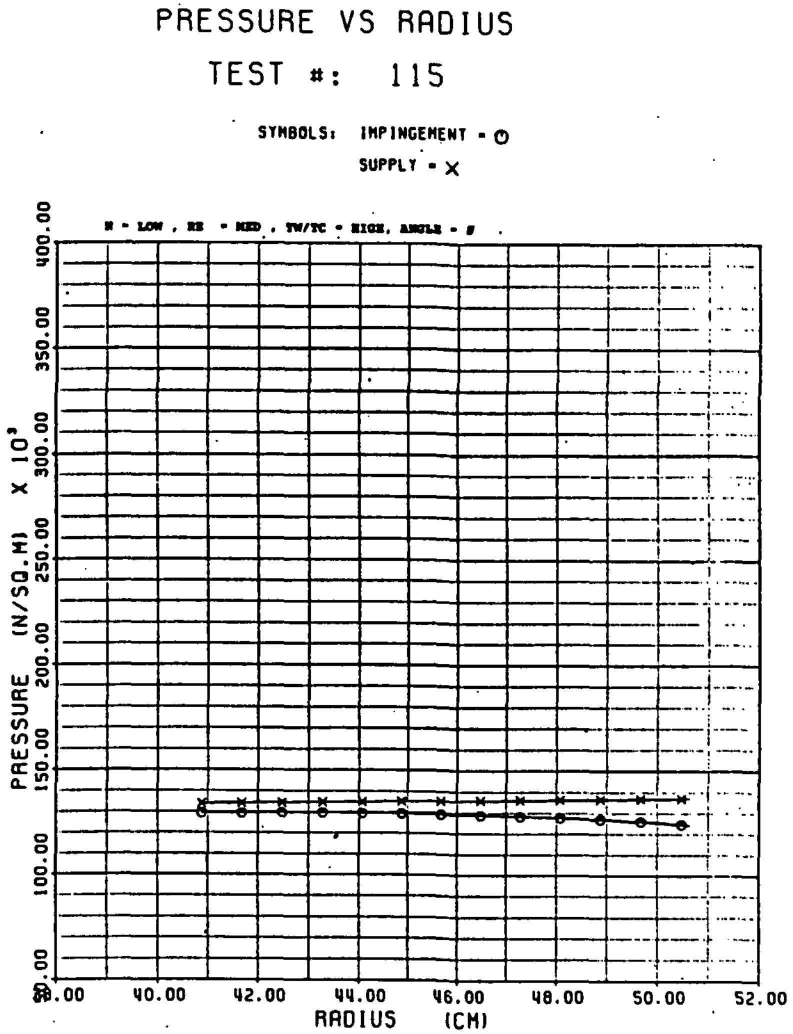

Figure 25B

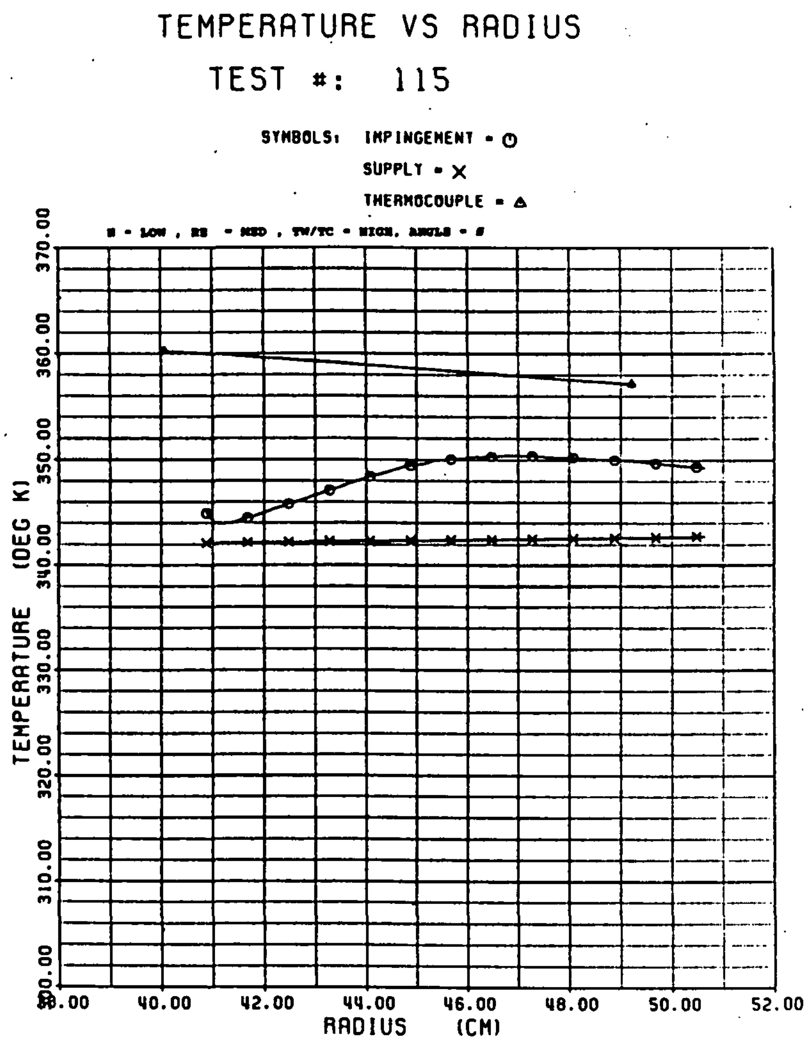

Figure 25C

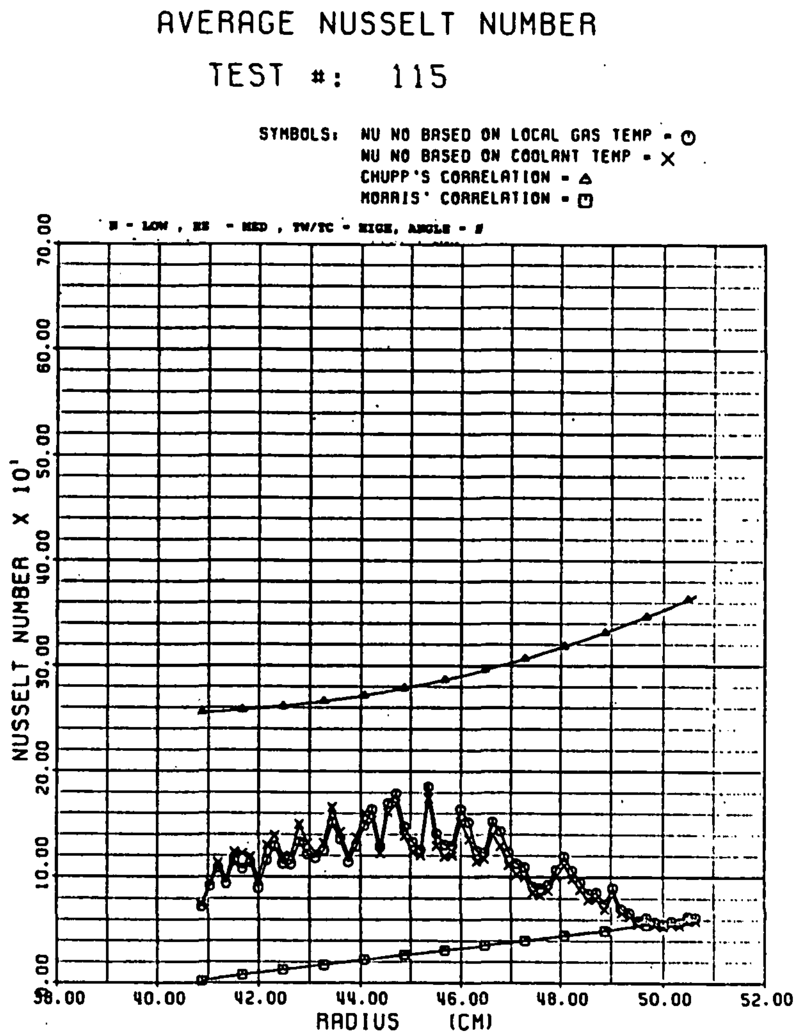

Figure 25D

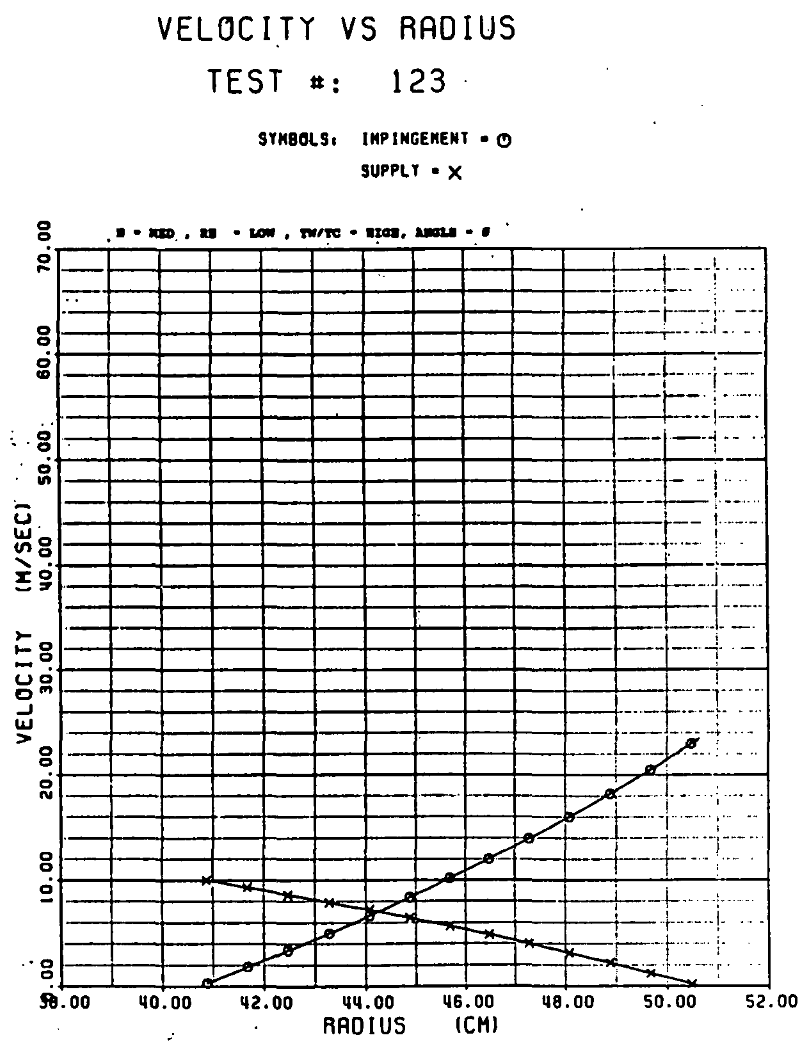

Figure 26A

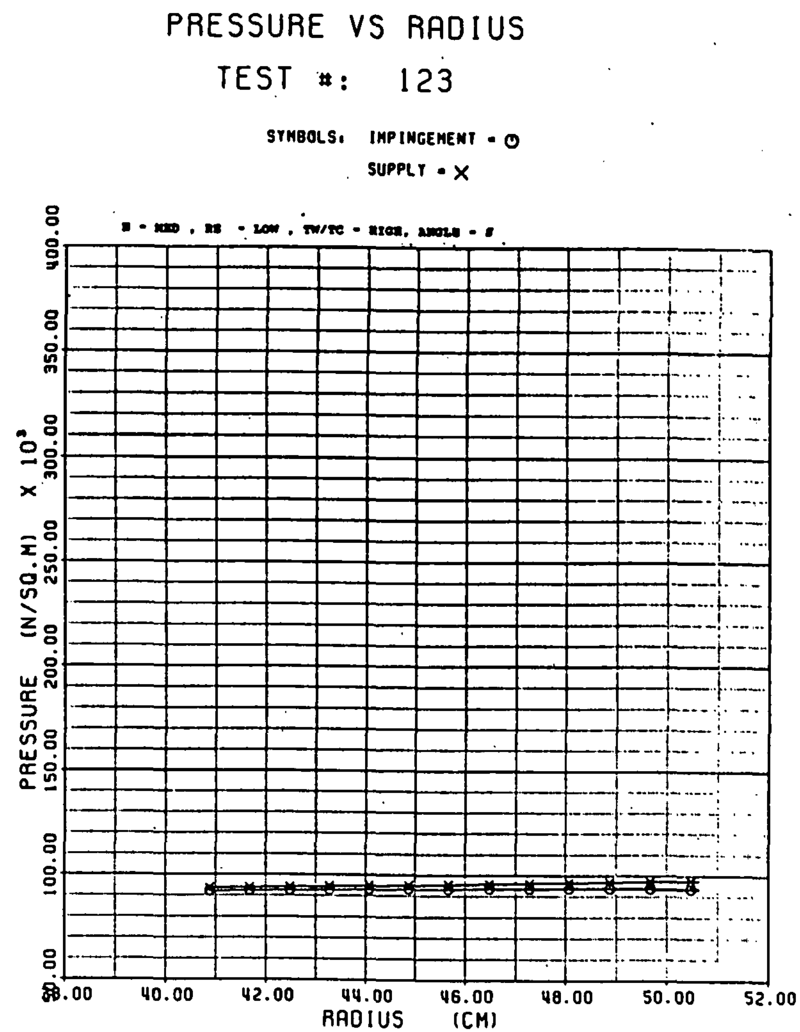

Figure 26B

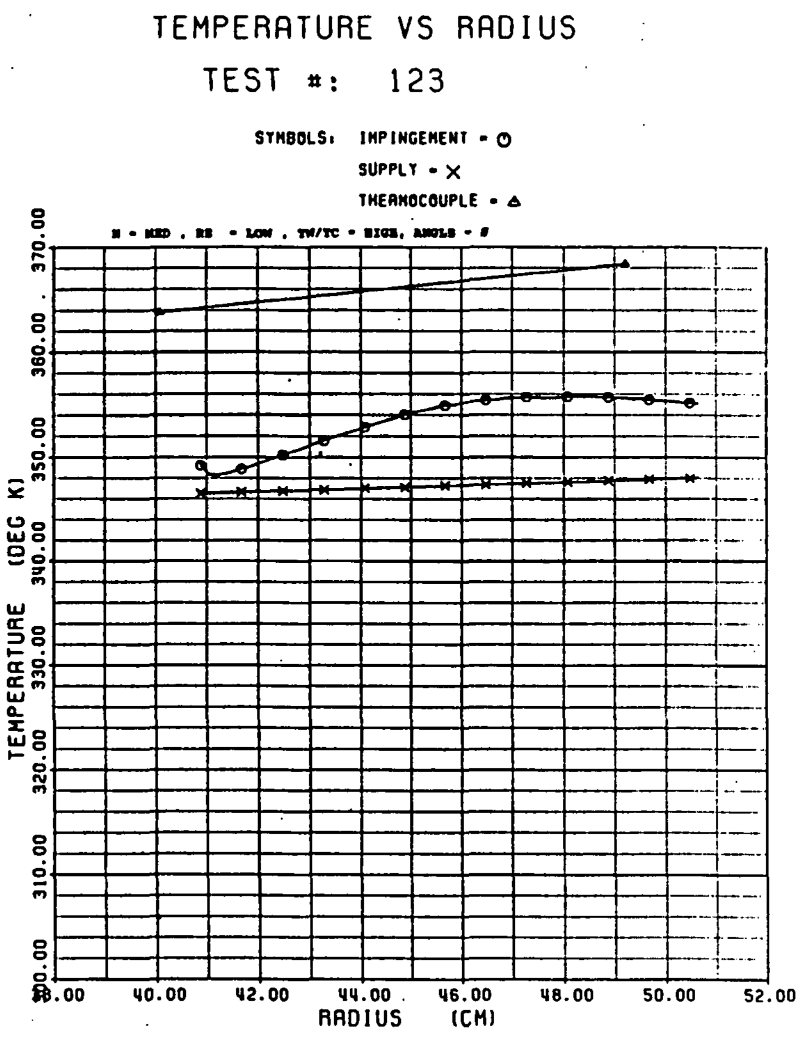

Figure 26C

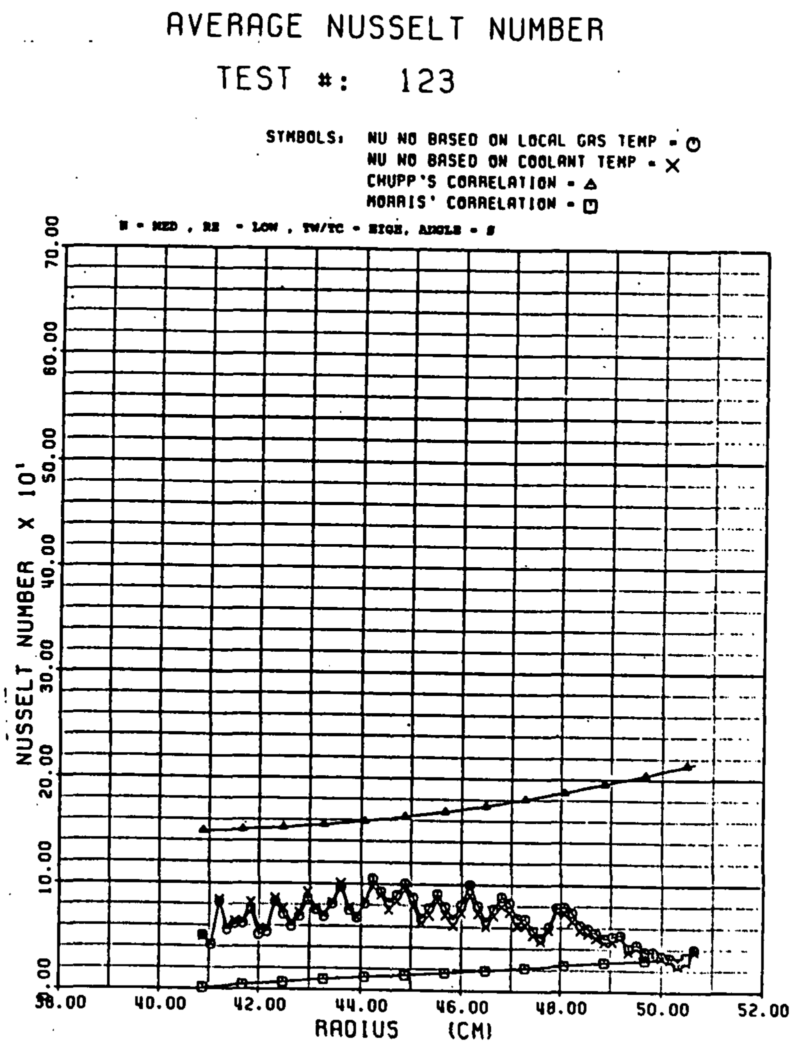

Figure 26D

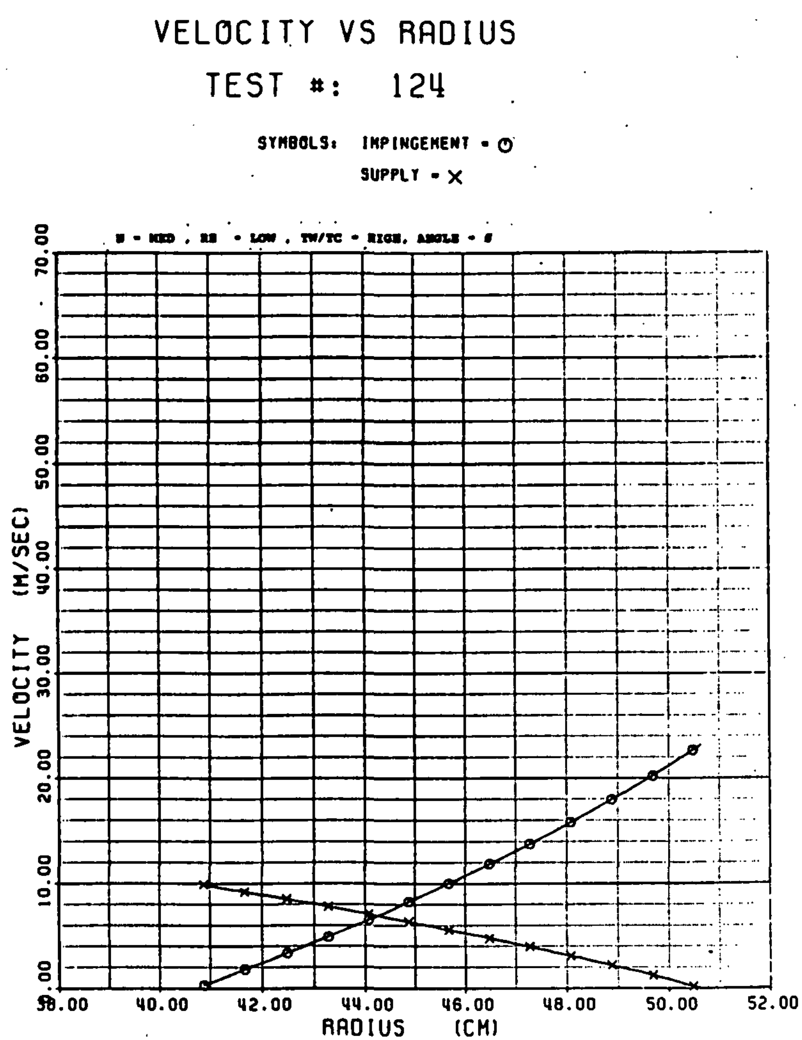

Figure 27A

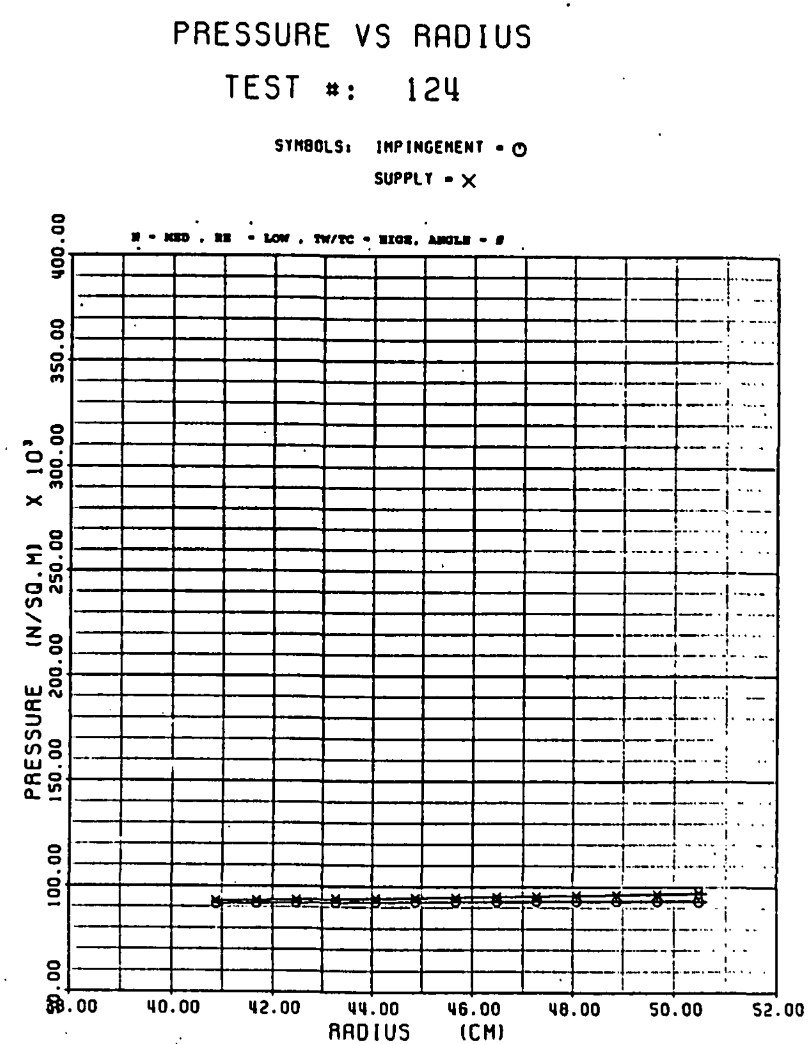

Figure 27B

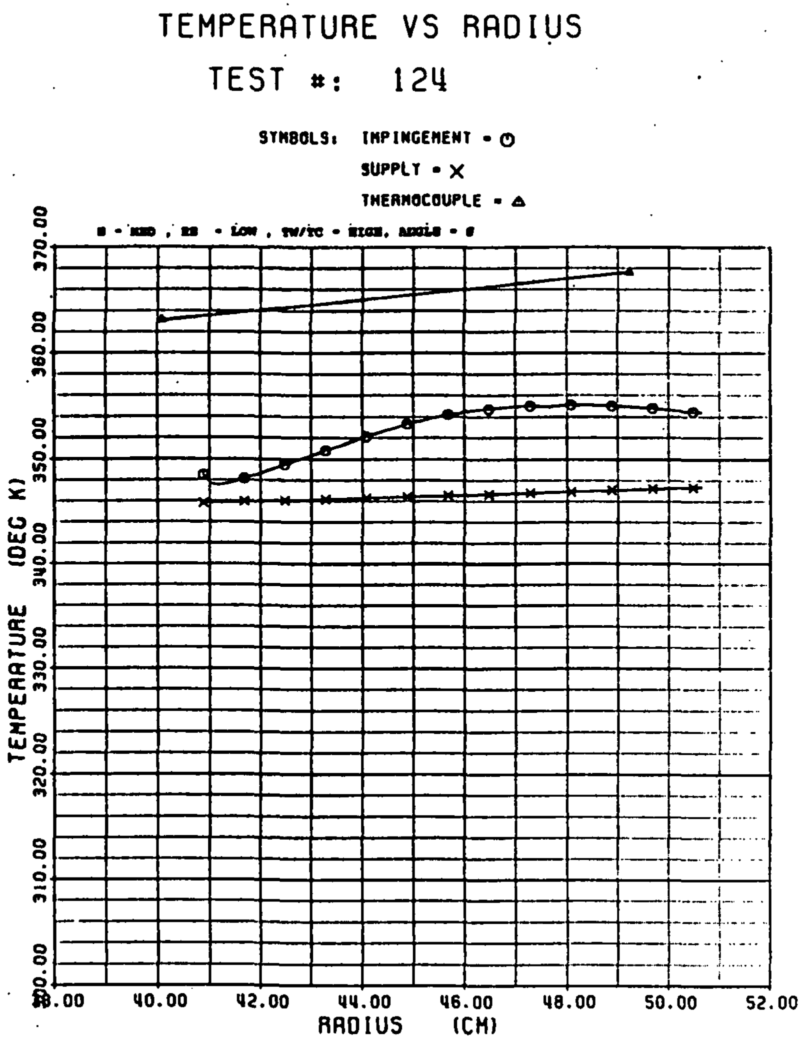

Figure 27C

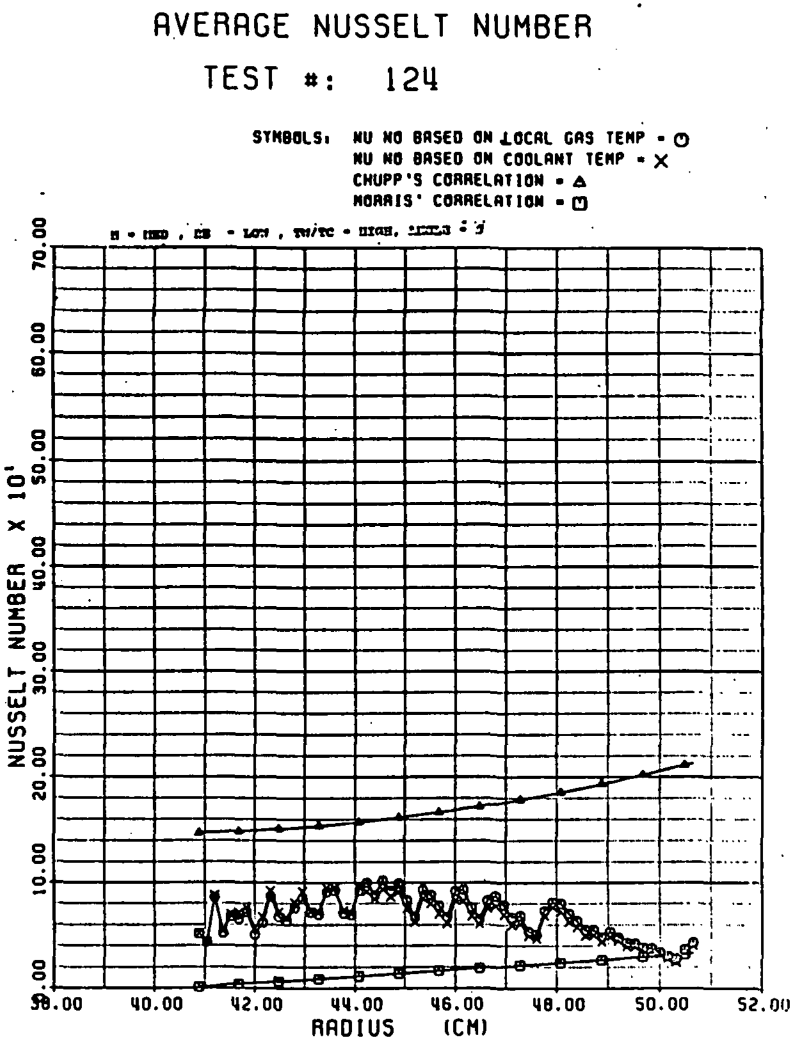

Figure 27D

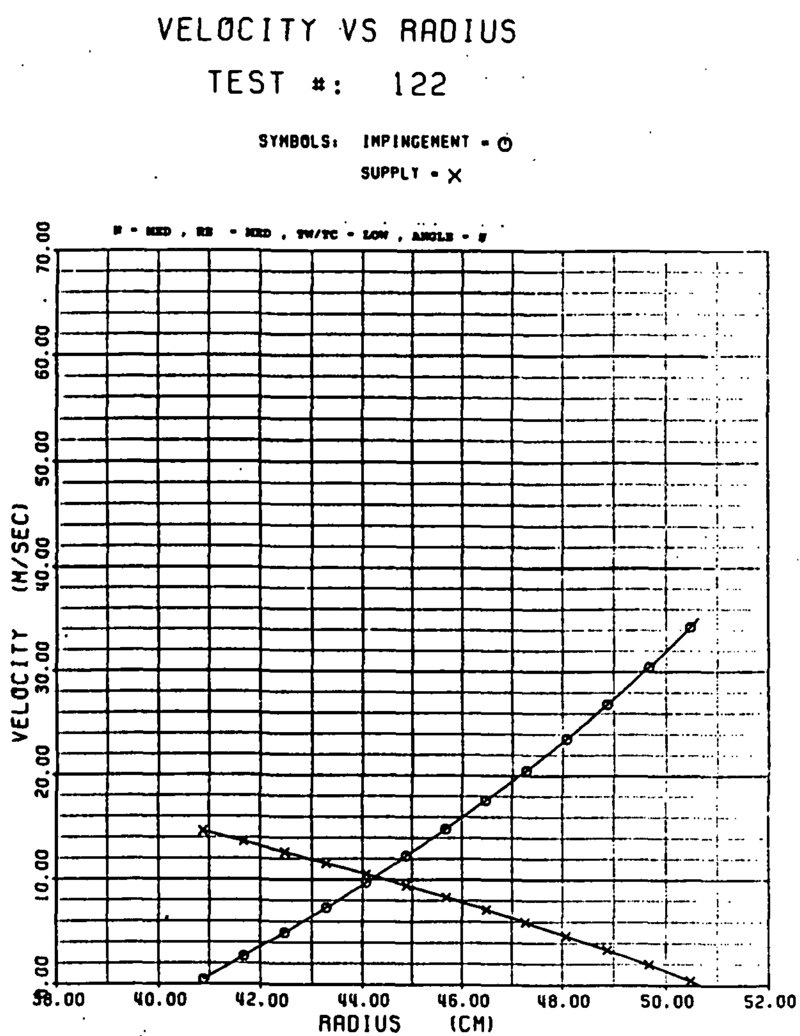

Figure 28A

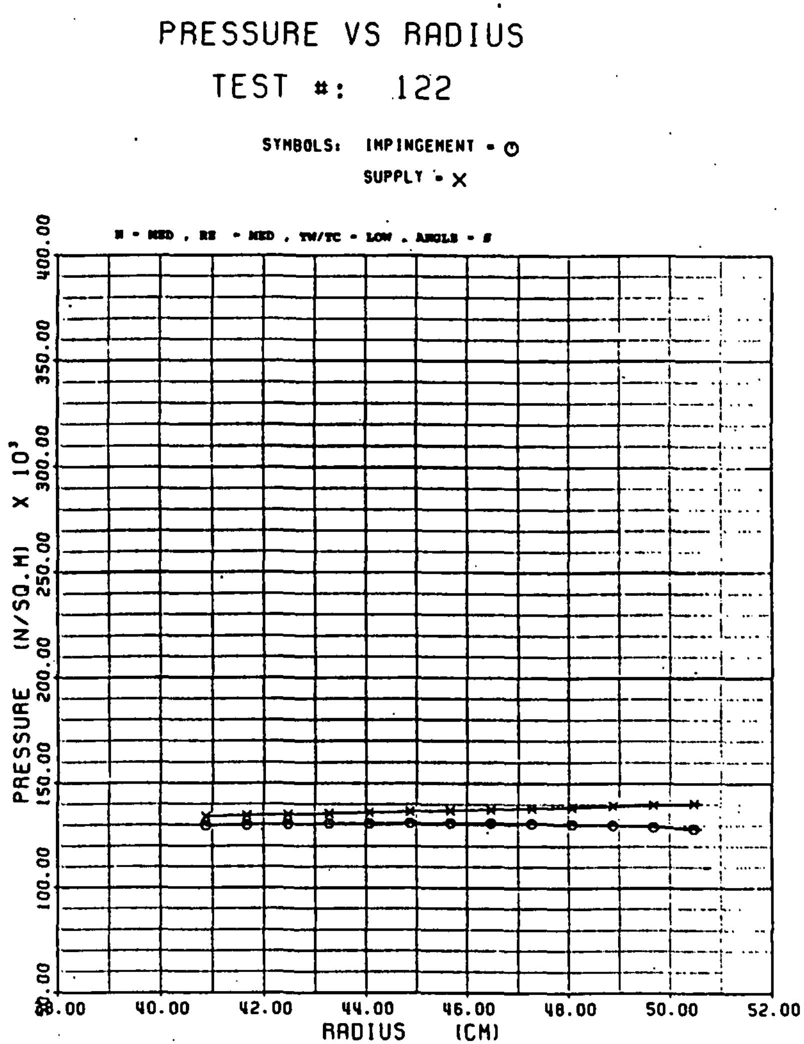

Figure 28B

ORIGINAL PAGE IS
OF POOR QUALITY

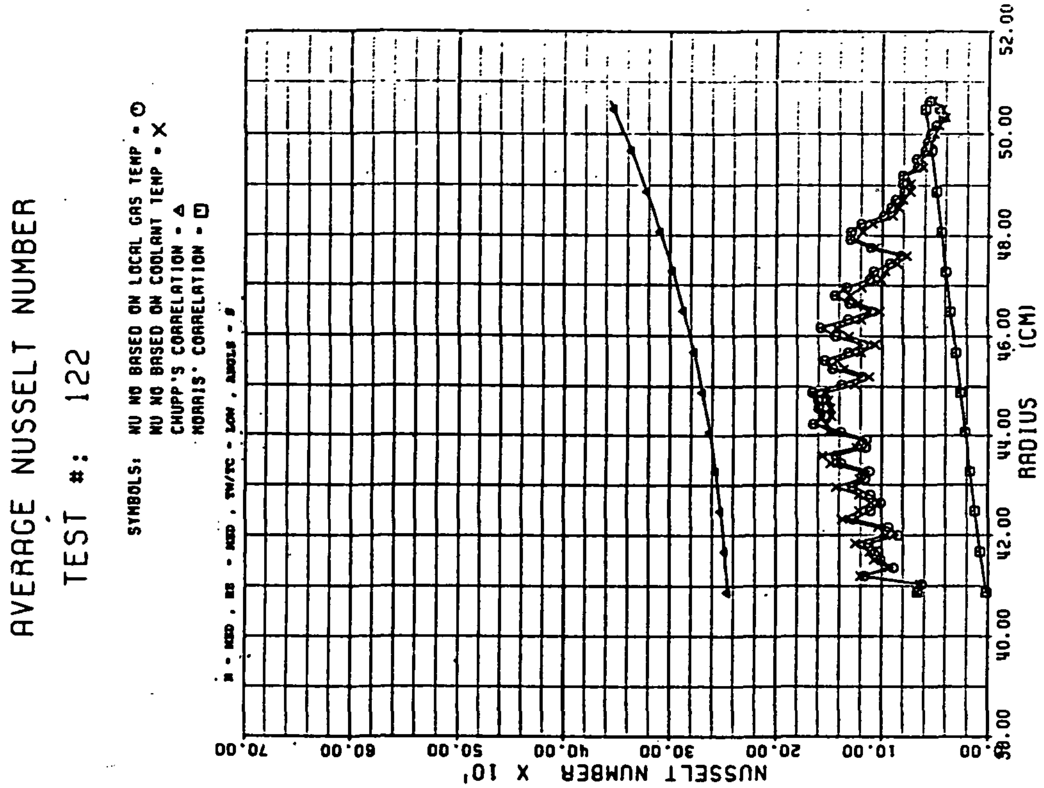

Figure 28D

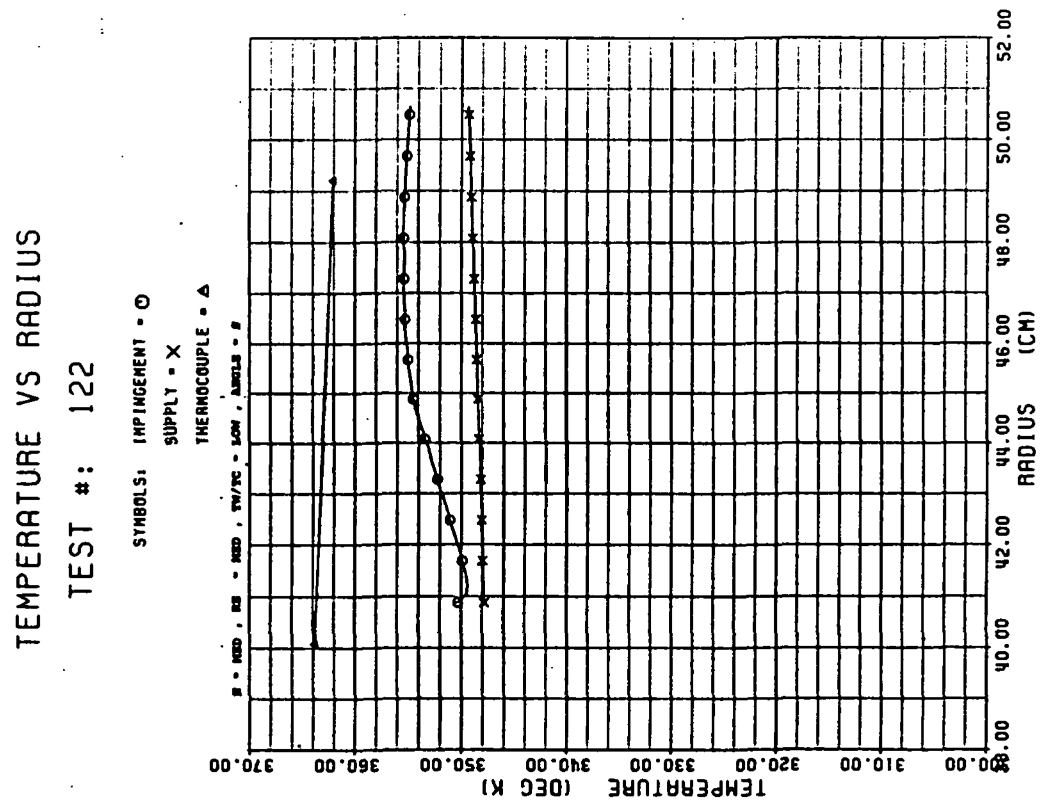

Figure 28C

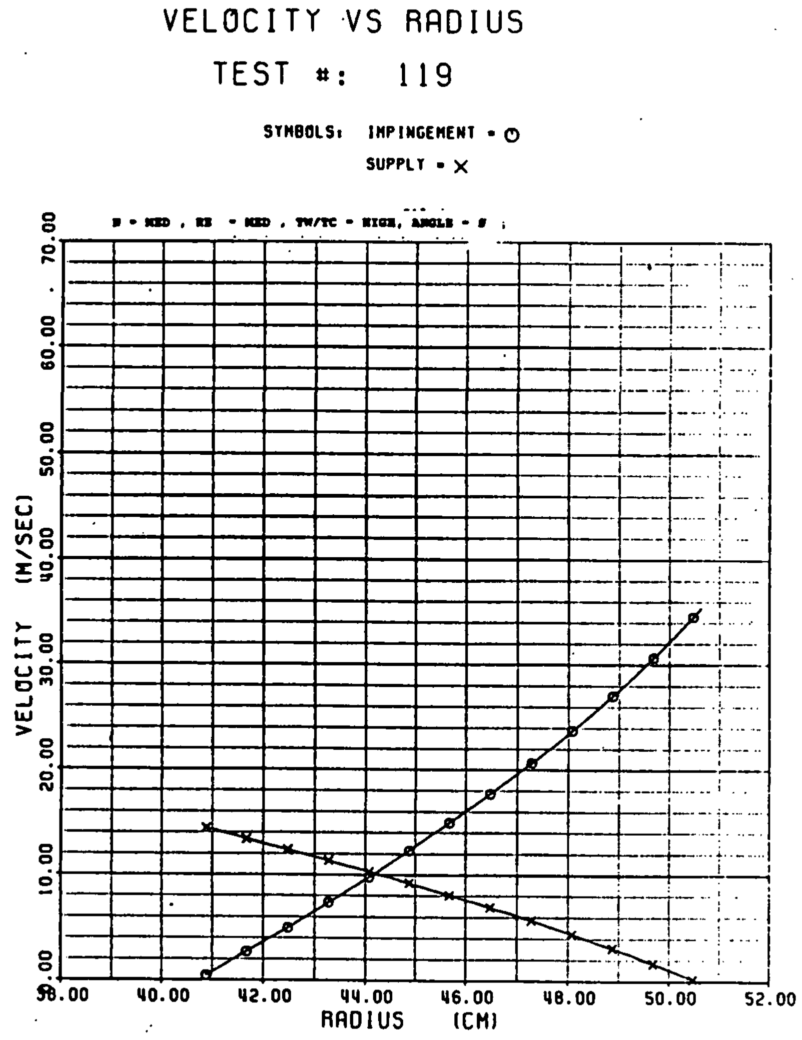

Figure 29A

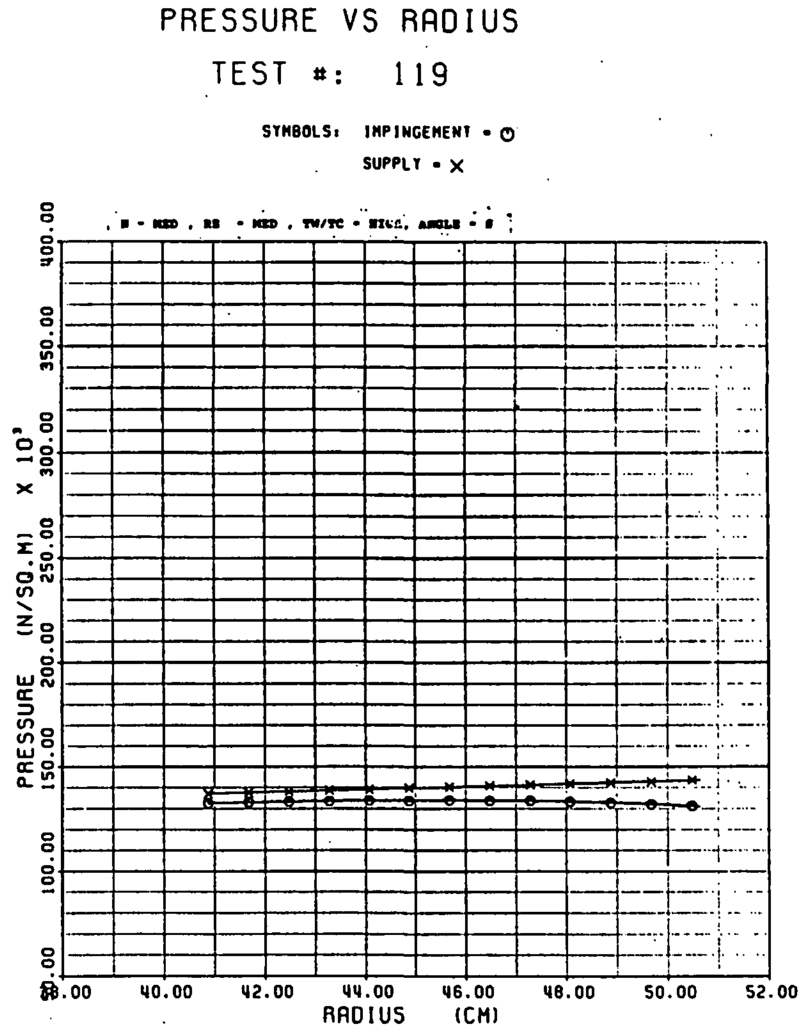

Figure 29B

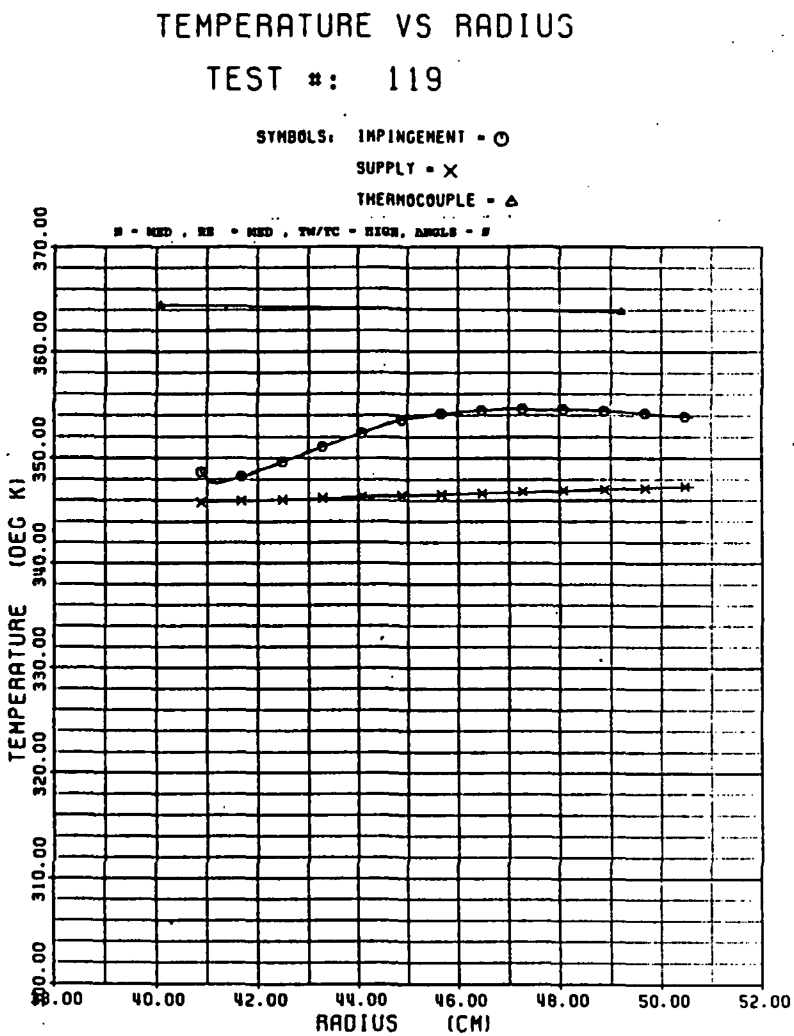

Figure 29C

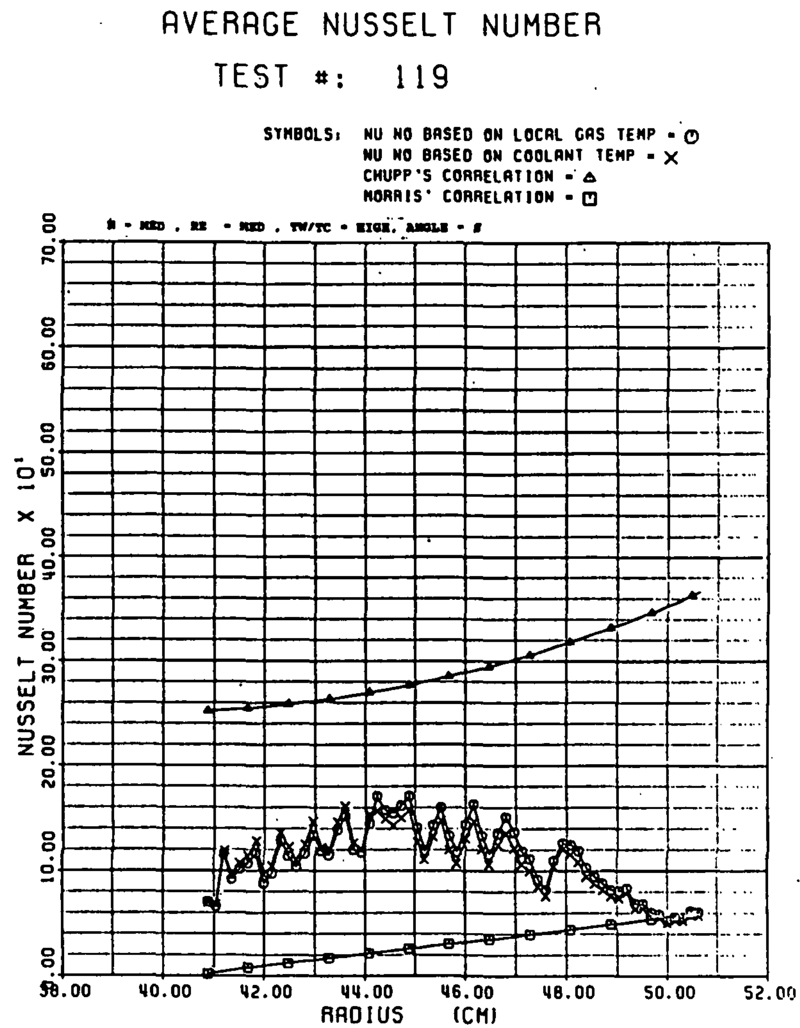

Figure 29D

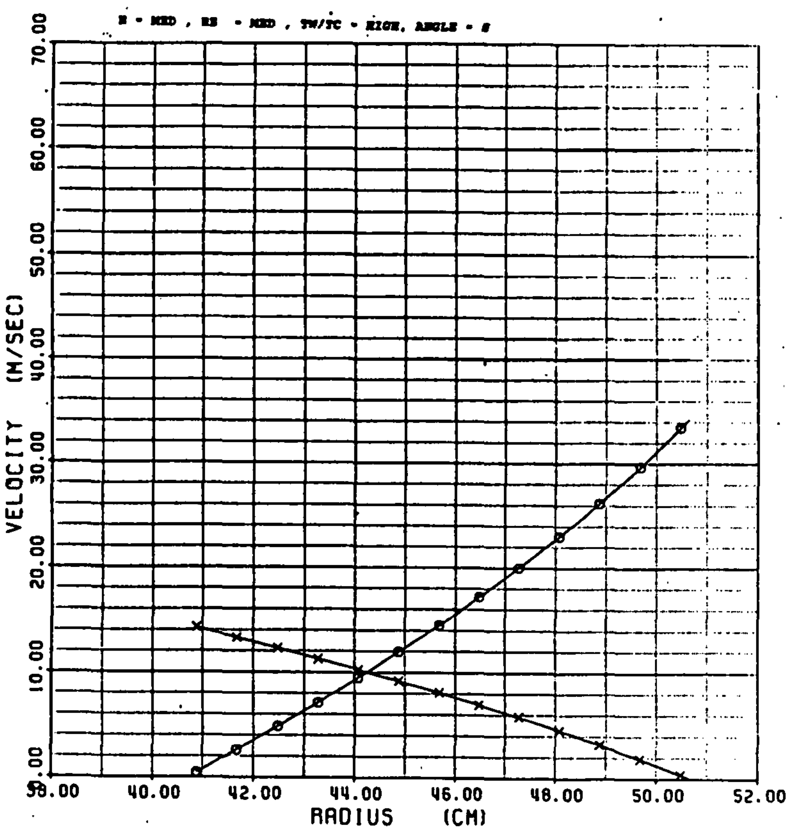

Figure 30A

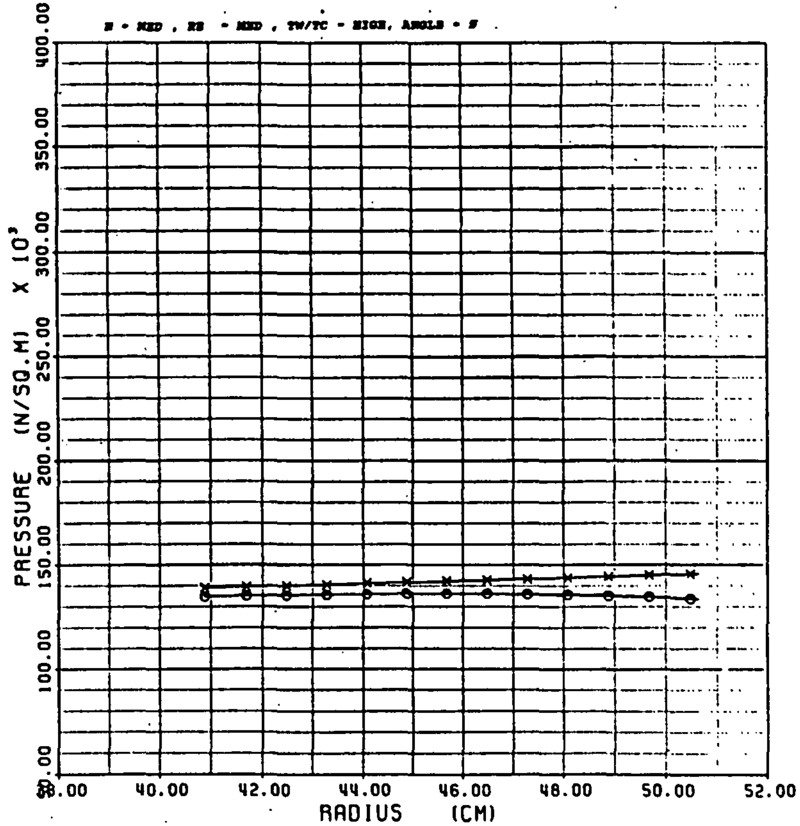

Figure 30B

ORIGINAL PAGE IS
OF POOR QUALITY

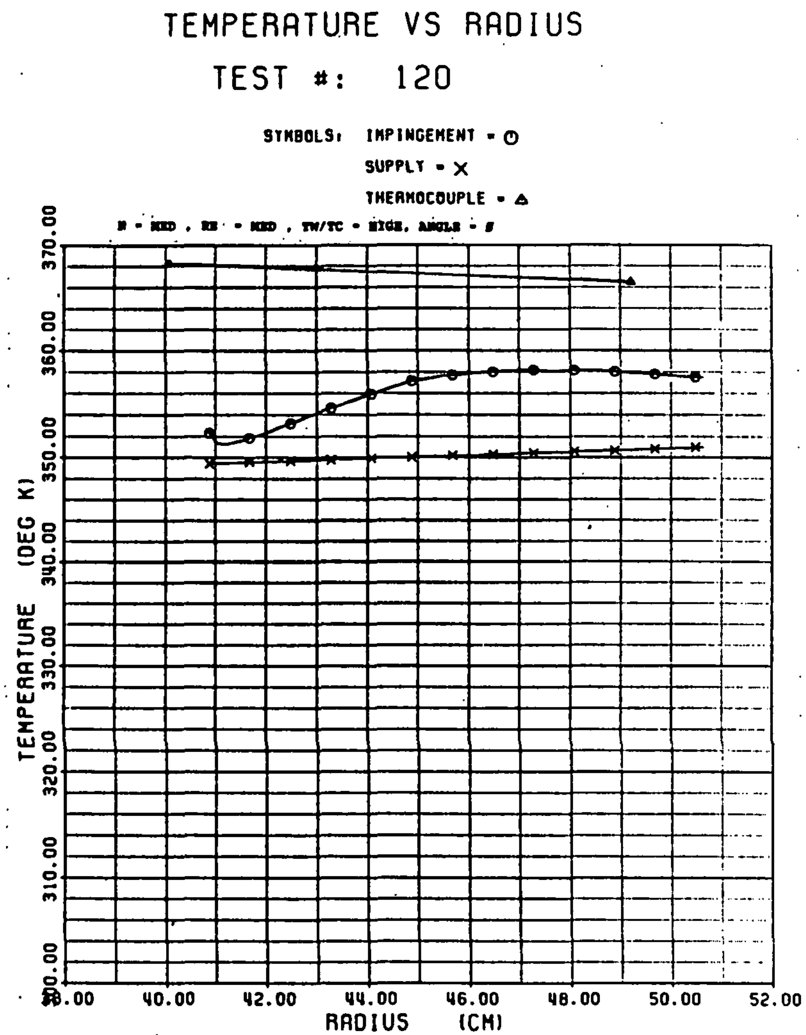

Figure 30C

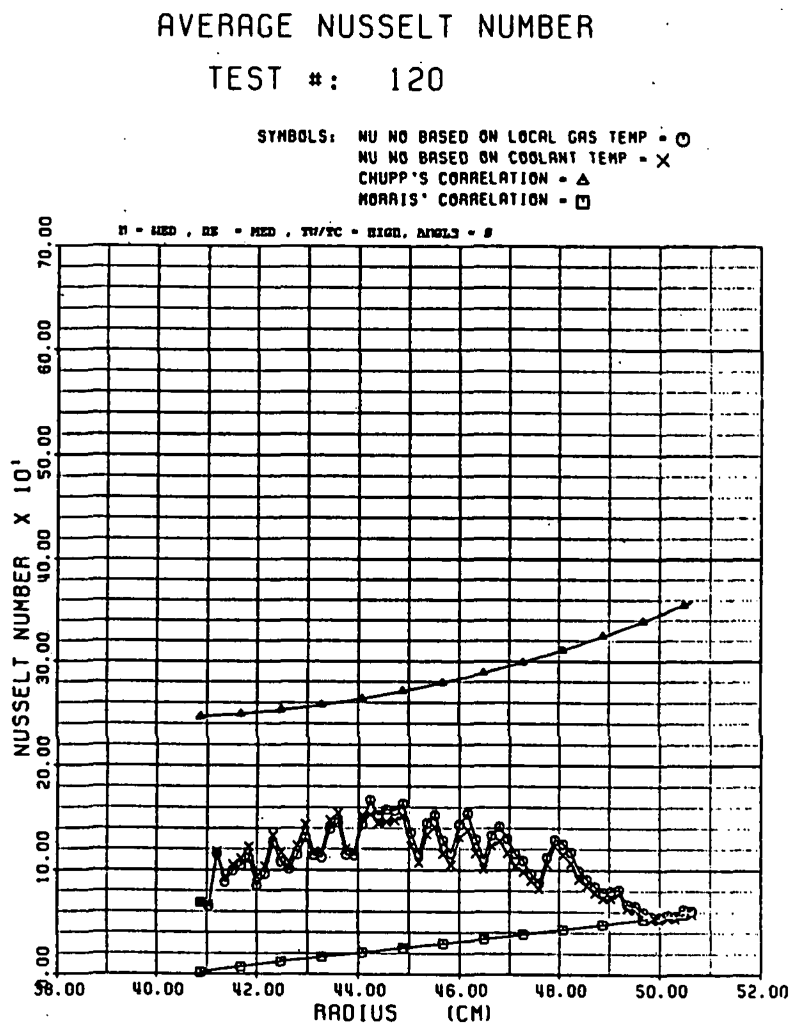

Figure 30D

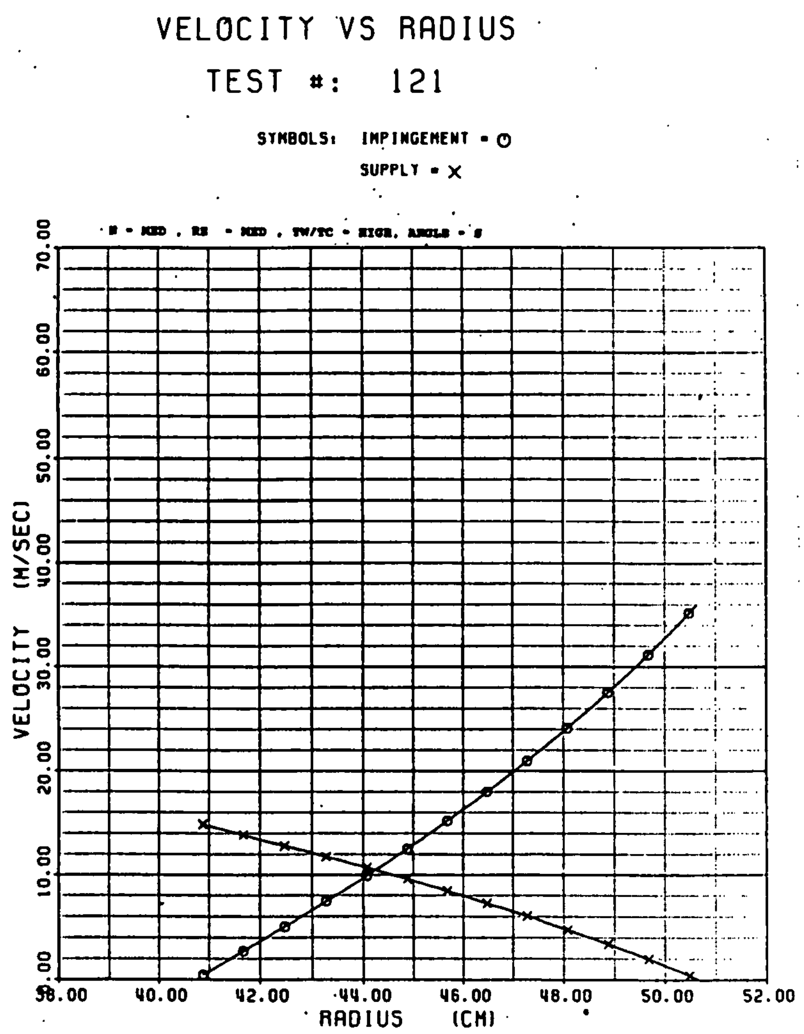

Figure 31A

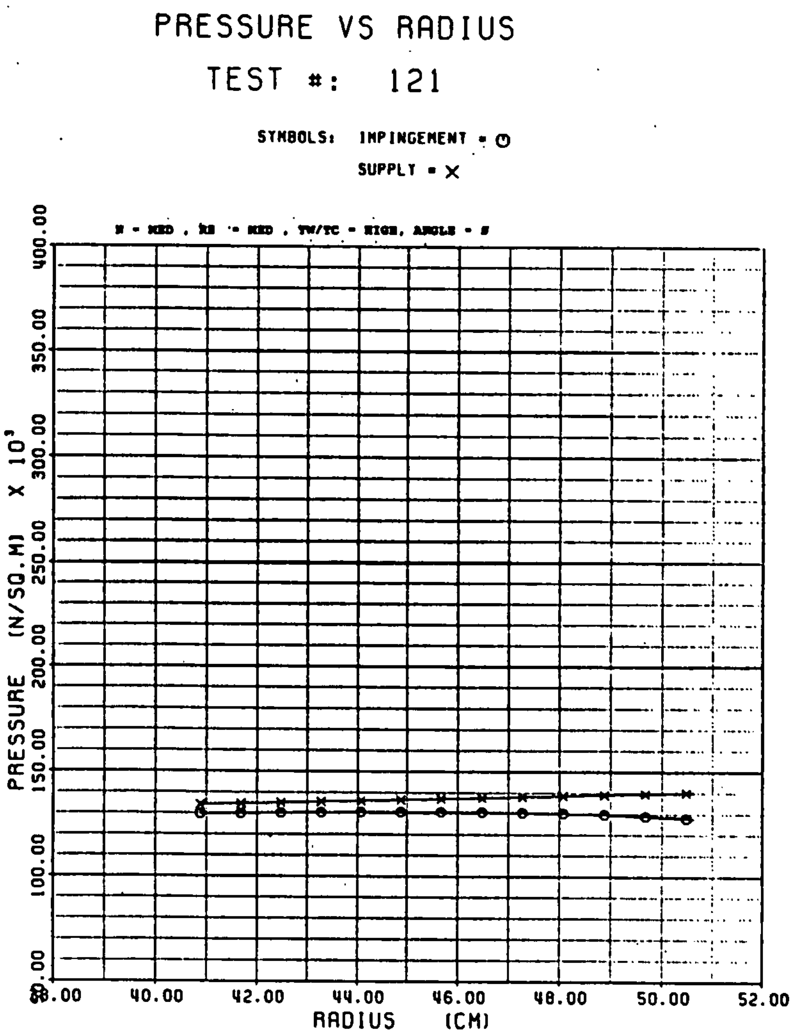

Figure 31B

ORIGINAL PAGE IS OF POOR QUALITY

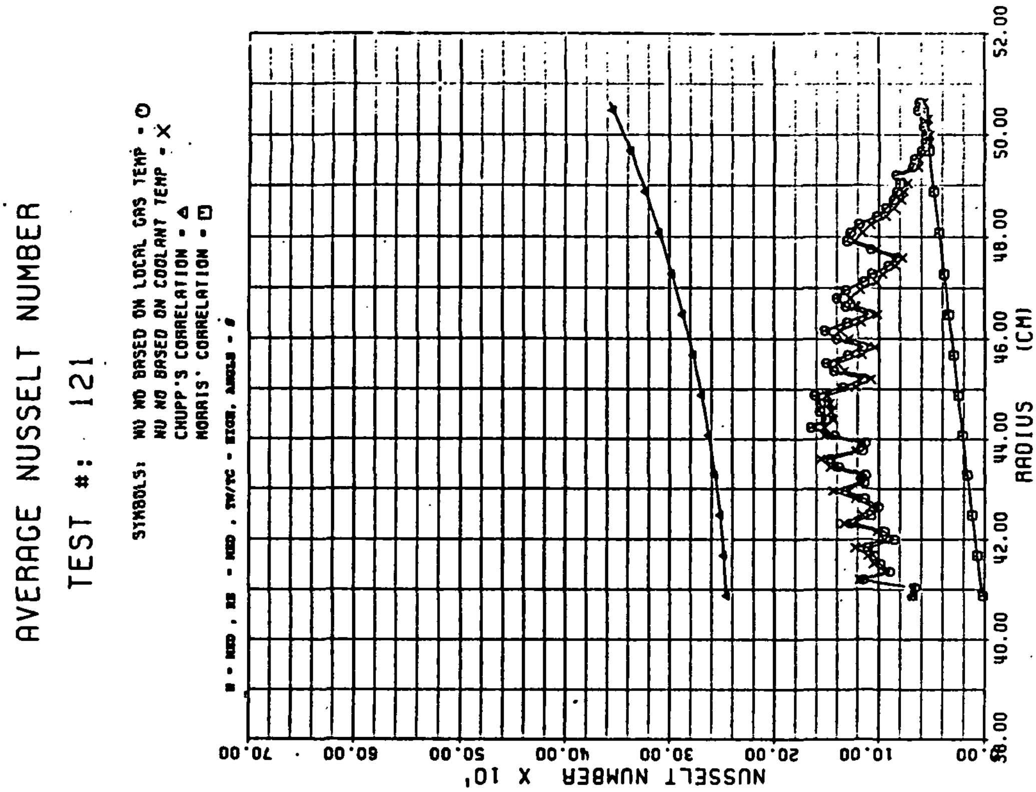

Figure 31D

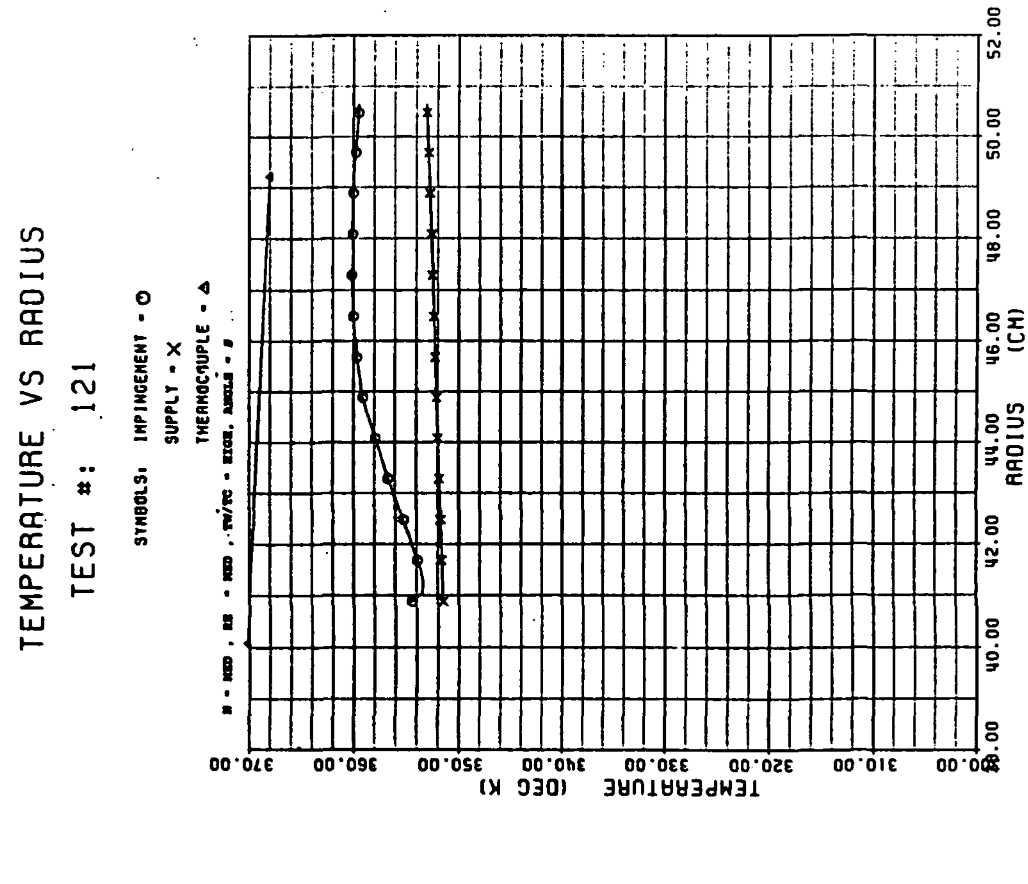

Figure 31C

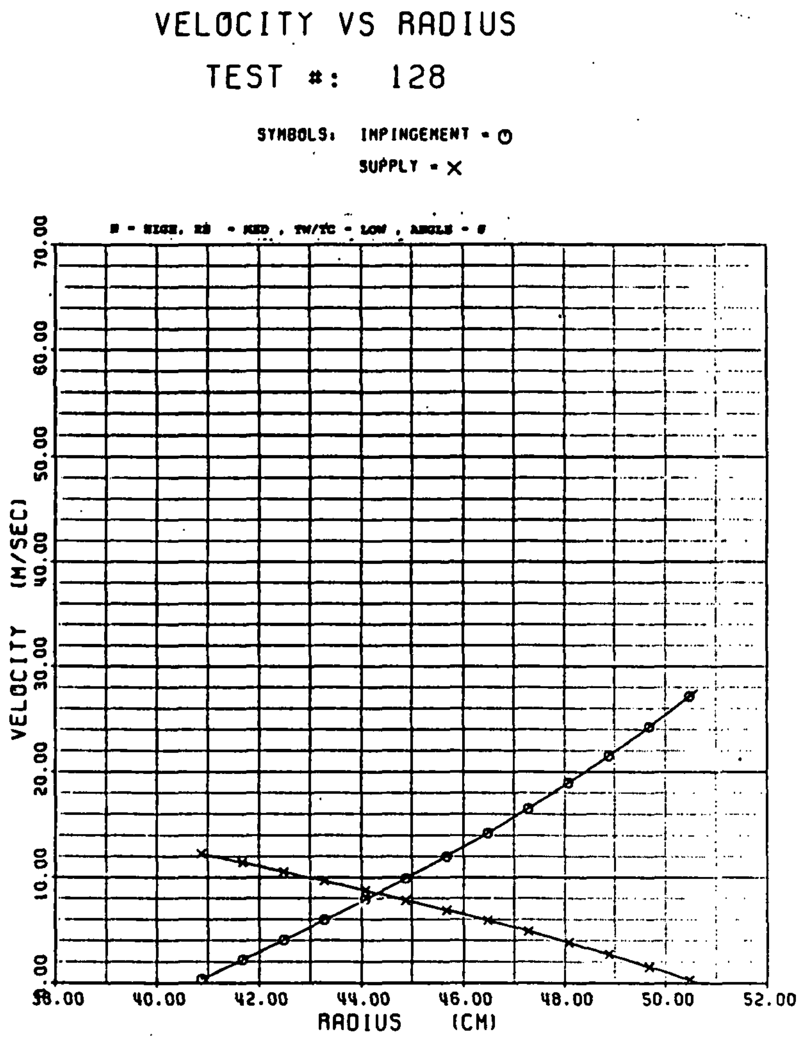

Figure 32A

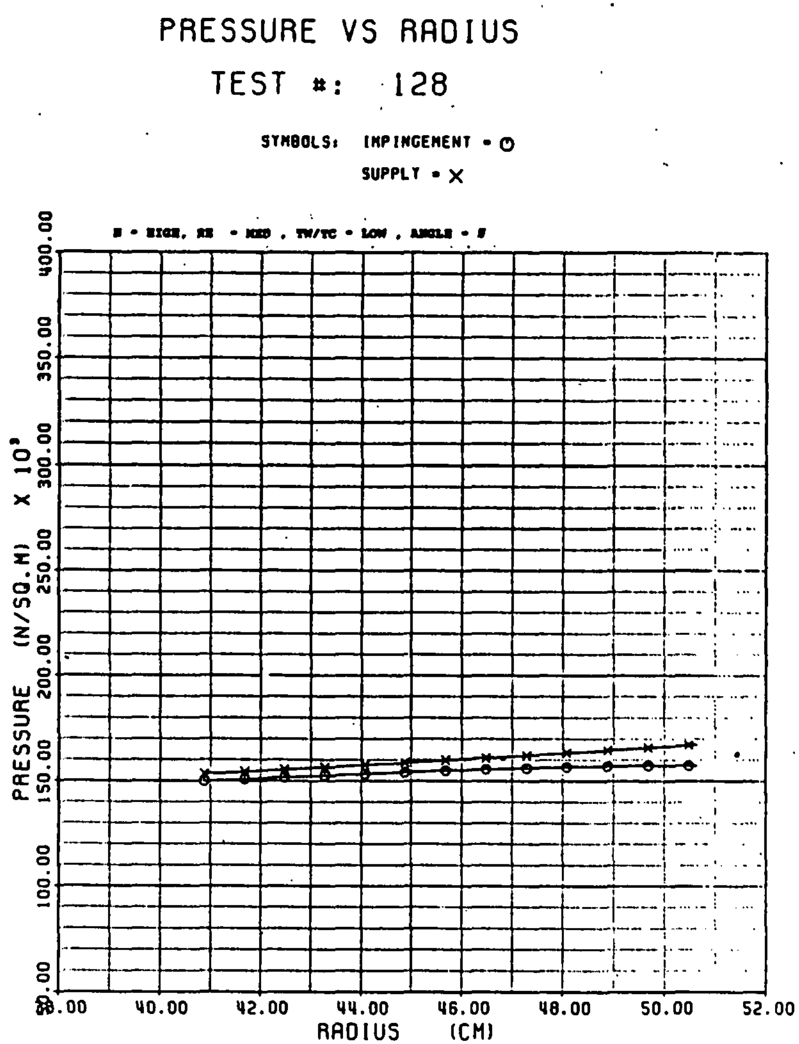

Figure 32B

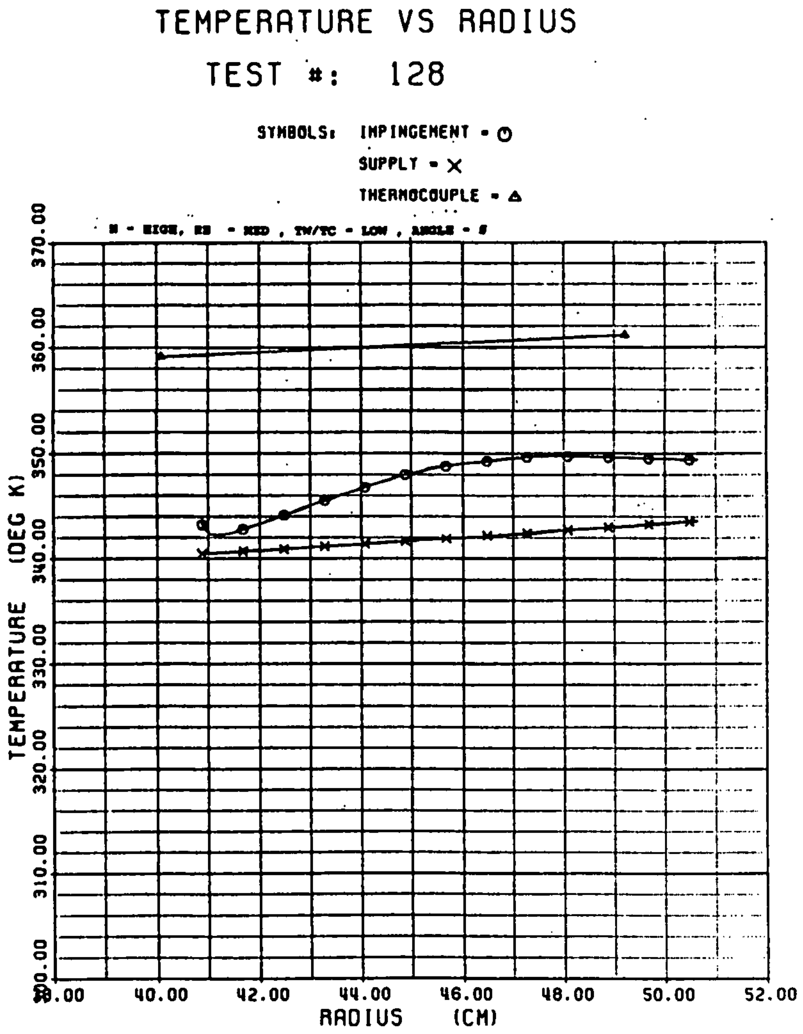

Figure 32C

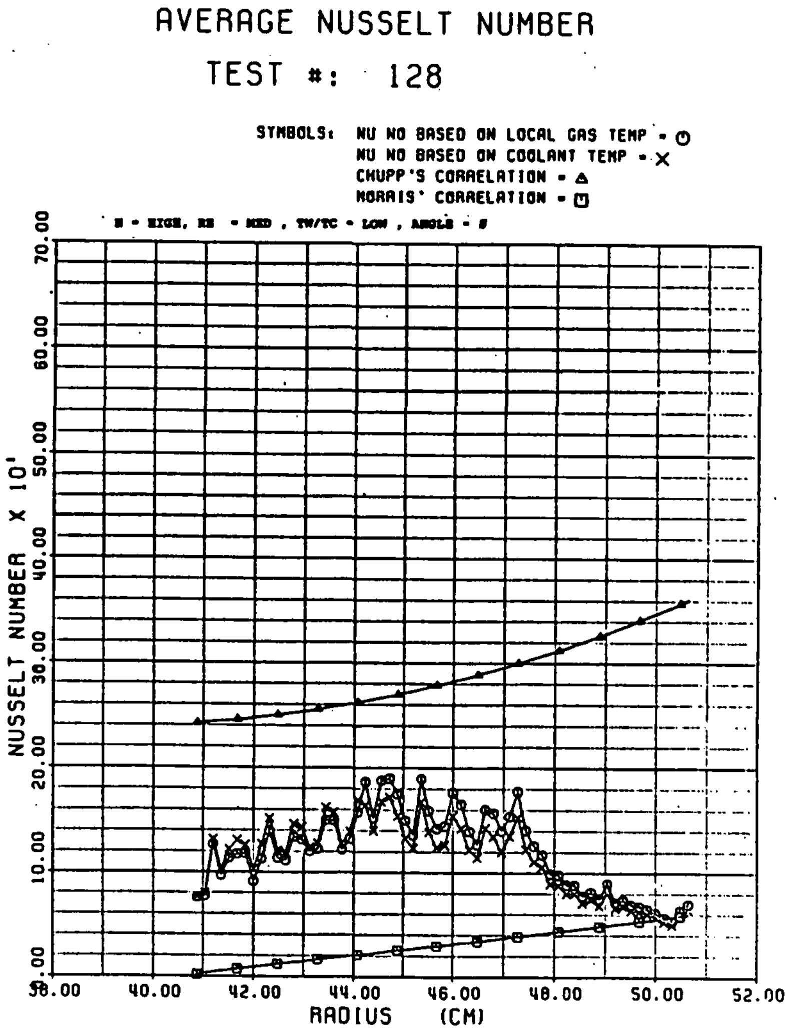

Figure 32D

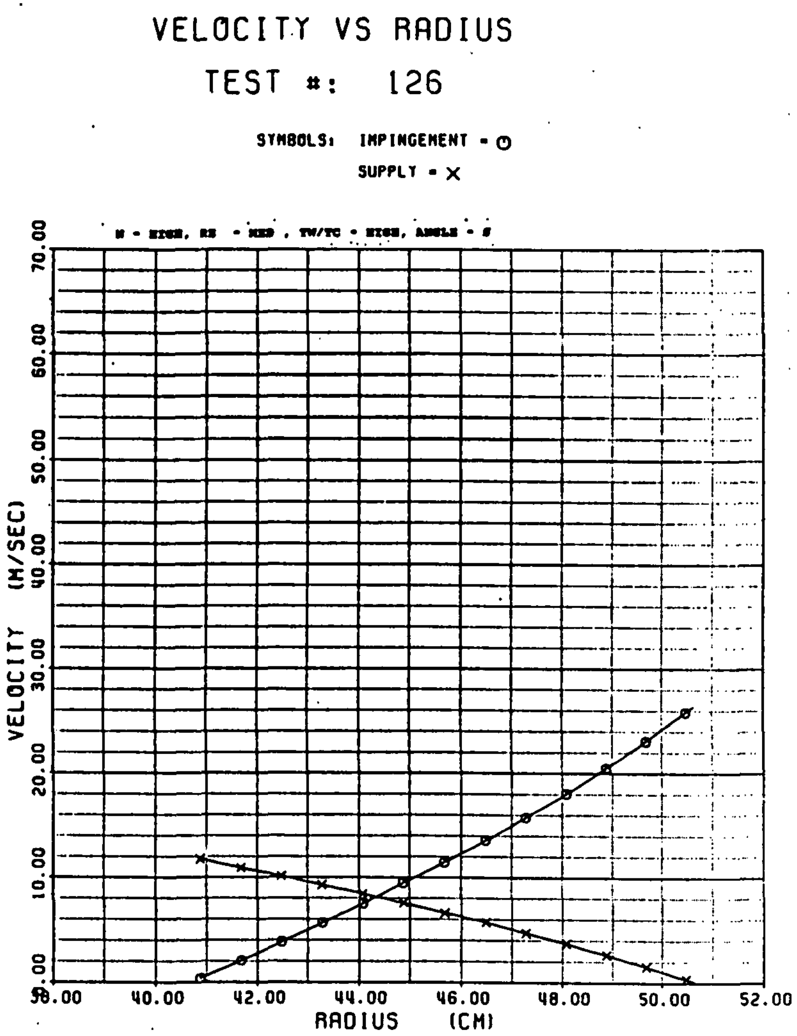

Figure 33A

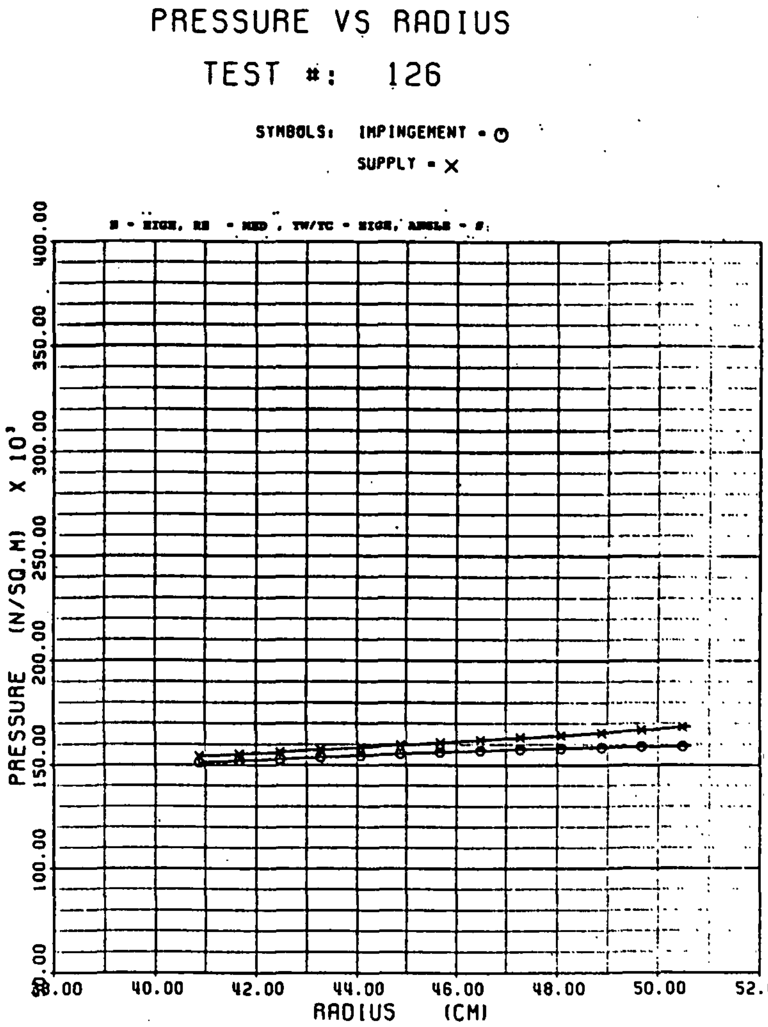

Figure 33B

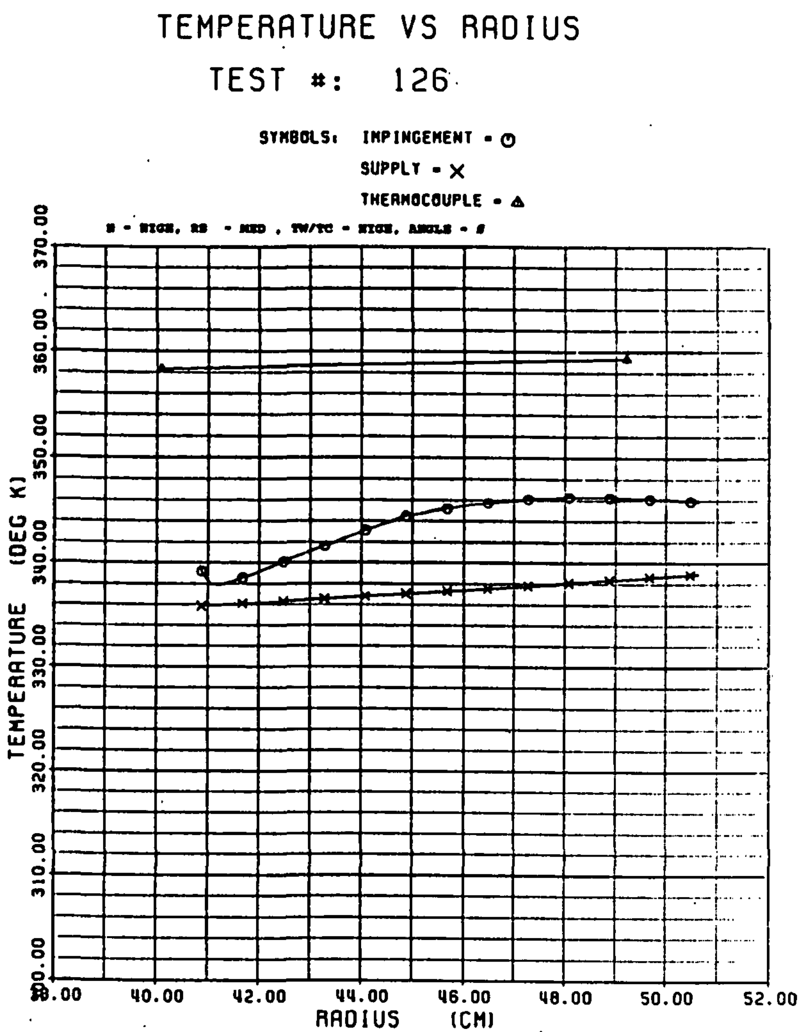

Figure 33C

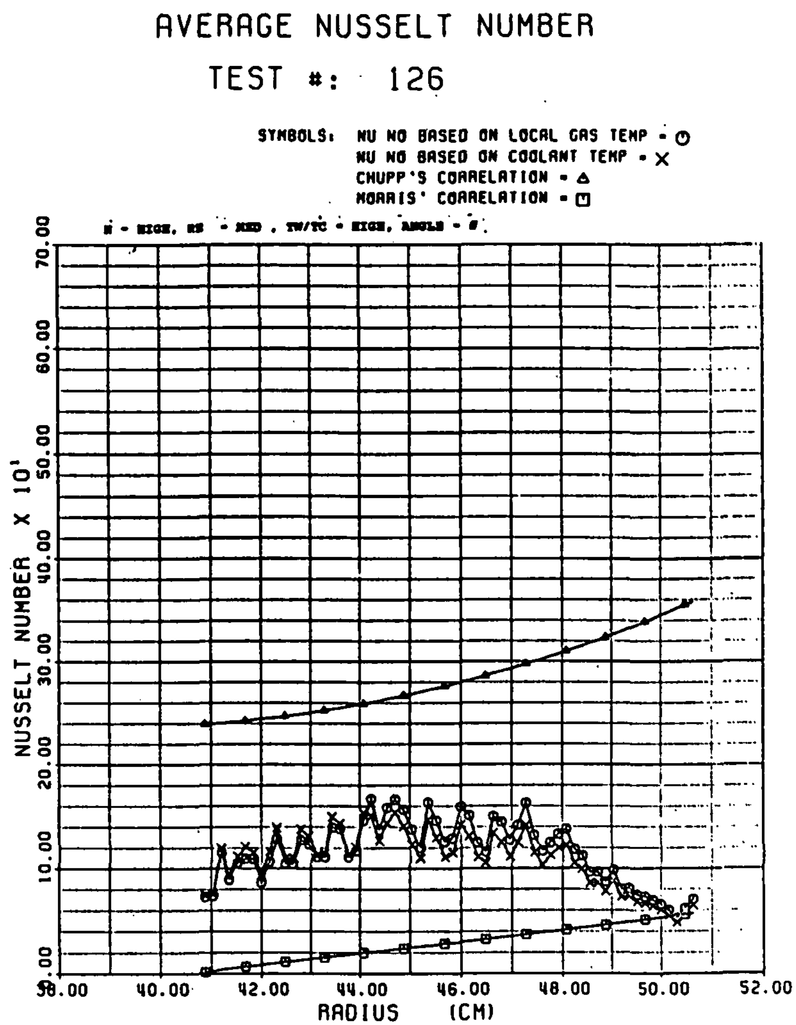

Figure 33D

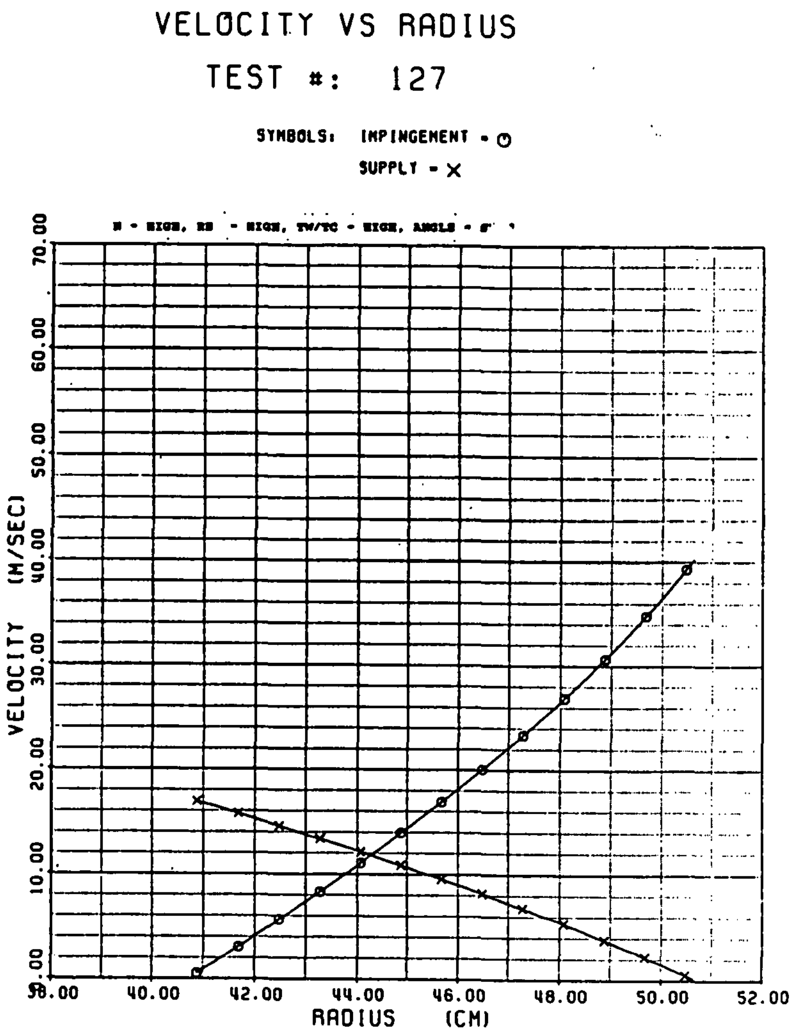

Figure 34A

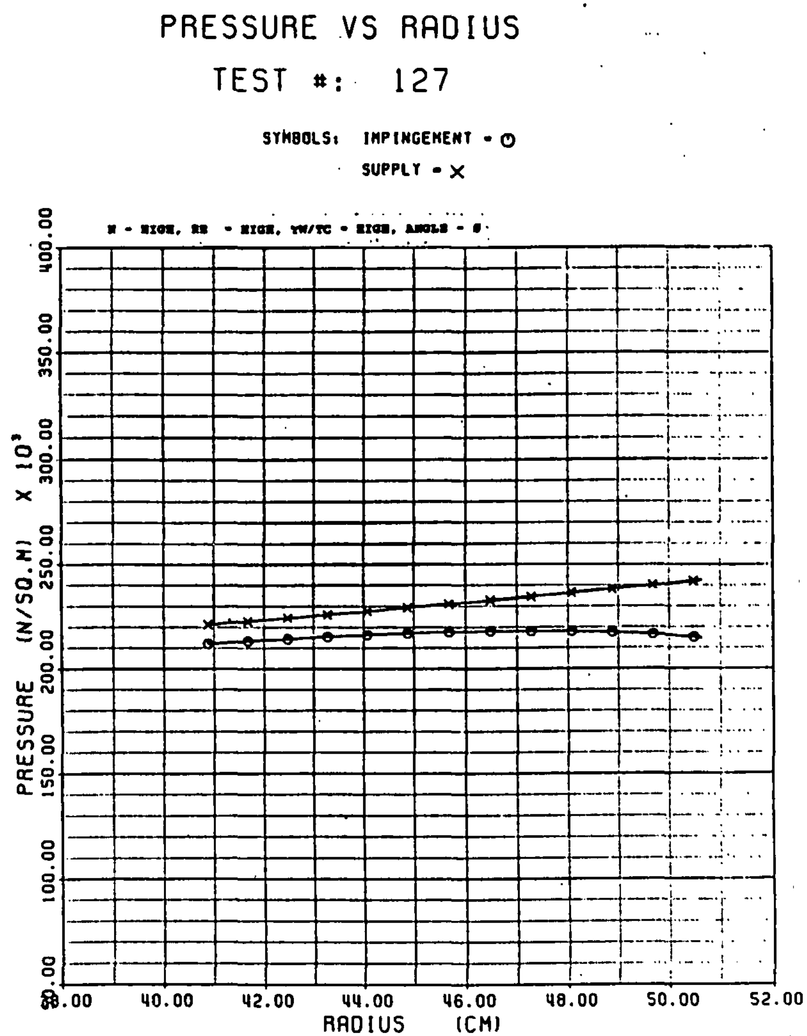

Figure 34B

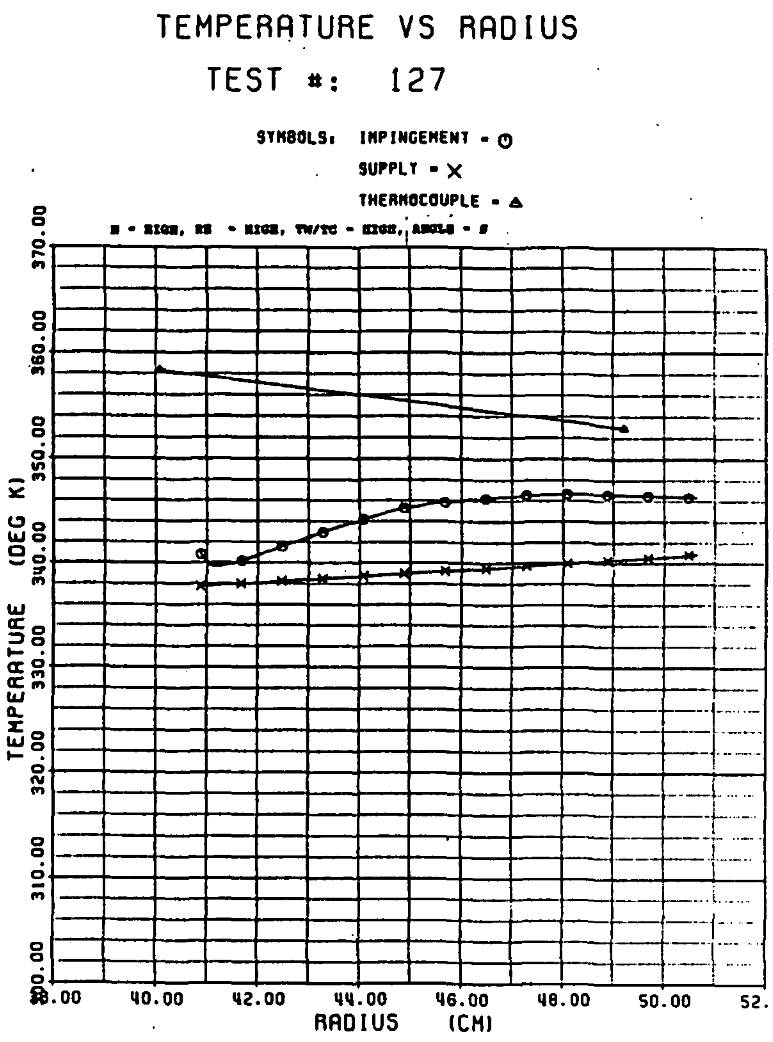

Figure 34C

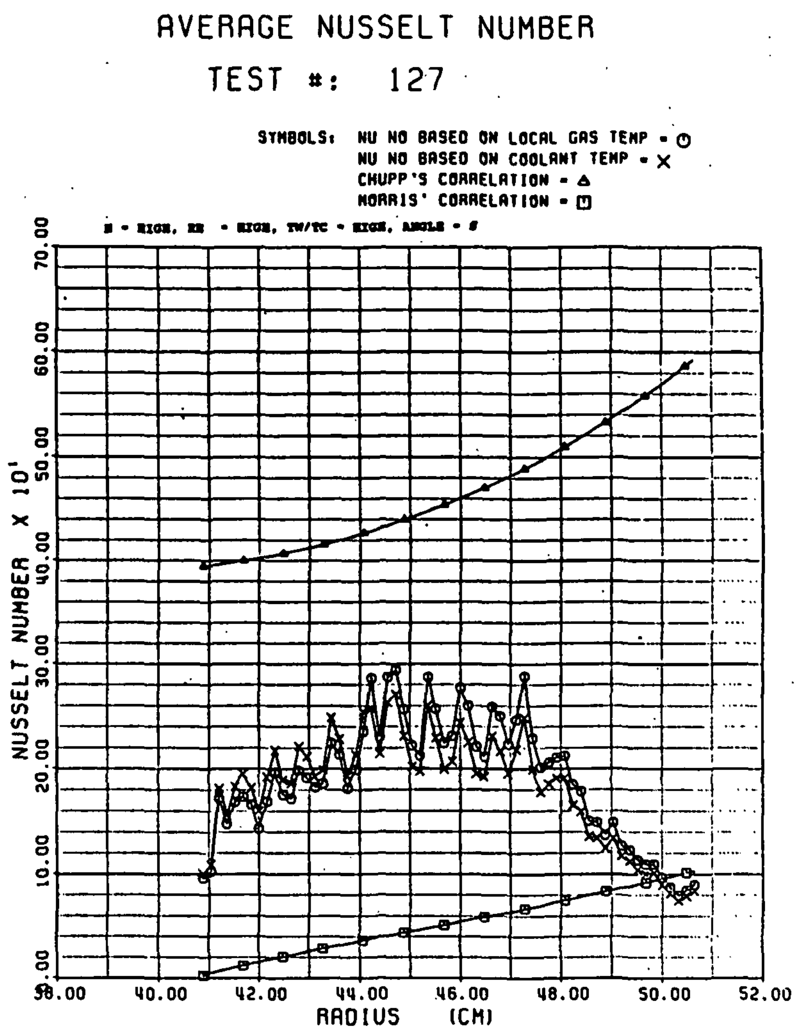

Figure 34D